Low temperature London penetration depth and superfluid density in Fe-based superconductors

by

Hyunsoo Kim

A dissertation submitted to the graduate faculty in partial fulfillment of the requirements for the degree of ${\tt DOCTOR\ OF\ PHILOSOPHY}$

Major: Condensed matter physics

Program of Study Committee:
Ruslan Prozorov, Major Professor
Makariy A. Tanatar
Paul C. Canfield
R. William McCallum
Charles R. Kerton

Iowa State University
Ames, Iowa
2013

Copyright © Hyunsoo Kim, 2013. All rights reserved.

UMI Number: 3597336

All rights reserved

INFORMATION TO ALL USERS

The quality of this reproduction is dependent upon the quality of the copy submitted.

In the unlikely event that the author did not send a complete manuscript and there are missing pages, these will be noted. Also, if material had to be removed, a note will indicate the deletion.



UMI 3597336

Published by ProQuest LLC (2013). Copyright in the Dissertation held by the Author.

Microform Edition © ProQuest LLC.
All rights reserved. This work is protected against unauthorized copying under Title 17, United States Code



ProQuest LLC. 789 East Eisenhower Parkway P.O. Box 1346 Ann Arbor, MI 48106 - 1346

TABLE OF CONTENTS

LIST (OF TA	BLES	V
LIST (OF FIG	GURES	vi
ACKN	OWLE	EDGEMENTS	ix
ABST	RACT		xi
СНАР	TER 1	I. INTRODUCTION	1
1.1	Prefac	e	1
1.2	Proper	rties of Fe-based superconductors	7
	1.2.1	Crystal structures	7
	1.2.2	Generic doping phase diagram: comparison to cuprates	8
	1.2.3	Magnetic structures	9
	1.2.4	Fermi surfaces	11
	1.2.5	Temperature-concentration Phase diagrams	12
	1.2.6	Superconducting mechanism and order parameter	16
1.3	Londo	n penetration depth	20
	1.3.1	Theory of the London penetration depth	20
	1.3.2	London penetration depth in Fe-based superconductors	24
CHAP	TER 2	2. EXPERIMENTAL	26
2.1	Tunne	diode resonator technique for London penetration depth measure-	
	ments		26
	2.1.1	Principles of tunnel diode resonator	26

	2.1.2 Calibration: conversion of measured Δf to $\Delta \lambda$	31
CHAP	TER 3. USE OF RUTGERS RELATION FOR THE ANALY-	
SIS	S OF THE SUPERFLUID DENSITY	36
3.1	Thermodynamic Rutgers relation	37
3.2	Theoretical results relevant for the analysis of the superfluid density	39
	3.2.1 Penetration depth in anisotropic materials	39
	$3.2.2 MgB_2 \dots $	40
	3.2.3 d-wave	41
	3.2.4 Scattering	41
3.3	Determination of $\lambda(0)$	42
3.4	Application of Rutgers formula to unconventional superconductors	46
CHAP	TER 4. DOPING DEPENDENCE OF LONDON PENETRA-	
TI	ON DEPTH AND SUPERFLUID DENSITY IN IRON-BASED	
\mathbf{SU}	PERCONDUCTORS	49
4.1	$\operatorname{Fe}_{1+y}\operatorname{Te}_{1-x}\operatorname{Se}_x$	50
	4.1.1 $Fe_{1.03}(Te_{0.63}Se_{0.37})$	52
	4.1.2 Fe(Te _{0.58} Se _{0.42})	57
4.2	$Ca_{10}(Pt_3As_8)((Fe_{1-x}Pt_x)_2As_2)_5 (0.028 \le x \le 0.097) \dots \dots \dots$	61
4.3	$Ba_{1-x}K_xFe_2As_2 \ (0.13 \le x \le 0.4) \dots$	66
4.4	Full substitution of Fe with Pd: $APd_2As_2\ (A=Ca,Sr)$ and $SrPd_2Ge_2$	7 3
	4.4.1 APd ₂ As ₂ (A = Ca, Sr)	74
	$4.4.2 \operatorname{SrPd_2Ge_2} \dots \dots$	7 6
4.5	Summary	81
CHAP	TER 5. EFFECT OF DISORDER ON LONDON PENETRA-	
TI	ON DEPTH IN IRON-BASED SUPERCONDUCTORS	83
5.1	Superconducting gap structure in stoichiometric LiFeAs and KFe $_2$ As $_2$	83

	5.1.1	Nodeless multi-gap superconductivity in LiFeAs	84
	5.1.2	Nodal superconducting gap in KFe_2As_2	91
5.2	Irradia	ation effect on London penetration depth in $Ba(Fe_{1-x}T_x)_2As_2$ ($T=Co$,	
	Ni) an	ad $Ba_{1-x}K_xFe_2As_2$ superconductors	102
	5.2.1	London penetration depth in Ba(Fe _{1-x} T _x) ₂ As ₂ (T=Co, Ni) super-	
		conductors irradiated with heavy ions	103
	5.2.2	London penetration depth in $\mathrm{Ba}_{1-x}\mathrm{K}_x\mathrm{Fe}_2\mathrm{As}_2$ irradiated with heavy	
		ion	110
5.3	Summ	ary	115
СНАР	TER 6	6. CONCLUSIONS	117
BIBLIOGRAPHY			120

LIST OF TABLES

Table 2.1	TDR circuit components for setup in a dilution refrigerator	31
Table 3.1	Physical parameters used for analysis of superfluid density with	
	Rutgers realtion	47
Table 5.1	Sample properties and parameters of exponential and power-law	
	fits for LiFeAs	85

LIST OF FIGURES

Figure 1.1	Crystal structures of Fe-based superconductors	8
Figure 1.2	Schematic phase diagram of copper-oxide-based and the 122 fam-	
	ily of iron-based superconductors	9
Figure 1.3	Magnetic structure of Fe-based superconductors	10
Figure 1.4	Fermi surfaces of $\rm Tl_2Ba_2CuO_{6+\delta}$ and $\rm Ba(Fe_{0.9}Co_{0.1})_2As_2$	11
Figure 1.5	Temperature-concentration phase diagrams of 122 compounds	12
Figure 1.6	Temperature-concentration phase diagrams of 1111, 11, and 10-3-8	
	compounds	15
Figure 1.7	A schematic representation of various superconducting order pa-	
	rameters: s-wave, d-wave, s_{++}-wave, and s_{\pm}-wave	16
Figure 1.8	Temperature dependent London penetration depth in Nb, MgB ₂ ,	
	and BSCCO	23
Figure 1.9	Theoretical superfluid density of s-wave and d-wave	24
Figure 2.1	IV characteristic curve of a tunnel diode	26
Figure 2.2	Circuit diagram for a prototypical TDR circuit	28
Figure 2.3	Schematic of TDR measurements	29
Figure 2.4	TDR setup on a dilution refrigerator	30
Figure 2.5	$\Delta f(T)$ vs. T/T_c in Cd and KFe ₂ As ₂	31
Figure 2.6	Contour lines of the vector potential in a semi-infinite supercon-	
	ducting slab	32

Figure 3.1	London penetration depth and superfluid density of Nb calculated	
	with various choices of $\lambda(0)$	43
Figure 3.2	Application of Rutgers formula to Nb and MgB_2	45
Figure 3.3	Superfluid density in LiFeAs, FeTe $_{0.58}$ Se $_{0.42}$, YBa $_2$ Cu $_3$ O $_{1-\delta}$, and	
	$MgCNi_3$	48
Figure 4.1	London penetration depth in $Fe_{1.03}(Te_{0.63}Se_{0.37})$	52
Figure 4.2	London penetration depth plotted vs. $(T/T_c)^2$ in Fe _{1.03} (Te _{0.63} Se _{0.37}).	53
Figure 4.3	Power-law behavior of $\Delta\lambda(T)$ in Fe _{1.03} (Te _{0.63} Se _{0.37})	54
Figure 4.4	Determination of $\lambda(0)$ in $\mathrm{Fe}_{1.03}(\mathrm{Te}_{0.63}\mathrm{Se}_{0.37})$	55
Figure 4.5	Superfluid density in $Fe_{1.03}(Te_{0.63}Se_{0.37})$	57
Figure 4.6	χ_{ac} and $\Delta\lambda$ in Fe(Te _{0.58} Se _{0.42}) and Fe _{1.03} (Te _{0.63} Se _{0.37})	58
Figure 4.7	Power-law behavior of $\Delta \lambda$ in $\text{Fe}_{1+y}\text{Te}_{1-x}\text{Se}_x$	59
Figure 4.8	Superfluid density in $Fe(Te_{0.58}Se_{0.42})$	60
Figure 4.9	Variation of London penetration depth in 10-3-8 system	62
Figure 4.10	$\Delta\lambda(T)$ in under doped 10-3-8 compounds	63
Figure 4.11	Power-law behavior of $\Delta\lambda$ and T - x phase diagram in 10-3-8 system.	64
Figure 4.12	Superfluid density of the optimally doped 10-3-8 sample	65
Figure 4.13	Temperature variation of London penetration depth in under doped	
	$Ba_{1-x}K_xFe_2As_2$	68
Figure 4.14	Power-law behavior of $\Delta \lambda$ in under doped $\mathrm{Ba}_{1-x}\mathrm{K}_x\mathrm{Fe}_2\mathrm{As}_2$	70
Figure 4.15	Superfluid density in optimally doped $Ba_{1-x}K_xFe_2As_2$	71
Figure 4.16	Exponent-concentration phase diagram in $Ba_{1-x}K_xFe_2As_2$	73
Figure 4.17	London penetration depth in APd_2As_2 (A = Ca, Sr)	75
Figure 4.18	London penetration depth in $SrPd_2Ge_2$	77
Figure 4.19	Application of Rutgers formula to SrPd ₂ Ge ₂	79
Figure 4.20	Superfluid density in SrPd ₂ Ge ₂	80

Figure 5.1	Resistivity, skindepth, and London penetration depth in LiFeAs.	86
Figure 5.2	London penetration depth and power-law fitting in LiFeAs	87
Figure 5.3	Power-law behavior of $\Delta \lambda$ in LiFeAs	88
Figure 5.4	Superfluid density in LiFeAs	89
Figure 5.5	Electrical resistivity, T_c vs residual electrical resistivity, and $\Delta\lambda(T)$	
	in $K_{1-x}Na_xFe_2As_2$ (x=0, 0.07)	94
Figure 5.6	Power-law behavior of $\Delta\lambda(T)$ in $K_{1-x}Na_xFe_2As_2$ (x=0, 0.07)	96
Figure 5.7	Temperature variation of Δf for configurations with H_{ac} parallel	
	and perpendicular to tetragonal c-axis in KFe_2As_2	98
Figure 5.8	Superfluid density in $K_{1-x}Na_xFe_2As_2$ (x=0, 0.07)	100
Figure 5.9	Variation of $\Delta\lambda$ in heavy ion irradiated Ba(Fe _{1-x} T _x) ₂ As ₂ (T =	
	Co, Ni)	105
Figure 5.10	Detailed comparison of the functional form of $\Delta\lambda(T)$ for heavy	
	ion irradiated Ba(Fe _{1-x} T _x) ₂ As ₂ (T = Co, Ni)	106
Figure 5.11	Variation of T_c and power-law of $\Delta\lambda(T)$ in Ba(Fe _{1-x} T _x) ₂ As ₂ (T	
	= Co, Ni) upon heavy ion irradiation	107
Figure 5.12	Theoretical superfluid density and evolution of T_c upon heavy ion	
	irradiation in Ba(Fe _{1-x} T _x) ₂ As ₂ (T = Co, Ni)	108
Figure 5.13	Change in $\Delta \lambda$ in Ba _{0.6} K _{0.4} Fe ₂ As ₂ with $T_c = 38$ K for $B_{\phi} = 0, 2$,	
	4 T	111
Figure 5.14	Change in $\Delta\lambda$ in Ba _{0.6} K _{0.4} Fe ₂ As ₂ with $T_c=36.8$ K for $B_\phi=21$ T.	113
Figure 5.15	Change in London penetration depth near T_c for $\mathrm{Ba}_{0.6}\mathrm{K}_{0.4}\mathrm{Fe}_2\mathrm{As}_2$	
	with $T_c = 36.8$ K and 38 K, for different irradiation levels	114

ACKNOWLEDGEMENTS

I would like to take this opportunity to express my sincere gratitude to those who have helped me in completing my Ph.D., and in writing my thesis. First and foremost, I thank Dr. Ruslan Prozorov and Dr. Makariy Tanatar for guidance, constant encouragement and support throughout my Ph.D. I will never forget the philosophy of Gena-na in writing concise research articles. I would also like to thank my committee members for their contributions to this work: Dr. Paul Canfield, Dr. R. William McCallum, and Dr. Charles Kerton. I would like to thank Joerg Schmalian and Adam Kaminski for serving as a committee member for some period of time, and I regret that I had to replace them due to unavoidable reasons.

I would like to thank Dr. Paul Canfield for helping me to improve my thesis with fruitful discussion and critical reading. I would like to thank Dr. Vladimir Kogan for helping understanding problems in theoretical aspects and for valuable advices. I will keep in mind that always try to contribute to the society. I would like to thank Dr. Sergey Budko for providing not only discussion about physics but also unlimited amount of caffeine. I would like to thank Dr. Tanya Prozorov for using personal time to help out SML-group business.

I would like to thank former and current SML-group members for help: Dr. Catalin Martin, Dr. Matt Vannette, Brett McCarty, Dr. Ryan Gordon, Jacob Hoberg, Plengchart Prommapan, Nick Spyrison, Dr. Kyuil Cho, Dr. Vikash Malik, Erick Blomberg, Steve Yeninas, Jason Murphy, Charles Strehlow, Serafim Teknowijoyo.

To my parents, I would like to express my thanks for all of their encouragement. Especially, I would like thank my mom for coming over here all the way from Busan to take care of Richard while I was preparing this thesis.

Lastly, I would like to sincerely thank my wife Halyna for all the support, understanding, and taking best care of Richard.

This work was performed at the Ames Laboratory under contract number DE-AC02-07CH11358 with the U.S. Department of Energy. The document number assigned to this thesis/dissertation is IS-T 3099.

ABSTRACT

The superconducting gap symmetry of the Fe-based superconductors was studied by measurements and analysis of London penetration depth and superfluid density. Tunnel diode resonator technique for these measurements was implemented in a dilution refrigerator allowing for the temperatures down to 50 mK. For the analysis of the superfluid density, we used both experimental studies of Al-coated samples and original thermodynamic approach based on Rutgers relation. In three systems studied, we found that the superconducting gap at the optimal doping is best described in multi-gap full gap scenario. By performing experiments on samples with artificially introduced disorder with heavy ion irradiation, we show that evolution of the superconducting transition temperature and of the superfluid density are consistent with full-gap sign changing s₊ superconducting state. The superconducting gap develops strong modulation both in the under-doped and the over-doped regimes. In the terminal hole-doped KFe₂As₂, both temperature dependence of the superfluid density and its evolution with increase of the scattering rate are consistent with symmetry imposed vertical line nodes in the superconducting gap. By comparative studies of hole-doped (Ba,K)Fe₂As₂ and electron-doped Ca10-3-8, we show that the superconducting gap modulation in the under-doped regime is intrinsic and is not induced by the coexisting static magnetic order.

CHAPTER 1. INTRODUCTION

1.1 Preface

Superconductivity is one of rare macroscopic quantum phenomena [1]. The phenomenon refers to abrupt disappearance of electrical resistivity and complete expulsion of magnetic field from the bulk of the sample, so-called Meissner effect. Attempts to understand this mysterious phenomenon led to the developments of both experimental methods and theoretical understandings which currently serve as main tools in condensed matter physics.

For a quarter-century after the discovery in 1911, the origin of superconductivity was not understood. Discovery of the Meissner effect stimulated London brothers to develop a theory of magnetic field penetration into a superconductor [2]. The brothers developed the concept of London penetration depth, a characteristic length scale of superconductors. Thermodynamics of superconductors was first successfully described by Ginzburg-Landau theory of late 1940s [3]. But microscopic understanding of the phenomenon was lacking until key experiments found isotope substitution effect on superconducting phase transition temperature T_c [4] and evidence for a superconducting energy gap [5]. These two experimental findings and a theoretical idea about pairing of electrons by even a weak attraction [6] led to the first successful microscopic theory for superconductivity suggested by J. Bardeen, L. N. Cooper, and J. R. Schrieffer (BCS) in 1957 [7]. The BCS theory considers the Bose-Einstein condensation of pairs formed by conduction electrons, so-called Cooper pairs. The electrons in the pair have opposite

spins and momenta. The pairing is caused by electron-phonon interactions, the strength of which determines T_c . Pairing is isotropic and leads to a superconducting gap which is constant over the Fermi surface, so-called s-wave pairing. In the BCS scenario, T_c would be dependent on the strength of electron-phonon coupling and on the detailed electronic structure of materials [8, 9]. This isotropic interaction is robust against scattering by non-magnetic impurities [10], but magnetic scattering is strongly antagonistic to the spin-singlet pairing weakening superconductivity [11].

Studying superconductivity is important not only for scientific research but also for applications. Practical implementation of superconductors requires materials with high operational parameters such as superconducting critical temperature (T_c) , upper critical magnetic field (H_{c2}) , and critical current density (j_c) , the highest values of temperature, magnetic field and critical current density that superconductor can withstand. This permanent desire for improving these parameters led to search and discovery of numerous superconducting materials.

Elemental metals were the first superconductors, and their T_c at ambient pressure is limited by ~ 10 K. In 1930s, higher T_c values were observed in some intermetallic alloys. This new direction eventually led to the discovery of Nb₃Sn and Nb₃Ge with $T_c = 18$ K and 23 K, respectively, in early 1970s. In materials with presumably phonon-mediated superconductivity, this T_c remained the highest until discovery of superconductivity with $T_c \approx 23$ K in various compositions of Y-Pd-B-C [12, 13], and eventually the record value for this class of materials was set at $T_c = 40$ K in MgB₂ [14, 15]. The superconductivity in MgB₂ is fully understood within the phonon-mediated mechanism as suggested by the magnitude of the isotope effect [16]. Superconductivity in MgB₂ also has pronounced multigap character with magnitude of the gap differing two times on different Fermi surface sheets [17, 18].

In the mid 1980s, surprisingly, materials with T_c well above 100 K were discovered among charge-doped copper oxides. This unexpected observation ignited a new hope for

discovery of materials which could be superconducting at ambient temperatures, but the highest T_c from this class of materials remains 155 K at 30 GPa to date.

It is interesting that the undoped parent compounds of the high T_c superconductors, so-called cuprates, revealed antiferromagnetism in the insulating state with enormously high Néel temperatures T_N . Superconductivity in cuprates is different from conventional s-wave in that superconducting gap has zeros, and phase sensitive experiments unambiguously showed that the symmetry of the order parameter is d-wave [19]. This proximity of superconductivity to magnetism and highly anisotropic order parameter are antagonistic with BCS theory. According to Abrikosov-Gor'kov theory [11], electron scattering on magnetic moments tends to break Cooper pairs, thus weakening superconductivity and suppressing T_c . Observation of high T_N led to the suggestion that magnetism rather than phonons may be responsible for such high T_c of cuprates. Cuprates are not the only class of materials in which superconductivity seems to like magnetism. Before their discovery, superconductivity was found in $CeCu_2Si_2$ with $T_c = 0.5$ K which attracted a good deal of attention [20]. The superconductivity in CeCu₂Si₂ required almost 100% of Ce-magnetic moments, a few atomic percent of nonmagnetic substitution was sufficient to kill superconductivity completely, and superconductivity was not observed in the electronically equivalent LaCu₂Si₂ [21]. This discovery shone new light on interplay between superconductivity and magnetism, which is now believed to be crucial for understanding the unconventional superconductors.

In 1998, superconductivity was discovered in another heavy fermion material, CeIn₃, under pressure [22]. This discovery brought an interesting insight into magnetic mechanism of superconductivity. CeIn₃ is an antiferromagnetic metal at ambient pressure with $T_N \sim 10$ K. With application of pressure T_N is driven to zero, and superconductivity appears at the edge of magnetic dome. The superconductivity was linked to magnetic quantum critical point (QCP) where the material undergoes a zero temperature non-thermal phase transition. Magnetic fluctuations near this transition are quantum in

nature. They affect normal state properties in a rather broad temperature domain and lead to their significant deviations from standard theory of metals, Fermi liquid theory of Landau. These magnetic fluctuations were suggested to mediate superconducting pairing and bring exotic superconducting order parameter different from s-wave of BCS theory. It was predicted that superconducting T_c in this family of materials can be notably increased in two dimensional materials [22], and indeed superconducting T_c jumped from 0.1 K to 2.3 K in layered CeCoIn₅ [23]. In addition, superconductivity with similar T_c was found in CeIrIn₅ and CeRhIn₅ under pressure. These three compounds are frequently referred to as "115" compounds. It was suggested that superconductivity in 115 compounds is d-wave, similar to the cuprates [24].

In 2008 the second class of high- T_c superconductors was discovered in a series of LaFeAsO_{1-x}F_x [25]. These Fe-based superconductors (FeSC) have attracted enormous attention with a hope for higher T_c than that of the copper-oxide superconductors and a hope to understand the pairing mechanism behind. The highest T_c observed in these materials up to date is 55 K [26]. Interestingly similar to cuprates and 115 compounds, highest T_c is found in the proximity of antiferromagnetic QCP [27]. However, initial studies of superconducting gap of FeSC found no zeros being inconsistent with d-wave [28, 29]. Is this compatible with magnetically mediated pairing? An exotic superconducting order parameter was suggested for FeSC in which superconducting gap changes sign on different Fermi surfaces, so-called s_{\pm} pairing. Verification of this suggestion in connection with different interactions between magnetism and superconductivity is main subject of this thesis.

Knowing the structure of the superconducting gap is the most crucial prerequisite for understanding the mechanism of superconductivity. The gap structure can be explored directly or indirectly by various experimental methods. Unlike copper oxide superconductors in which d-wave symmetry was found in all related compounds, a variety of experiments done in FeSC have revealed non-universal gap-symmetry. It is not clear

whether this non-universality is intrinsic or not. In order to elucidate this issue, measurements on samples of higher quality with controlled degree of disorder are needed.

The London penetration depth, λ , is among the most useful probes to study the superconducting gap structure. However, analysis of λ in FeSC is not trivial for many reasons. Fe-based superconductors have complicated band structures with up to five Fermi surface sheets. As a result, superconductivity has pronounced multiband character, which makes analysis of experimental λ difficult. In most of the Fe-based compounds superconductivity is induced by chemical substitution which adds significant disorder into the system. The effect of uncontrolled disorder masks intrinsic response of unconventional superconducting state. That is why it is important to study London penetration depth in materials with independent of doping control of disorder. In this thesis, we use heavy ion irradiation to probe superconducting pairing mechanism.

For understanding the relation between magnetism and superconductivity, it is important to study materials in which the two phases interact in a different way in the phase diagram. For example, in $BaFe_2As_2$ -based compounds with hole, electron, isoelectron doping superconductivity and magnetism coexist in the bulk [30, 31, 32]. The magnetic ground state of parent $BaFe_2As_2$ has stripe type antiferromagetic order. In the phase diagram of 1111 compounds, magnetism has similar stripe structure, but is separated from superconductivity in the doping phase diagram. In the phase diagram of $Ca_{10}(Pt_3As_8)((Fe_{1-x}Pt_x)_2As_2)_5$, magnetism and superconductivity are separated as well [33, 34]. In Fe(Se,Te) magnetic ground state has double stripe structure. How do these differences affect superconducting state? Do they affect the superconducting gap structure? These are questions addressed experimentally in this thesis.

Superconductivity in most of the FeSC is induced by chemical substitution which inevitably introduces disorder into the lattice. The degree of the disorder and its effect on superconducting gap structure in unconventional superconductors is very difficult to separate from the effect of doping. To get an insight into effect of disorder, we took two approaches. First, we studied stoichiometric compounds representative of optimal doping regime, LiFeAs, and heavily overdoped KFe₂As₂. Second, we used heavy ion radiation to have an independent of doping control of disorder.

In this thesis, I present a comprehensive study of the temperature variation of London penetration depth $\Delta\lambda(T)$ in various FeSC which are chemically tuned as well as disorder-controlled. This thesis begins with introduction to superconducting properties of the Fe-based superconductors. In the first half of this chapter, the structure of the superconducting order parameter in FeSC will be extensively discussed with some key experimental results. Most of the examples will be based on thermodynamic properties compared with the London penetration depth measurements, which will be presented in the second half of this chapter.

The experimental technique used to measure $\Delta\lambda(T)$ for this thesis is a tunnel diode resonator technique, and its principles associated with measurements of $\Delta\lambda(T)$ will be explained in-depth in the following chapter.

Temperature variation of the London penetration depth provides somewhat limited information about the gap-structure. The structure of the superconducting gap can be further investigated over full superconducting temperatures by studying superfluid density which can be calculated from known $\Delta\lambda(T)$ and $\lambda(0)$. However, measurement of $\lambda(0)$ remains most challenging to date. In chapter 3, I will introduce a new way of determining the absolute value of $\lambda(0)$ by using a modified Rutgers formula. The original form of the formula, which is purely thermodynamic, can be re-written so that superfluid density is related to directly measurable thermodynamic quantities.

Chapter 4 covers results on the London penetration depth measurements in several chemically tuned systems in which superconductivity and magnetism interplay in a different way. The first two sections deal with the simplest and almost isotropic binary phase of Fe(Te,Se) through one of the most complicated and highly two-dimensional phase $Ca_{10}(Pt_3As_8)((Fe_{1-x}Pt_x)_2As_2)_5$, the so-called 10-3-8 phase. Second half of the

chapter describes study of the materials in which superconductivity and magnetism coexist; under-doped (Ba,K)Fe₂As₂. These FeSC are contrasted with low T_c isostructural compounds, CaPd₂As₂, SrPd₂As₂, and SrPd₂Ge₂ as end members of the so-called 122 systems in which Fe is completely replaced by Pd for the first two materials and As is replaced by Ge in the last compound.

The experimental results on the London penetration depth measurements in two stoichiometric superconductors LiFeAs and KFe₂As₂ are discussed in chapter 5. The absence of substitutional disorder makes interpretation of experimental $\Delta\lambda(T)$ in these materials rather straightforward. Next, we use irradiation technique to deliberately introduce disorder into optimally electron-and hole-doped BaFe₂As₂ superconductors and study its effect on $\Delta\lambda(T)$.

In chapter 6, I will summarize and conclude this thesis.

Analysis of superfluid density with the Rutgers relation in chapter 3 has been published in Physical Review B 87, 214518 (2013). The experimental results of the chapter 4 were published in Physical Review B 81, 180503 (2010), Physical Review B 84, 174502 (2011), Physical Review B 85, 020504 (2012), Physical Review B 87, 224510 (2013) Physical Review B 87, 094515 (2013). The results of the chapter 5 were published in Physical Review B 83, 100502 (2011), Physical Review B 82, 060518 (2010), Physical Review B 87, 180502 (2013).

1.2 Properties of Fe-based superconductors

1.2.1 Crystal structures

Superconductivity was observed in several families of Fe-based materials with different crystal structures. Four families have been studied most widely; FeSe (11), AFeAs (111), AEFe₂As₂ (122), and RFeAsO (1111) where A is alkali metal, AE stands for alkali earth metals, and R represents rare earth elements. The crystal structures of these compounds

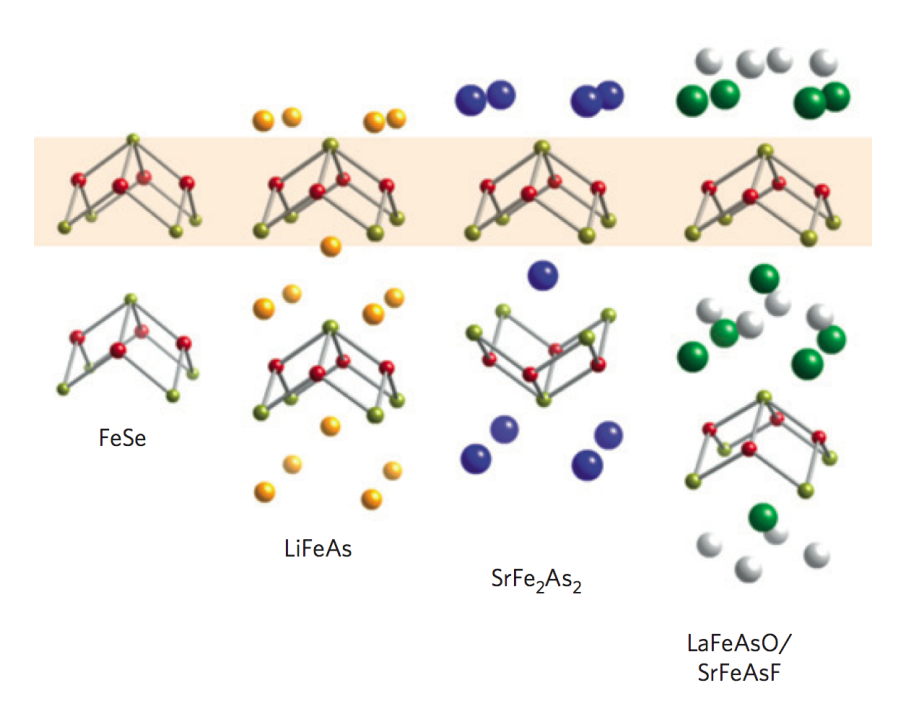


Figure 1.1 Crystal structure of the iron-based superconductors. The four tetragonal structures known to support superconductivity. The active planar iron layers common to all superconducting compounds with iron ions shown in red and pnictogen/chalcogen anions shown in gold. Ref. [35]

are shown in Fig. 1.1. ¹

The key structural element contributing the most to the levels close to the Fermi energy is a layer consisting of a square lattice of Fe atoms. Each Fe atom is surrounded by tetrahedrally coordinated pnicogens (Pn) or chalcogens (Ch). The Fe layers are sequenced with buffer layers between, with the 11-type being an exception.

1.2.2 Generic doping phase diagram: comparison to cuprates

The layered structure of FeSC resembles layered structure of the other family of high T_c superconductors, the cuprates, in which dominant contribution to the electronic structure is made by CuO plane. The similarity between these two families can be found

¹Reprinted figure with permission from J. Paglione and R. L. Green, Nature Physics 6, 645 (2010). Copyright (2010) by Nature Publishing Group.

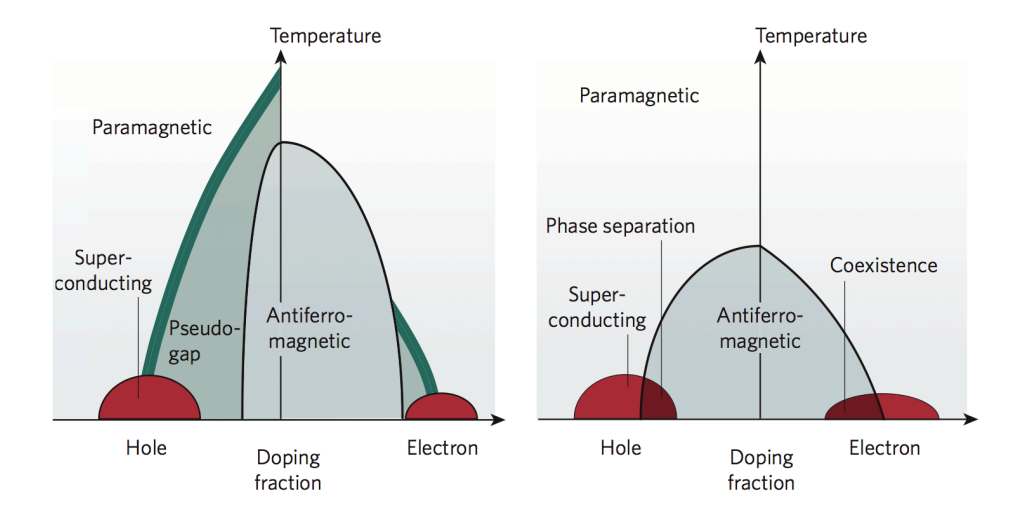


Figure 1.2 Schematic phase diagram of copper-oxide-based (left) and the 122 family of iron-based superconductors (right). Ref. [36]

also in the doping phase diagrams in Fig. 1.2. ² The parent undoped compounds in both cases are magnetically ordered. However, in case of the cuprates this magnetic state is the Mott insulator while in FeSC it is semimetal. In both cases, superconductivity is induced by doping, and maximum T_c is observed close to the point where magnetism vanishes. As we discussed in Preface, it was suggested that it coincides with a magnetic QCP. With further doping increase, T_c goes down, and superconductivity vanished in most of FeSC before full substitution.

1.2.3 Magnetic structures

In-plane commensurate antiferromagnetic structure of FeSC are depicted in Fig. 1.3 for (a) the 111-, 1111-, and 122-type FeAs-based parent compounds and for (b) FeTe. The Fe atoms are represented as filled circles in both panels.

Following the description in Ref. [31], for the 111-, 1111-, and 122-type FeAs-based compounds, the Fe-square lattice at temperatures $T > T_s$ (a = b) becomes slightly distorted (a > b) for $T < T_s$. Here T_s stands for structural phase transition from high-

 $^{^2}$ Reprinted figure with permission from I. I. Mazin, Nature 464, 183 (2010). Copyright (2010) by Nature Publishing Group.

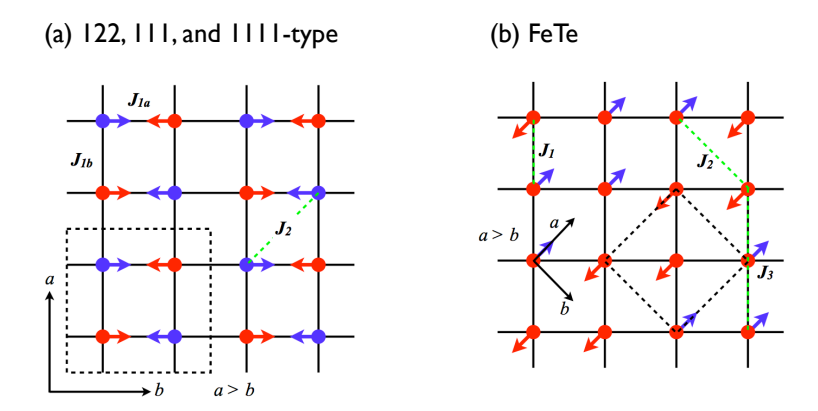


Figure 1.3 Magnetic structure of Fe-based superconductors. Ref. [31]

temperature orthorhombic to low-temperature tetragonal structure. The basal plane orthorhombic unit cell is shown as the dashed box in Fig. 1.3. The room temperature tetragonal basal plane has edges that are smaller by a factor of $\sqrt{2}$ and are rotated by 45° with respect to the orthorhombic axes. The direction of collinearly ordered moments is in the a-b plane of the orthorhombic structure and is along the longer aaxis. The red and blue arrows represent spins on the red and blue sublattices of Fe atoms, that respectively consist of next-nearest-neighbors. Each sublattice is individually antiferromagnetically ordered in a commensurate collinear Ising-like configuration. When both spin lattices are considered together, this intralattice ordering causes spin stripes to form along the b-axis, which also causes magnetic frustration between the two sublattices irrespective of whether the intersublattice coupling is ferromagnetic or antiferromagnetic. The nearest-neighbor exchange coupling constants J_{1a} and J_{1b} (between sublattices) and the next-nearest-neighbor coupling constant J_2 (within each sublattice) in a local moment description of the orthorhombic phase are shown. An anisotropy between J_{1a} and J_{1b} is needed for the system to choose whether the stripe orientation is vertical (as observed) or horizontal.

The magnetic structure in FeTe is different from the other Fe-based compounds as shown in Fig. 1.3(b). It is of commensurate collinear in-plane antiferromagnetic diagonal

double stripe structure. The tetragonal/monoclinic basal plane a- and b-axes and basal plane crystallographic unit cell outline (dashed lines) are indicated. J_1 , J_2 , and J_3 are the nearest, next nearest, and next next nearest neighbor exchange interactions.

1.2.4 Fermi surfaces

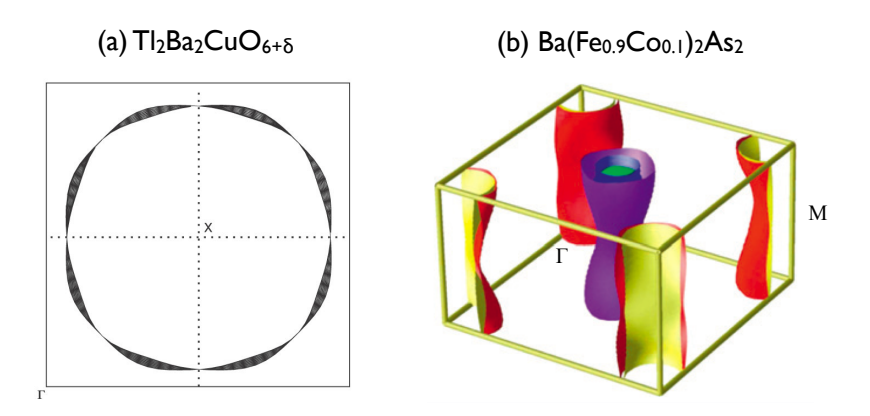


Figure 1.4 (a) The ab-plane projected Fermi surface of $\text{Tl}_2\text{Ba}_2\text{CuO}_{6+\delta}$. The shaded region represent small warping along c-axis [37]. (b) Calculated Fermi surfaces of BaFe_2As_2 with 10% substitution of Co using the folded BZ representation with two Fe per unit cell. The hole-like Fermi surfaces (purple and blue) are centered around the Γ point $(k_x = 0, k_y = 0)$ and the electron-like surfaces are around the \mathbf{M} point (π, π) [38].

The Fermi surface of the over-doped copper oxides is a single cylinder open along the c-axis, as shown in Fig. 1.4(a) for $\text{Tl}_2\text{Ba}_2\text{CuO}_{6+\delta}$. The Fermi surface seems to change in the underdoped compounds [37, 39]. The bandstructure calculations for FeSC predict complicated Fermi surfaces with up to five sheets. These sheets have cylindrical shape open along the c-axis, however, much more warped compared to the cuprates. This difference in warping leads to much smaller electrical anisotropy of the FeSC compared to the cuprates. Anisotropy sensitively depends on the pnictogen height with respect to the Fe-layer. The Fermi surfaces of FeSC shown, in Fig. 1.4(b), consist of the hole-like Fermi surfaces centered at the Γ point $(k_x = 0, k_y = 0)$ and the electron-like surfaces centered at the M point (π, π) .

1.2.5 Temperature-concentration Phase diagrams

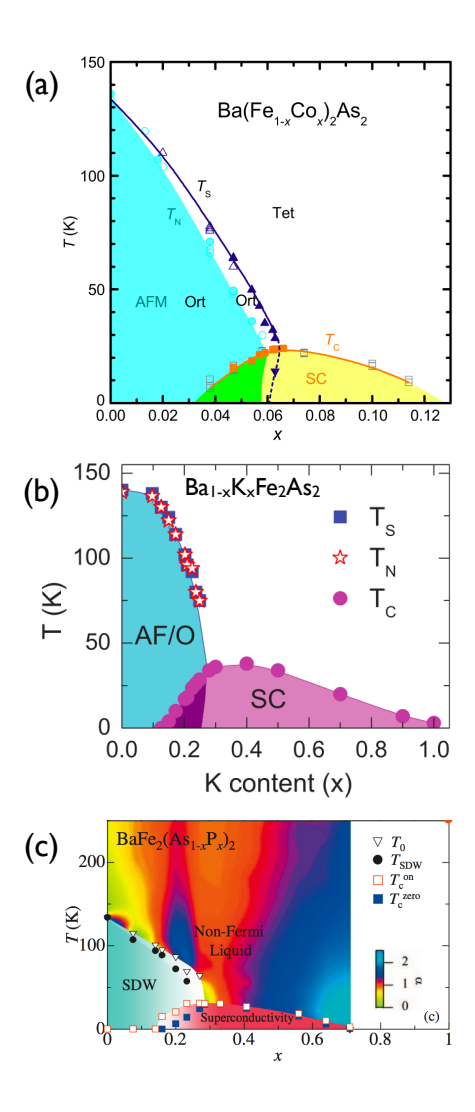


Figure 1.5 Temperature-concentration phase diagrams of (a) Ba(Fe_{1-x}Co_x)₂As₂ [40] (b) Ba_{1-x}K_xFe₂As₂ [41] (c) BaFe₂(As_{1-x}P_x)₂ [42].

The generic phase diagram of FeSC shown in Section 1.2.2 catches the main features of most materials. However, the details are different in different families. These differences are illustrated in Fig. 1.5 and Fig. 1.6. Top panel of Fig. 1.5 shows the T-x phase diagram for electron doped Ba(Fe_{1-x}Co_x)₂As₂.³ Substitution of Co for Fe suppresses both the high-temperature tetragonal-to-orthorhombic as well as paramagnetic to anti-

³Reprinted figure with permission from S. Nandi *et al.*, Physical Review Letter 104, 057006 (2010). Copyright (2010) by the American Physical Society.

Both transitions are completely suppressed for x > 0.06. Superconductivity is observed starting from $x \ge 0.038$ and for some range coexists with bulk magnetic phase. Superconductivity disappears for $x \sim 0.15$, maximum $T_c \approx 23$ K is observed for $x \approx 0.07$. The orthorhombicity (or orthorhombic distortion) defined as (a-b)/(a+b), where a and b are in-plane lattice parameters, decreases with increasing doping. The relative decrease in the orthorhombicity below T_c is pronounced and increases with increased doping [40]. In sample with x = 0.063 the orthorhombicity decreases below T_c , and the low-temperature structure returns to tetragonal symmetry below T_c [40]. For x = 0.066, no transition to the orthorhombic structure was observed, defining an upper Co concentration limit for the tetragonal-to-orthorhombic phase transition. The extension of the tetragonal-to-orthorhombic phase line into the superconducting dome is represented by the dashed line in the figure. Similarly, high-resolution thermal expansion measurements on detwinned single crystals of YBa₂Cu₃O_{7- δ} also found a change in the orthorhombic distortion at T_c , but smaller than the present case by approximately 2 orders of magnitude [43].

Similar phase diagrams with coexisting magnetism and superconductivity in the underdoped range is observed in hole-doped $Ba_{1-x}K_xFe_2As_2$ [44, 41] as well as in isoelectron doped 122 systems. The phase diagram of $Ba_{1-x}K_xFe_2As_2$ established based on resistivity, magnetization, and neutron powder diffraction experiments is shown in Fig. 1.5(b) taken from Ref. [41].⁴ With K-doping, the tetragonal to orthorhombic structural transition temperature T_s decreases until it is fully suppressed for x > 0.25. The SDW order and orthorhombic order are coincident and first order unlike electron-doped compounds. Superconductivity was observed for all samples with $x \ge 0.15$. Superconducting transition temperatures peak at ~ 38 K for x = 0.4. Interestingly, the end member (x = 1), heavily hole-doped KFe₂As₂, exhibits superconductivity with low $T_c = 3.4$ K.

Figure 1.5(c) displays the T-x phase diagram of isoelectric doped $BaFe_2(As_{1-x}P_x)_2$

⁴Reprinted figure with permission from S. Avci *et al.*, Physical Review B 85, 184507 (2012). Copyright (2012) by the American Physical Society.

system taken from Ref. [42].⁵ Both structural and magnetic transition temperatures decrease rapidly with increasing x, and there is clear separation between them (0.14 $\leq x \leq 0.30$). Near $x \approx 0.30$, the magnetic transition disappears. The superconducting transition shows a maximum $T_c = 31$ K at x = 0.26, and superconductivity is not observable for x > 0.7. The phase diagram in this system resembles that of the pressure dependence of BaFe₂As₂, indicating that the isoelectron substitution of P for As causes similar effects on the system as mechanical pressure. Normal state transport properties exhibit the non-Fermi liquid behavior over wide temperature domain near optimally doped regime.

Isoelectron doping effect on Fe-site was also studied in Ba(Fe_{1-x}Ru_x)₂As₂ [45]. The structural and magnetic phase transition is also suppressed upon Ru-doping, but unlike P-doping and electron-doping on Fe-site there is no detectable separation between. Superconductivity is stabilized at low temperatures for x > 0.2 and appears more gradual as compared to electron-doping on Fe-site, which resembles the effect of mechanical pressure. The superconducting region is dome-like with maximum $T_c = 16.5$ K.

Similar phase diagrams were also observed in Co-doped NaFeAs. The isostructural LiFeAs which does not show apparent magnetism corresponds to slightly overdoped case according to the pressure study [46].

The structural and magnetic phase diagram in CeFeAsO_{1-x}F_x shown in Fig. 1.6(a) is taken from [47]. ⁶The red circles indicate the onset temperature of the tetragonal-to-orthorhombic phase transition. The black squares and green triangles designate the Néel temperatures of Fe and Ce, respectively, as determined from neutron measurements. The superconducting transition temperatures are from onset T_c of the resistivity measurements taken from [49]. The open triangles are T_c determined from susceptibility measurements. The inset in (d) shows the F-doping dependence of the Fe moment as

 $^{^5}$ Reprinted figure with permission from S. Kasahara *et al.*, Physical Review B 81, 184519 (2010). Copyright (2010) by the American Physical Society.

⁶Reprinted figure with permission from J. Zhao, Nature Materials 7, 953 (2008). Copyright (2010) by Nature Publishing Group.

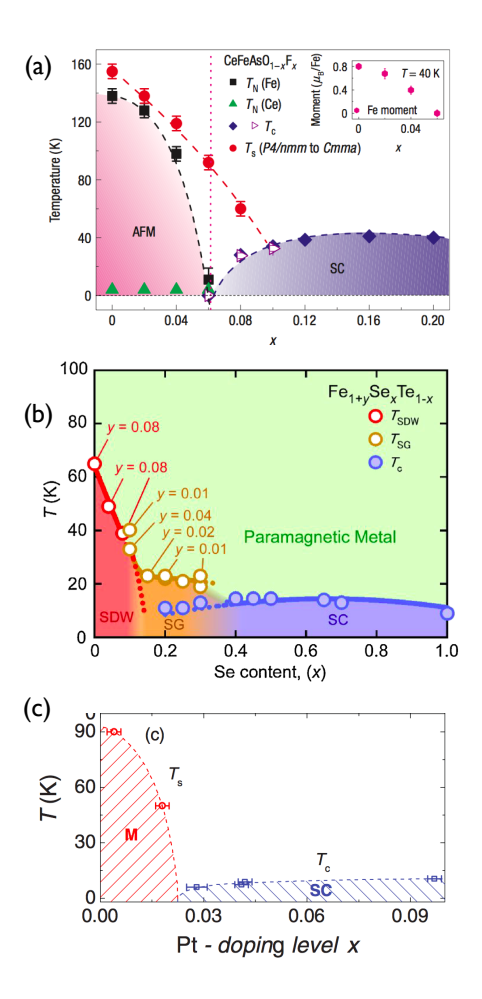


Figure 1.6 Temperature-concentration phase diagrams of (a) CeFeAsO_{1-x}F_x [47] (b) Fe_{1+y}Se_xTe_{1-x} [48] (c) Ca₁₀(Pt₃As₈)((Fe_{1-x}Pt_x)₂As₂)₅ [33].

determined from the intensity of the (1,0,2) magnetic peak at 40 K, where the influence of the Ce moment on the Fe magnetic Bragg peak intensity can be safely ignored.

The T-x phase diagram for $Fe_{1+y}Se_xTe_{1-x}$ based on the bulk susceptibility data obtained from the single crystal samples is shown in Fig. 1.6(b) taken from [48].⁷ The values of x and y are nominal values. The phase digram clearly shows the trends and the existence of three distinct phases; the antiferromagnetic phase for $x \leq 0.1$, the bulk superconducting phase for $x \leq 0.4$, and the intermediate spin-glass phase. The phase diagram in this work clearly shows that the long-range ordered SDW phase is non-

⁷Reprinted figure with permission from N. Katayama *et al.*, Journal of the Physical Society of Japan 79, 113702 (2010). Copyright (2010) by the Physical Society of Japan.

superconducting while an earlier paper by Fang et al. [50] reported superconductivity in the same phase based on powder samples, problems with contamination by oxide phases in that work have already been pointed out by McQueen et al. [51]. In the intermediate phase, some samples showed partial superconductivity below $T_c \sim 11$ K as presented in the figure, while others were non-superconducting down to 1.4 K.

The T-x phase diagram of $Ca_{10}(Pt_3As_8)((Fe_{1-x}Pt_x)_2As_2)_5$ is shown in Fig. 1.6(c). In this system, the magnetic (M) and superconducting (SC) phases are clearly separated as a function of Pt doping (x). T_s is determined by electronic transport measurements [34], below which an NMR study found evidence for a stripe type magnetism similar to the 122 systems. However, detailed magnetic structure has not been determined to date.

1.2.6 Superconducting mechanism and order parameter

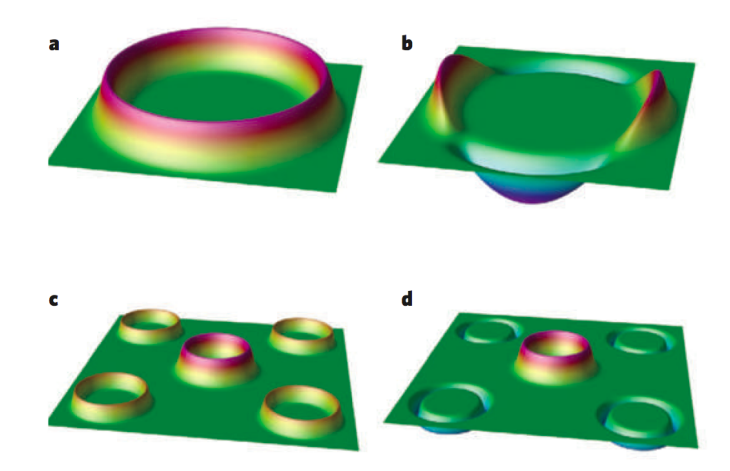


Figure 1.7 A schematic representation of the superconducting order parameter in (a) a conventional s-wave superconductor, (b) d wave in copper oxides, (c) a two-band s wave with the same sign, so-called s_{++} in MgB₂, and (d) s_{\pm} wave, which is thought to be the case in Fe-based superconductors. Figures are reprinted with permission from I. I. Mazin, Nature 464, 183 (2010). Copyright (2010) by Nature Publishing Group.

As we mentioned in Preface, the original BCS theory predicts superconducting gap which is constant on the Fermi surface. This s-wave state is schematically illustrated

in Fig. 1.7(a). This simplest BCS gap function does not describe all phonon mediated superconductors. It was recognized that superconducting gap can strongly vary between different Fermi surface sheets as observed, for example, in MgB₂ as shown in (c). In addition to this, in some materials, gap strongly varies over the Fermi surface as seen, for example, in LuNi₂B₂C [52, 53]. It was suggested that this gap anisotropy is arising from nesting on the Fermi surface [53]. But, importantly, in all phonon mediated superconductors, the gap function does not change sign. In the cuprates, the superconducting gap function changes sign over the Fermi surface [36]. This sign change is experimentally proven by corner junction phase sensitive experiments [19]. Figure 1.7(b) shows schematically the superconducting gap function of the cuprates. Figure 1.7(c) shows the superconducting gap structure of MgB₂. This material has strong variation of gap magnitude between different sheets of the Fermi surfaces [54, 55]. This represents socalled multiband superconductivity. Note, however, the superconducting gap function is of same sign on different Fermi surfaces [36, 56]. In Figure 1.7(d), we show the superconducting gap function suggested for FeSC in the s_{\pm} -wave state [57]. The superconducting gap has different magnitude on different Fermi surfaces, but most importantly the gap function changes sign between Fermi surfaces. Experimental verification of this suggestion and its contrast with conventional s-wave were at the forefront of the studies of the superconducting gap in FeSC.

One of key experiments establishing electron-phonon mechanism of coupling was isotope effect on T_c . The conventional isotope effect has been reported in SmFeAsO_{1-x}F_x and Ba_{1-x}K_xFe₂As₂ [58]. This observation may indicate some contribution of electron-phonon interaction into pairing. However, the magnitude of the effect has been highly controversial [58, 59], which is not unusual for complex materials contrary to a simple case of MgB₂ [16]. The observed isotope effect may be spurious, it may result from subtle changes in the structural properties adding more weight on possibility of electronic-originated superconductivity.

In the proposed s_{\pm} state for FeSC, the pairing is induced by the repulsive Coulomb interactions which lead to effective attraction between two electrons provided gap function changes sign. This sign change leads to neutron resonance peak at the wavevector connecting Fermi surfaces with opposite signs of order parameter, i.e., $\Delta_k = -\Delta_{k+Q}$. Here Q is a wavevector of spin resonance peak which can be explicitly detected in inelastic neutron scattering experiment. Such resonance peak has been indeed observed in the cuprates and 115 compounds [60]. For FeSC, this resonance peak was first detected in $\mathrm{Ba}_{0.6}\mathrm{K}_{0.4}\mathrm{Fe}_2\mathrm{As}_2$ with 14 meV energy transfer with $Q=1.15~\mathrm{\AA}^{-1}$ [61].

Although a firm conclusion about the pairing symmetry in FeSC would require a direct measurement of the sign-changing order parameters by phase sensitive experiments [62], measurements of basic thermodynamic and transport properties have provided convincing results for the nodal structure of the superconducting gap. The magnitude of the jump in heat capacity experiments $\Delta C_p/\gamma_n T_c$ is expected to be $\Delta C_p/\gamma_n T_c = 1.43$ in a weak-coupling BCS superconductor. $\Delta C_p/\gamma_n T_c \approx 2.5$ was observed in (Ba,K)Fe₂As₂ indicating strong-coupling full-gap superconductivity, and $\Delta C_p/\gamma_n T_c \approx 0.5$ in KFe₂As₂ which is much smaller than the weak-coupling limit. Such a low value could be attributed to multigap nature of superconductivity [63, 64].

Bud'ko, Ni, and Canfield (BNC) proposed a correlation $\Delta C_p/T_c = a T_c^2$ ($a \sim 0.56$ mJ/mole-K⁴) for various doped BaFe₂As₂ [65]. This clear deviation from conventional BCS-like behavior was interpreted as consequence of strong pair-breaking [66, 67], coexistence of superconductivity and magnetism [68], and superconductivity arising from non-Fermi-liquid quantum critical metal [69].

The most relevant experiments to study the superconducting gap structure include heat capacity, thermal conductivity, and London penetration depth. Knowledge of their low temperature behavior, provided precisely measured, gives insight into the nodal structure of the superconducting gap. Conventional superconductors exhibit T-exponential behavior in these quantities at the lowest temperature limit due to thermally

activated quasiparticles over isotropic superconducting gap. Magnetic field-dependence is also consistent with the existence of isotropic energy gap. For example, H-linear field-dependence of C_p/T is caused by quasiparticle state in the vortex core but not in the bulk. On the other hand, unconventional superconductors often show a power-law behavior, T^n , in both temperature-and field-dependence over a wide range of temperatures. Temperature and field dependence of these quantities can be associated with a certain structure of the superconducting gap.

Measurements of heat capacity as a function of temperature and magnetic field provide valuable clues about pairing symmetry. While conventional superconductors show T-exponential, unconventional paring exhibit a power-law behavior of $C_p(T)$ at low temperatures. For instance, $\Delta C_p(T) \sim T^2$ would imply line-nodal superconducting gap in clean materials [70], but it is often difficult to verify experimentally due to other contributions, such as phonons and the Schottky anomaly. Nevertheless, T^2 -behavior was observed in Ba(Fe,Co)₂As₂ [71, 72]. On the other hand, field-dependence of $C_p/T = \gamma$ could be more useful. H-linear variation of $\gamma(H)$ is consistent with a fully gapped superconductor. For d-wave, on the other hand, $\gamma(H)$ varies as $H^{1/2}$ in clean limit [73] or $H \log H$ in dirty limit [74] due to the so-called Volovik effect arising from the Doppler shift of the low-energy nodal quasiparticles in the superflow field of the vortex line. Similar field dependence is expected in the s_{\pm} state with scattering, and $\gamma \sim H^{1/2}$ was observed in the 1111 system. In a hole doped BaFe₂As₂, an observation of $\gamma \sim H$ was attributed to fully gapped superconductivity. However, field dependence of γ in electron-doped BaFe₂As₂ compounds remains controversial to date [75, 76].

Temperature-and field-dependence of electronic thermal conductivity κ is also a characteristic of the nodal structure of the superconducting gap. Residual linear term in the electronic thermal conductivity, $\kappa/T|_{T=0}$ is negligible in a fully gapped superconductor, and a finite residual value would imply nodes in the gap. Field dependence of κ is H-exponential for a full gap, and $\kappa/T \sim H^{1/2}$ for a nodal gap. Most comprehensive

and convincing results on temperature-and field-dependent κ can be found in BaFe₂As₂ systems mostly because of the availability of high quality single crystals although thermal conductivity is less sensitive to impurities compared to other measurable quantities in the superconducting state. At the optimal doping, in both electron-and hole-doped BaFe₂As₂, there is no measurable residual electronic thermal conductivity in both in- and out-of-plane directions [77, 78, 79]. However, a significant residual linear term was measured in electron doped BaFe₂As₂ with concentrations at both edges of superconducting-dome of T-x phase space [78]. Measurements in KFe₂As₂ which is effectively the end member of hole-doped BaFe₂As₂ revealed d-wave gap structure, but it is still an open question whether it is a symmetry imposed d-wave or a state with accidental nodes in multi s-wave gap structure. On the other hand, isovalent substitution of As by P in BaFe₂As₂ shows a nodal gap structure over all superconducting concentrations.

1.3 London penetration depth

1.3.1 Theory of the London penetration depth

Concept of the penetration depth of weak magnetic field into a superconductor was first introduced by F. and H. London brothers to account for the Meissner-Ochcenfeld effect. A superconductor in weak magnetic field generates the so-called supercurrent to expel the magnetic field out of the bulk. The supercurrent is distributed near surfaces of the superconductor within a characteristic length scale which is now called the London penetration depth. For superconductor with a spherical Fermi surface (electron gas), the penetration depth at $T \ll T_c$ is given by

$$\lambda^2 = \frac{mc^2}{4\pi n_s e^2} \tag{1.1}$$

where n_s is a density of superconducting electrons which are responsible for the occurrence of supercurrent, and the value of n_s is of the order of normal state electronic density. Although there is no explicit temperature dependence in this equation, this quantity has a minimum value at T=0 and diverges at the superconducting phase transition as temperature is raised.

In a semiclassical picture [80], the temperature-dependent London penetration depth provides basic information about the microscopic pairing state of a superconductor. In a superconductor with an arbitrary electronic structure, the anisotropic London penetration depth is given by

$$\lambda_{ii}^2 = \frac{c}{4\pi \mathbf{T}_{ii}} \tag{1.2}$$

where $\mathbf{T}_{ii} = \mathbf{T}_P + \mathbf{T}_D$ is proportional to superfluid density. Here \mathbf{T}_P and \mathbf{T}_D are paramagnetic and diamagnetic responses, respectively, of thermally activated quasi particles and are given by

$$\mathbf{T}_{P} \approx \frac{e^{2}}{2\pi^{3}\hbar c} \oint dS_{F} \frac{\mathbf{v}_{F} \mathbf{v}_{F}}{v_{F}} \int_{\Delta_{k}}^{\infty} dE_{k} \left(-\frac{\partial f}{\partial E_{k}} \right) \frac{E_{k}}{\sqrt{E_{k}^{2} - \Delta_{k}^{2}}}$$
(1.3)

$$\mathbf{T}_D = \frac{e^2}{4\pi^3\hbar c} \oint dS_F \frac{\mathbf{v}_F \mathbf{v}_F}{v_F} \tag{1.4}$$

where Δ , E_k , and v_F are superconducting gap function, energy measured from E_F , and Fermi velocity, respectively. As T goes to zero, \mathbf{T}_P decreases to zero as well, and as T is raised to T_c , \mathbf{T}_P approached \mathbf{T}_D . If Δ_k is isotropic, then the anisotropy of \mathbf{T}_P is temperature-independent and its anisotropy is the same as the anisotropy of \mathbf{T}_D . On the other hand, if Δ_k is anisotropic, then the anisotropy of \mathbf{T}_P is affected by the anisotropies of both E_k and Δ_k , and is temperature-dependent. Therefore, according to this picture, the spatial components of the London penetration depth can be computed for a general Fermi surface geometry and an arbitrary momentum dependent superconducting gap function. In other words, temperature dependence of the London penetration depth probes the angular variation of the superconducting order parameter when its temperature dependence is measured precisely down to low enough temperatures. Practically, at low temperatures, below $0.3T_c$, where the superconducting gap can be considered as constant, the measured penetration depth can be well described by a power-law function, $\Delta \lambda(T) = AT^n$. The pre-factor A is closely related to $\lambda(0)$, and the exponent n

has characteristic values depending on the symmetry of the superconducting gap. The temperature dependence of the penetration depth has been well accounted for two wellknown gap symmetries.

First, in s-wave superconductors with isotropic order parameter the dependence is exponential and is given as

$$\frac{\Delta\lambda(T)}{\lambda(0)} = \sqrt{\frac{\pi\Delta(0)}{2k_BT}} \exp\left(-\frac{\Delta(0)}{k_BT}\right) \tag{1.5}$$

where $\Delta(0)$ is one half of the superconducting energy gap at T=0. Second, for a nodal superconductor, in particular with line nodes in a cylindrical Fermi surface, the penetration depth in clean limit varies as T-linear and is given by

$$\frac{\Delta\lambda(T)}{\lambda(0)} = \frac{2\ln 2}{\alpha\Delta(0)}T\tag{1.6}$$

where α depends on the functional form of Δ near nodes [81]. Unlike isotropic superconductors, temperature variation of λ in anisotropic superconductors is rather easily affected by impurity scattering. In a dirty line-nodal superconductor, penetration depth may vary as T-quadratic at $T \ll T_c$ due to residual in-gap states introduced by impurities. The penetration depth in this situation can be characterized by [82]

$$\Delta\lambda(T) = a \frac{T^2}{T + T^*} \tag{1.7}$$

where T^* is a characteristic temperature which is proportional to impurity scattering in the system, and a is a constant of order $\lambda(0)$.

Fig. 1.8 shows examples of $\Delta\lambda(T)$ in typical superconductors (see chapter 2 for details). The penetration depth was measured by using a tunnel diode resonator technique in Ames Laboratory. Penetration depth was normalized as $\Delta\lambda(T)/\Delta\lambda(0.5T_c)$ so that $\Delta\lambda(T)$ in different superconductors can be easily compared. Nb, a conventional superconductor, shows almost temperature independent lambda up to $T_c/3$. MgB₂ multi-gap s-wave superconductor shows clear saturation in $T \to 0$ limit, but clearly distinguishable

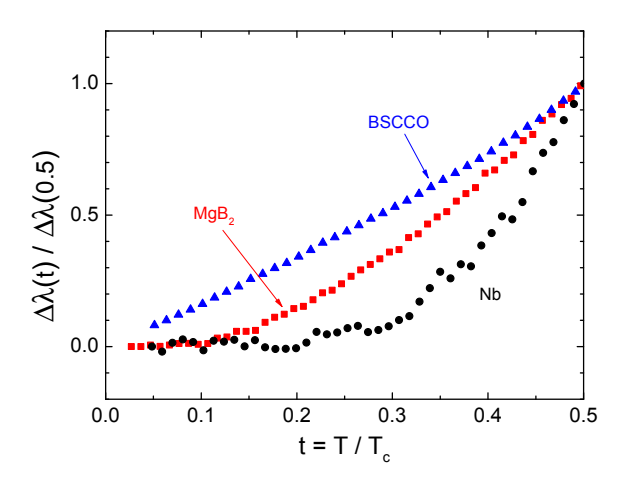


Figure 1.8 Experimental London penetration depth in Nb, MgB₂, and BSCCO.

from single gap s-wave in Nb. A d-wave superconductor, $\mathrm{Bi_2Sr_2CuO_{6+x}}$, shows linear temperature dependence.

Knowledge of the superconducting gap structure obtained from measured $\Delta\lambda(T)$ at the lowest temperatures can be extended to full superconducting T-domain by studying superfluid density. Superfluid density can be calculated from the London penetration depth by using a relation;

$$\rho_s(T) = \frac{\lambda_{ii}^2(0)}{\lambda_{ii}^2(T)} \tag{1.8}$$

For a conventional superconductor, the superfluid density at low temperatures can be found by

$$\rho_s = 1 - \sqrt{\frac{2\pi\Delta(0)}{k_B T}} \exp\left(-\frac{\Delta(0)}{k_B T}\right)$$
(1.9)

For $d_{x^2-y^2}$ pairing superconductors, the superfluid density at low temperatures is given by

$$\rho_s = 1 - \frac{2\ln 2}{\Delta(0)}T. \tag{1.10}$$

As shown above, temperature dependence of the superfluid density at low temperatures are the same as that of the London penetration depth. The theoretical superfluid density for these two special cases are plotted for full superconducting temperature range in Fig. 1.9.

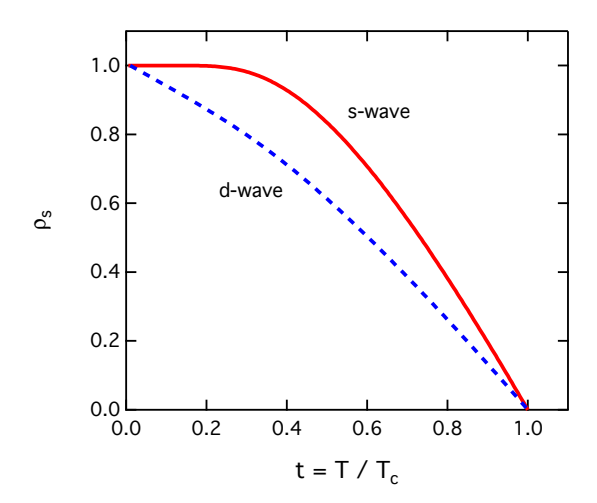


Figure 1.9 Theoretical superfluid density of s-wave and d-wave.

1.3.2 London penetration depth in Fe-based superconductors

When this project was starting, very little was known about London penetration depth in FeSC, and the reports were very controversial. Whereas exponential temperature dependence was reported in SmFeAsO_{1-x}F_x [83] and (Ba,K)Fe₂As₂ [84], studies of $\Delta\lambda(T)$ in Ba(Fe,Co)₂As₂ [85, 86], SmFeAsO_{1-x}F_x [83], and LaFeAsO_{1-x}F_x [87] found a power-law $\Delta\lambda \sim T^n$ where $2 \leq n < 2.5$, which is not consistent with presence of line nodes in the superconducting gap. In R1111, measured $\Delta\lambda(T)$ could be modified due to localized magnetic moment of R, which makes analysis rather difficult [88, 83, 87]. For s_{\pm} state, it was pointed out that the effect of disorder may change exponential T-variation of $\Delta\lambda(T)$ to a power-law behavior with exponent even below 2, down to 1.6 [89, 90]. But stoichiometric LaFePO exhibits $\Delta\lambda \sim T^{1.5}$ which can not be reconciled with fully gapped superconductivity [91, 92].

On the other hand, systematic studies of doping evolution of thermal conductivity found strong doping induced gap anisotropy change in BaCo122. This doping evolution was not expected in any model. It was natural to ask if this is a general trend for FeSC. Considering significant effect of disorder scattering, it was very important to study stoichiometric materials. Our measurements on stoichiometric LiFeAs revealed

true exponential $\Delta\lambda(T)$ [93, 94]. In a similar stoichiometric compound LiFeP, $\Delta\lambda(T)$ was consistent with the presence of nodes in the superconducting gap [95]. This difference may be suggestive that evolution of gap anisotropy with doping does not depend on disorder scattering and may be intrinsic effect. Studies of $\Delta\lambda(T)$ in another stoichiometric superconductor, KFe₂As₂, finding gap nodes, support this view.

CHAPTER 2. EXPERIMENTAL

2.1 Tunnel diode resonator technique for London penetration depth measurements

2.1.1 Principles of tunnel diode resonator

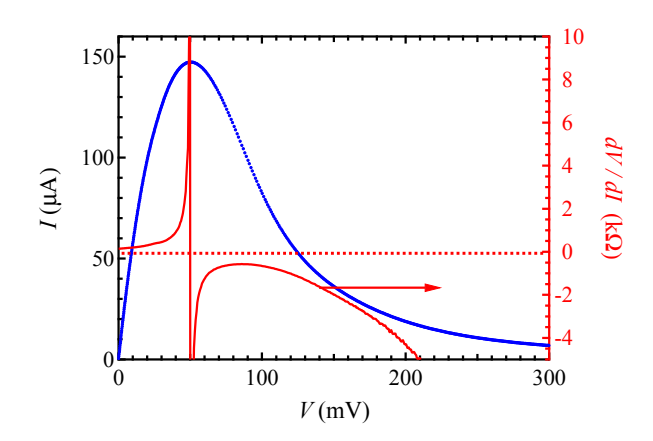


Figure 2.1 (left axis) IV characteristic curve of a tunnel diode. (right axis) Differential resistance dV/dI.

A tunnel diode resonator (TDR) is an electronic circuit that generates a highly stable oscillation with a radio frequency of order typically 1-100 MHz. The key element is a self-oscillating LC tank circuit powered by a tunnel diode or Esaki diode. The resonance frequency is determined by $f_0 = 1/\sqrt{LC}$.

The tunnel diode is composed of two different types of heavily doped semiconductors: p-and n-type. When these two semiconductors are spatially very closely positioned with the depletion layer being approximately 100 Å, valence band of p-type and conduction

band of n-type overlap, and such thin layer allows electric current flow even at zero bias voltage by quantum tunneling effect. When an applied forward bias voltage reduces the overlap enough, it exhibits a characteristic of negative differential resistance as shown in Fig. 2.1, which is the most crucial property of the diode for the resonator technique.

Either the inductor and capacitor circuit elements of the LC tank circuit can be used as the experimental probe incorporating the sample as part of the element. Relevant magnetic and electric properties can be studied by utilizing the inductor and the capacitor, respectively. Various usages of TDR with a capacitor as a probe can be found in Ref. [96, 97]. In this section, we will focus on measurements based on the inductive coupling between a probe coil and a specimen. In such a case, the frequency shift δf due to change of the inductance δL can be related by;

$$f_0 + \delta f = \frac{1}{2\pi\sqrt{(L+\delta L)C}} = \frac{1}{2\pi\sqrt{LC}} \left(1 + \frac{\delta L}{L}\right)^{-1/2}.$$
 (2.1)

Inductance of a typical coil, for example ~ 10 mm long and ~ 2 mm wide with ~ 50 turns, is of order 1 μ H. By using a capacitor with 100 pF, $f_0 \approx 16$ MHz. Practical upper limit of change in inductance δL with an $1\times 1\times 0.1$ mm³ big sample is $\delta L \sim 10$ nH. In such cases, i.e., $\delta L \ll L$, the equation can be simplified;

$$\frac{\delta f}{f_0} \approx \frac{1}{2} \frac{\delta L}{L}.\tag{2.2}$$

 δL can be associated to change in dynamic magnetic susceptibility of the specimen. By definition,

$$L = \frac{d\Phi}{dt} \tag{2.3}$$

where Φ is magnetic flux penetrating through the inductor. For a long solenoid-coil without a sample, $\Phi = H_{ac} A l n = H_{ac} V_c n$. Here H_{ac} is the ac magnetic field produced by the coil, A is a cross sectional area of the coil, l is the longitudinal length of the coil, l is the number of turns per unit length, and V_c is the volume of the coil. For infinitesimal change in L caused by presence of a sample in the coil, we can write;

$$\delta L = \frac{d\delta\Phi}{dt}; \quad \frac{\delta L}{L} = \frac{\delta\Phi}{\Phi}.$$
 (2.4)

Since the change in L is purely due to change in magnetization of the specimen M,

$$\delta\Phi = M V_s n \tag{2.5}$$

where V_s is volume of the specimen. It can be shown;

$$\frac{\delta\Phi}{\Phi} = \frac{V_s}{V_c} \chi_{ac} \tag{2.6}$$

where $\chi_{ac} = M/H_{ac}$ is real part of magnetic susceptibility of the specimen. Finally the frequency shift can be written;

$$\frac{\delta f}{f_0} \approx -\frac{1}{2} \frac{V_s}{V_c} 4\pi \chi_{ac}. \tag{2.7}$$

The sensitivity of 0.001 ppm can be achieved when the circuit is constructed with care as well as all relevant electronics are properly used [97]. Application to measurements of superconducting penetration depth will be throughly discussed in the following section, and the sensitivity for this quantity can be as good as Å.

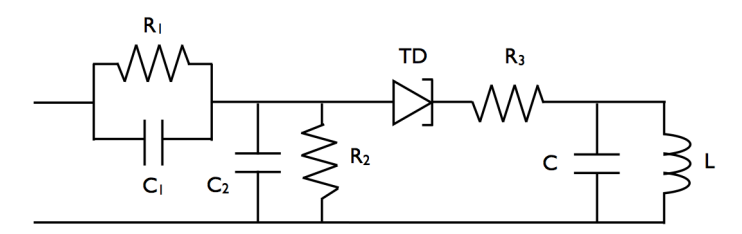


Figure 2.2 Circuit diagram for a prototypical TDR circuit.

A prototype circuit consists of eight components; a tunnel diode, an inductor coil, three capacitors, and three resistors. A schematic of this prototype is shown in Fig. 2.2. The combination of R_1 and R_2 should provide optimal bias voltage to the tunnel diode. Total impedance of R_3 , C, and L should be low enough so that it can be well compensated by the negative resistance of the diode. C_1 (~ 10 pF) allows small portion of signal to travel to the room temperature electronics. C_2 should be acting as a short circuit for the primary resonance oscillation. In-depth description of the circuit construction can be found in Ref. [97, 98, 99].

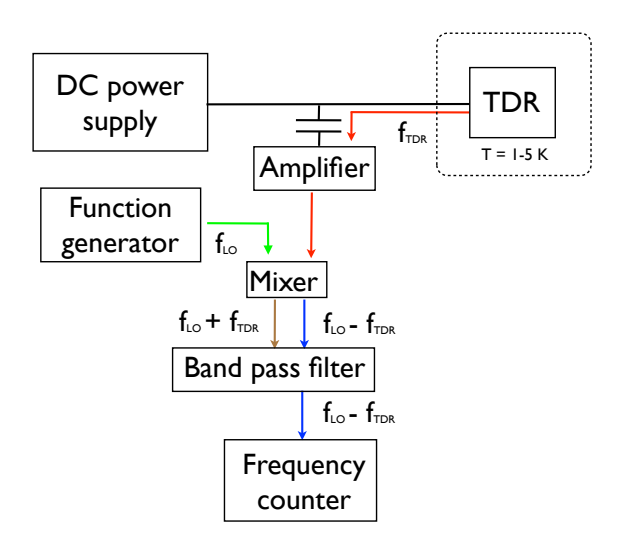


Figure 2.3 Schematic of TDR measurements.

Figure 2.3 is a schematic of typical measurements using a TDR technique at low temperatures. At proper forward bias voltage, the TDR produces a radio frequency f_{TDR} . The signal is usually amplified and mixed with a stable frequency f_{LO} which is set to be ~ 1 kHz higher than f_{TDR} , and finally the variation of the frequency shift $\Delta f = (f_{\text{LO}} - f_{\text{TDR}})$ is measured against time, temperature, or magnetic field.

For applications of a TDR circuit at low temperatures, it is important to achieve thermal stability of the circuit since the resonance frequency is highly dependent on the temperature of the circuit. It is recommended to stabilize the temperature of the circuit in order to minimize noise and background caused by thermal instability. The first published description of a TDR technique used in low temperatures was given in Ref. [96] where the technique was utilized to measure density of ³He under pressure.

For London penetration depth measurements below 500 mK down to \sim 50 mK, we developed a TDR setup in a dilution refrigerator (KelvinoxMX400, Oxford Instruments). Real images of the key parts of the setup are shown in Fig. 2.4. To minimize thermal conductance between the TDR stage and the sample stage, thin stainless steel separators were used between these two stages. The TDR stage is thermally connected to the

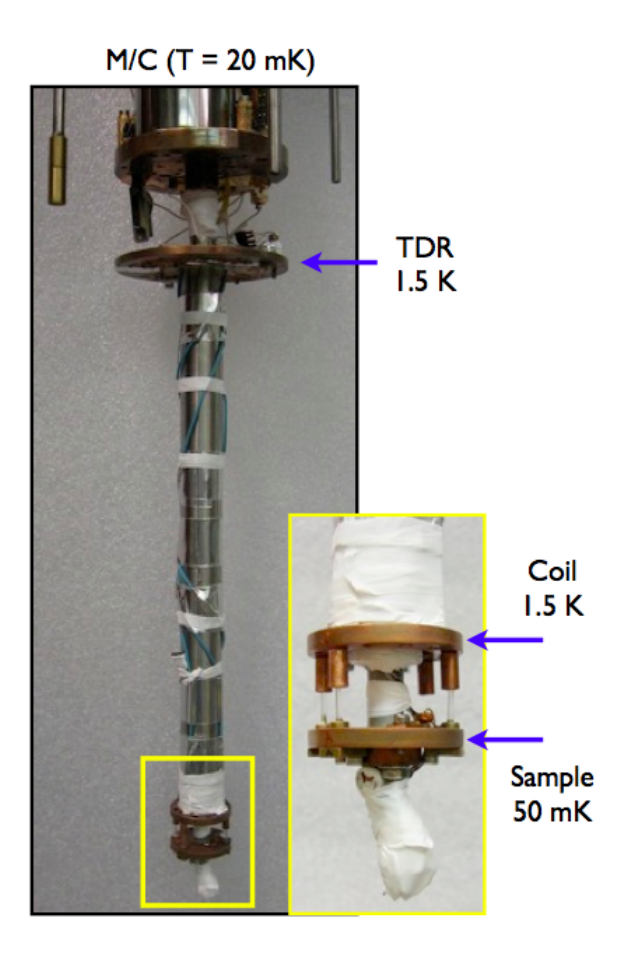


Figure 2.4 TDR setup on a dilution refrigerator.

Still stage with thick copper wires, and the temperature of the TDR stage was actively controlled. With the TDR operating at T=1.5 K, the temperature of the mixing chamber does not rise above 20 mK, and the base temperature of the sample stage can be as low as 40 mK. The circuit components used in the dil-fridge TDR setup are listed in Table 2.1. Two types of circuit configurations are used. For the first type, all eight components of the TDR circuit are located on the circuit temperature stage. For the second type, the circuit is split between two different stages. In this type, R_1 , R_2 , and C_1 are located at the Still stage, dissipating Joule-heat directly to the Still. This lowers the heat-load on the circuit stage, and the sample stage base temperature is lowered by ~ 10 mK, which can be significant for very low T_c superconductors. The noise level of

Table 2.1 TDR circuit components for setup in a dilution refrigerator. The circuit diagram is shown in Fig. 2.2. I_p is the current at the peak of IV curve of a tunnel diode. L is estimated with the number of turns $(25 \pm 2 \text{ turns})$ and the geometry of a cylindrical coil (2 mm long and 2.8 mm wide).

$I_p (\mu A)$	$R_1(\Omega)$	$R_2(\Omega)$	$R_3 (\Omega)$	C_1 (pF)	C_2 (pF)	C (pF)	$L (\mu H)$
100-150	300	200	50	39	10000	100	1-2

the two circuits is practically the same.

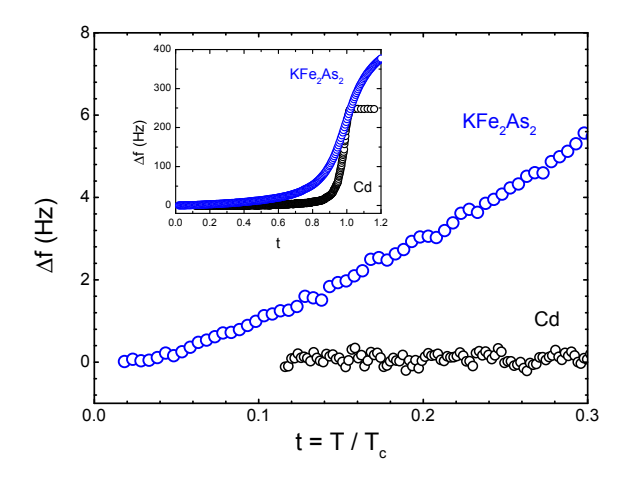


Figure 2.5 $\Delta f(T)$ vs. T/T_c in Cd $(T_c = 0.52 \text{ K})$ and KFe₂As₂ $(T_c = 3.4 \text{ K})$ measured by a TDR technique. T_c is determined at the maximum of $d\Delta f/dT$.

Figure 2.5 shows examples of Δf in superconducting materials: KFe₂As₂ and Cd. The frequency shift $\Delta f(T) = f(T) - f(T_{min})$ shows a clear difference between different types of superconductors, which will be discussed in-depth in the next section.

2.1.2 Calibration: conversion of measured Δf to $\Delta \lambda$

A superconducting sample is inserted into the center of an inductor coil of TDR. Assuming the sample is small enough so that the magnetic field produced by the inductor is homogeneous, changes in magnetic properties of the sample change the effective inductance due to a change in distribution of magnetic flux inside the coil. Precise analysis of

this change is crucial for application of the TDR technique to study London penetration depth.

Exact analytical solutions are known only for special geometries: an infinite bar or cylinder in longitudinal field, a cylinder in perpendicular field, a sphere, or a thin film. These solutions are not practical since most of samples are thin platelets. A general numerical method was developed to calculate magnetic susceptibility for plates and disks, but this method is somewhat difficult to apply in practice. In this section, we describe a numerical solution of the London equation in two dimensions for long slabs in a perpendicular field, and the results are then extended analytically to three dimensions. Using numerical results and analytical approximations, we derive a formula that can be used to interpret frequency-shift data obtained from TDR experiments [100].

The numerical results for a particular geometry is shown in Fig. 2.6.

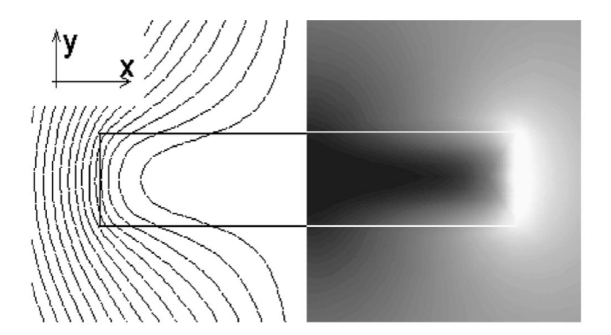


Figure 2.6 Right half: calculated distribution of the magnetic field in and around the sample of d/w = 1/5 and $\lambda/d = 0.5$. Black color represents B = 0. Left half: contour lines of the vector potential. Origin (x = 0, y = 0) is at the sample center. Ref. [100]

Consider a semi-infinite superconducting slab of width 2w in the x direction, thickness 2d in the y direction, and infinite in the z direction. A uniform magnetic field H_0 is applied along the y direction. In this two-dimensional geometry, $\mathbf{A} = (0, 0, A)$ and $\mathbf{H} = (\partial A/\partial y, -\partial A/\partial x, 0)$, and the London equation takes the form $\nabla^2 A = \lambda^{-2} A$. Figure 2.6 presents the distribution of the magnetic field in and around the sample with w/d = 5

and $\lambda/d = 0.5$.

Using the London equation for an isotropic superconductor

$$4\pi\lambda^2 j = -cA \tag{2.8}$$

and the definition of the magnetic moment

$$M = \frac{1}{2c} \int r \times j \, d^3r \tag{2.9}$$

we calculate numerically the magnetic susceptibility per unit volume (unit of surface cross section in a 2D case):

$$4\pi\chi = \frac{1}{dw\lambda^2 H_0} \int_0^d dy \int_0^w A(x,y)x \, dx \tag{2.10}$$

In finite geometry, there will be a contribution to the total susceptibility from the currents flowing on top and bottom surfaces. These currents are due to shielding of the inplane component of the magnetic field, $H_x = \partial A/\partial y$, appearing due to demagnetization.

It can be mapped onto the flat surface, so that the distribution of H_x is given by

$$H_x = \frac{H_0 r}{\sqrt{a^2 - r^2}} \tag{2.11}$$

where r = x/w and $a^2 = a + (2d/w)^2$.

Next, we find a simple analytical approximation to the exact numerical results by calculating the ratio of the volume penetrated by the magnetic field to the total sample volume. This procedure automatically takes into account demagnetization and nonuniform distribution of the magnetic field along sample top and bottom surfaces. The exact calculation requires knowledge of A(x,y) inside the sample or H(x,y) in a screened volume outside, proportional to w^2 . The penetrated volume is

$$V_p = \oint_S \frac{\lambda |H_s|}{H_0} ds, \tag{2.12}$$

where integration is conducted over the sample surface in a 3D case or sample cross-section perimeter in a 2D case. Using Eq. (2.11) for magnetic field on the top and

bottom surfaces and assuming $H_s = H_0/(1-N)$ on the sides we obtain

$$4\pi\chi = \frac{1}{1-N} \left[\frac{\lambda}{R} \tanh\left(\frac{R}{\lambda}\right) - 1 \right] \tag{2.13}$$

Here N is an effective demagnetization factor, and R is the effective dimension. Both depend on the dimensionality of the problem.

It was found numerically that in a 2D case, for not too large an aspect ratio w/d, $1/(1-N) \approx 1 + w/d$ [100]. Calculating the expelled volume as described above, the effective dimension R is given by

$$R_{2D} = \frac{w}{1 + \arcsin(1/a)}. (2.14)$$

The natural extension of this approach for the 3D disk of radius w and thickness 2d leads to $1/(1-N)\approx 1+w/2d$ and R is given by

$$\frac{w}{2R} = 1 + \left[1 + \left(\frac{2d}{w}\right)^2\right] \arctan\left(\frac{w}{2d}\right) - \frac{2d}{w}$$
 (2.15)

with w = ab/(a+b).

With typical size of samples for this technique, $0.8 \times 0.8 \times 0.1 \text{ mm}^3$, the calculated effective dimension is $R \approx 53 \ \mu\text{m}$ which is much greater than a typical value of penetration depth (~ 0.1 -1 μm). Using Eq. (2.13) and (2.15), we obtain for $\lambda \ll R$:

$$\frac{\Delta f}{f_0} = \frac{V_s}{2V_0(1-N)} \left(1 - \frac{\lambda}{R}\right) \tag{2.16}$$

where V_s is the sample volume, V_0 is the effective coil volume. The apparatus and sampledependent constant $\Delta f_0 = V_s f_0/[2V_0(1-N)]$ is measured directly by removing the sample from the coil. Thus, the change in λ with respect to its value at low temperature is

$$\Delta\lambda(T) = -\delta f(T) \frac{R}{\Delta f_0} \tag{2.17}$$

where $\Delta \lambda(T) = \lambda(T) - \lambda(T_{min})$ and $\delta f(T) = \Delta f - \Delta f(T_{min})$.

For the excitation field $H_{ac}||c$, screening currents flow only in the ab-plane, so Δf is only related to the in-plane penetration depth $\Delta \lambda_{ab}$. However, when the magnetic

field is applied along the ab-plane, screening currents flow both in the plane and between the planes, along the c-axis. In this case, Δf^{mix} contains contributions from both λ_{ab} and λ_c . For a rectangular sample of thickness 2t, width 2w and length l, mixed Δf is approximately given by

$$\frac{\Delta f^{\text{mix}}}{\Delta f_0^{\text{mix}}} = \frac{\Delta \lambda_{ab}}{t} + \frac{\Delta \lambda_c}{w} = \frac{\Delta \lambda^{\text{mix}}}{R}$$
 (2.18)

where R is the effective dimension that takes into account finite size effects. Knowing $\Delta \lambda_{ab}$ from the measurement with H_{ac} along c-axis and sample dimensions, one can obtain $\Delta \lambda_c$ from this equation.

This calibration procedure was applied to convert measured frequency shift by TDR technique to obtain temperature variation of London penetration depth throughout this thesis.

CHAPTER 3. USE OF RUTGERS RELATION FOR THE ANALYSIS OF THE SUPERFLUID DENSITY

The London penetration depth λ is one of the most important length scales of superconductors. The temperature dependent $\lambda(T)$ is a subject of many studies for various materials since, among other things, it provides information about the symmetry of the order parameter [101, 102]. Commonly, the superfluid density, $\rho(T) \equiv \lambda^2(0)/\lambda^2(T)$, is used for comparison with theory. Experimentally, some of the most sensitive techniques can reliably determine the temperature variation of the London penetration depth, $\Delta\lambda(T) = \lambda(T) - \lambda(0)$, while the determination of the absolute value, $\lambda(0)$, requires a separate effort. The techniques which are most widely used to estimate $\lambda(0)$ include muon spin rotation (μ SR) [103], infrared spectroscopy [104], and tunnel diode resonator (TDR) technique on Al-coated samples [105]. μ SR measures averaged $\lambda(T, H)$ in the mixed state and from field-dependence of λ , the zero field-limiting value is extracted and should be extrapolated to T=0. In infrared spectroscopy, $\lambda(0)$ is deduced from the measured plasma frequency [104]. In the Al-coating technique for TDR, $\lambda(0)$ is estimated from penetration of rf field through known thickness of uniformly coated Al over the sample surface [105]. While aforementioned techniques deal with bulk properties of a specimen, some local probes with spatial resolution of $\sim \mu m$ have been accomplished, which include scanning SQUID [106] and MFM [107] magnetometry. In these local techniques, $\lambda(T)$ is inferred from the analysis of magnetic interactions between a relevant probe and a magnetic moment induced in a superconductor [108].

Of all the techniques mentioned, TDR offers perhaps the most precise data on the

change of λ with temperature, $\Delta \lambda = \lambda(T) - \lambda(0)$. TDR per se, however, does not provide the absolute value of λ and of $\lambda(0)$, in particular, so that the sample has to be modified by coating with a low- T_c superconductor [105]. Determination of $\lambda(0)$ is critical because the shape of $\rho(T)$ extracted from the data on $\Delta\lambda(T)$ depends sensitively on the value of $\lambda(0)$ adopted, and a wrong $\lambda(0)$ could lead to incorrect conclusions on the superconducting order parameter.

In this chapter we show that the thermodynamic Rutgers relation [109] between the specific heat jump ΔC and the slope of upper critical field dH_{c2}/dT at the critical temperature T_c can be used to check consistency of the chosen value of $\lambda(0)$ provided that reliable data on $\Delta\lambda(T)$ are available over a broad temperature domain. Moreover, we offer a method of estimating $\lambda(0)$ provided that ΔC and dH_{c2}/dT at T_c are known. This idea is checked on Nb and MgB₂ and applied to several unconventional superconductors. In all cases we use $\Delta\lambda(T)$ measured by using the TDR technique and literature data for other two quantities except for YBa₂Cu₃O_{1- δ} where its superfluid density is taken from elsewhere [110]. In all studied cases, the method works well and determined values of $\lambda(0)$ are in agreement with established literature values.

3.1 Thermodynamic Rutgers relation

The specific heat jump at T_c in materials where the critical fluctuations are weak is expressed through the free energy difference $F_n - F_s = H_c^2/8\pi$: [109, 111]

$$\Delta C = T_c \frac{\partial^2}{\partial T^2} \frac{H_c^2}{8\pi} \Big|_{T_c} = \frac{T_c}{4\pi} \left(\frac{\partial H_c}{\partial T} \right)_{T_c}^2$$
(3.1)

Here, C is measured in erg/cm³K and T in K. Within the mean-field Ginzburg-Landau (GL) theory, near T_c , the thermodynamic critical field $H_c = \phi_0/2\sqrt{2}\pi\xi\lambda$ with

$$\xi = \frac{\xi_{GL}}{\sqrt{1-t}}, \qquad \lambda = \frac{\lambda_{GL}}{\sqrt{1-t}}, \qquad t = \frac{T}{T_c}.$$
 (3.2)

Here ξ and λ are the coherence length and the penetration depth, and the constants ξ_{GL} , λ_{GL} are of the same order but not the same as the zero-T values $\xi(0)$ and $\lambda(0)$.

Hence we have:

$$\Delta C = \frac{\phi_0^2}{32\pi^3 \xi_{GL}^2 \lambda_{GL}^2 T_c} \,, \tag{3.3}$$

where ξ_{GL} is related to the slope of $H_{c2}(T)$ at T_c :

$$T_c \frac{\partial H_{c2}}{\partial T}\Big|_{T_c} = \frac{\partial H_{c2}}{\partial t}\Big|_{t=1} = H'_{c2}(1) = -\frac{\phi_0}{2\pi\xi_{GL}^2}.$$
 (3.4)

It is preferable to determine the slope of H_{c2} line from specific heat measurements since resistive determination of this line is significantly affected by vortex lattice instability (irreversibility line). It is common to introduce the dimensionless superfluid density $\rho = \lambda^2(0)/\lambda^2$ with the slope at T_c given by

$$T_c \frac{\partial \rho}{\partial T}\Big|_{T_c} = \frac{\partial \rho}{\partial t}\Big|_{t=1} = \rho'(1) = -\frac{\lambda^2(0)}{\lambda_{GL}^2}.$$
 (3.5)

We then obtain:

$$\Delta C = \frac{\phi_0}{16\pi^2 \lambda^2(0)T_c} (H'_{c2} \rho')_{t=1}$$
(3.6)

where the primes denote derivatives with respect to t.

It should be stressed that being a thermodynamic relation that holds at a 2nd order phase transition, applicability of Rutgers formula is restricted only by possible presence of critical fluctuations. In particular, it can be applied for zero-field phase transition in materials with anisotropic order parameters and Fermi surfaces, multi-band etc, which makes it a valuable tool in studying great majority of new materials.

For anisotropic materials, Eq. (3.1) is, of course, valid since the condensation energy and H_c do not depend on direction. However, already in Eq. (3.3) the field direction should be specified. In the following we discuss situations with \mathbf{H} parallel to the c axis of uniaxial crystals. Hence, H_{c2} , ρ , and $\lambda(0)$ in Eq. (3.6) should have subscripts ab; we omit them for brevity. A general case of anisotropic material with arbitrary field orientation requires separate analysis.

3.2 Theoretical results relevant for the analysis of the superfluid density

3.2.1 Penetration depth in anisotropic materials

It is known [112] that in isotropic materials,

$$\rho'(1) = -\lambda^2(0)/\lambda_{GL}^2 = -2. \tag{3.7}$$

It is easy to reproduce this result for the free electron model of the normal state; it is shown below, however, that this value holds for any Fermi surface provided the order parameter is isotropic.

Here, we are interested in relating $\lambda(0)$ and λ_{GL} , the T independent part of λ near T_c , for anisotropic Fermi surfaces and order parameters. We start with a known relation,

$$(\lambda^2)_{ik}^{-1} = \frac{16\pi^2 e^2 N(0)T}{c^2} \sum_{\omega} \left\langle \frac{\Delta^2 v_i v_k}{\beta^3} \right\rangle , \qquad (3.8)$$

which holds at any temperature for *clean* materials with arbitrary Fermi surface and order parameter anisotropies [113, 102]. Here, N(0) is the density of states at the Fermi level per spin, $\beta^2 = \Delta^2 + \hbar^2 \omega^2$ with $\hbar \omega = \pi T (2n+1)$, $\Delta(\mathbf{k}_F, T) = \Psi(T) \Omega(\mathbf{k}_F)$ is the zero-field order parameter which in general depends on the position \mathbf{k}_F on the Fermi surface, and $\langle ... \rangle$ stand for averaging over the whole Fermi surface. The function $\Omega(\mathbf{k}_F)$ which describes the variation of Δ along the Fermi surface, is normalized: $\langle \Omega^2 \rangle = 1$.

Eq. (3.8) is obtained within the model of factorizable effective coupling $V(\mathbf{k}, \mathbf{k}') = V_0 \Omega(\mathbf{k}) \Omega(\mathbf{k}')$ [114]. The self-consistency equation of the weak coupling theory takes the form:

$$\Psi(\mathbf{r},T) = 2\pi T N(0) V_0 \sum_{\omega > 0}^{\omega_D} \left\langle \Omega(\mathbf{k}) f(\mathbf{k}, \mathbf{r}, \omega) \right\rangle, \tag{3.9}$$

where f is the Eilenberger Green's function which, for the uniform current-free state, reads: $f = \Delta/\beta = \Psi\Omega/\beta$. The order parameter near T_c is now readily obtained:

$$\Psi^2 = \frac{8\pi^2 T_c^2 (1-t)}{7\zeta(3)\langle \Omega^4 \rangle} \,, \tag{3.10}$$

which reduces to the isotropic BCS form for $\Omega = 1$. Substitute this in Eq. (3.8) to obtain near T_c :

$$(\lambda^2)_{ik}^{-1} = \frac{16\pi e^2 N(0) \langle \Omega^2 v_i v_k \rangle}{c^2 \langle \Omega^4 \rangle} (1 - t). \tag{3.11}$$

The constants λ_{GL} for any direction readily follow.

As $T \to 0$, the sum over ω in Eq. (3.8), the so-called Matsubara frequencies, can be replaced with an integral according to $2\pi T \sum_{\omega} \to \int_0^{\infty} d(\hbar \omega)$:

$$(\lambda^2)_{ik}^{-1}(0) = \frac{8\pi e^2 N(0)}{c^2} \left\langle v_i v_k \right\rangle. \tag{3.12}$$

For free electrons, this reduces to the London value $\lambda^2 = mc^2/4\pi e^2 n$ where $n = 2mN(0)v^2/3$ is the electron density.

Hence, we get for the slope of the in-plane superfluid density:

$$\rho_{ab}'(1) = -\frac{\lambda_{ab}^2(0)}{\lambda_{GLab}^2} = -2\frac{\langle \Omega^2 v_a^2 \rangle}{\langle v_a^2 \rangle \langle \Omega^4 \rangle}.$$
 (3.13)

Similarly, one can define $\rho'_c(1)$ for which v_a should be replaced with v_c in Eq. (3.13). In particular, we have:

$$\frac{\rho_c'(1)}{\rho_{ab}'(1)} = \frac{\langle v_a^2 \rangle}{\langle v_c^2 \rangle} \frac{\langle \Omega^2 v_c^2 \rangle}{\langle \Omega^2 v_a^2 \rangle} = \frac{\gamma_\lambda^2(0)}{\gamma_\lambda^2(T_c)}.$$
 (3.14)

E.g., for MgB₂ with $\gamma_{\lambda}(0) \approx 1$, $\gamma_{\lambda}(T_c) \approx 2.6$, we estimate $\rho'_c(1) \approx 0.15 \, \rho'_{ab}(1)$.

It is instructive to note that $\rho'(1)$ reduces to the isotropic value of -2 for any Fermi surface provided the order parameter is constant, $\Omega = 1$.

$3.2.2 \quad MgB_2$

Consider a simple two-band model with the gap anisotropy given by

$$\Omega(\mathbf{k}) = \Omega_{1,2} \,, \quad \mathbf{k} \in F_{1,2} \,, \tag{3.15}$$

where F_1, F_2 are two sheets of the Fermi surface. $\Omega_{1,2}$ are assumed constants, in other words, we model MgB₂ as having two different s-wave gaps. The normalization $\langle \Omega^2 \rangle = 1$ then gives:

$$\Omega_1^2 \nu_1 + \Omega_2^2 \nu_2 = 1, \quad \nu_1 + \nu_2 = 1,$$
 (3.16)

where $\nu_{1,2} = N_{1,2}/N(0)$ are the relative densities of states.

Based on the band structure calculations [115, 116], ν_1 and ν_2 of our model are ≈ 0.56 and 0.44. The ratio $\Delta_2/\Delta_1 = \Omega_2/\Omega_1 \approx 3$. Then, the normalization (3.16) yields $\Omega_1 = 0.47$ and $\Omega_2 = 1.41$.

Further, we use the averages over separate Fermi sheets calculated in Ref. [115]: $\langle v_a^2 \rangle_1 = 33.2, \, \langle v_a^2 \rangle_2 = 23 \, \mathrm{cm}^2/\mathrm{s}^2$. With this input, we estimate

$$\rho_{ab}'(1) = -0.92. (3.17)$$

It should be noted that this number is sensitive to a number of input parameters. The procedure described above, see Fig. 5.10 gives $\rho'_{ab}(1) \approx -0.91$.

Since only even powers of Ω enter Eq. (3.13), the same analysis of the slope $\rho'(1)$ can, in fact, be exercised for materials modeled by two bands with the $\pm s$ symmetry of the order parameter, for which Ω 's have opposite signs. If the bands relative densities of state $\nu_{1,2}$ and the averages $\langle v_a^2 \rangle_{1,2}$ are comparable to each other and similar to those of MgB₂, we expect a similar $|\rho'(1)| \approx 1$ for clean crystals.

3.2.3 d-wave

It can be shown that $\Omega = \sqrt{2}\cos 2\phi$ for closed Fermi surfaces as rotational ellipsoids (in particular, spheres) or open ones as rotational hyperboloids (in particular, cylinders) [117]. Using the relation for anisotropic materials with a spherical Fermi surface:

$$\rho_{ab}'(1) = -\frac{\lambda_{ab}^2(0)}{\lambda_{GL,ab}^2} = -2\frac{\langle \Omega^2 v_a^2 \rangle}{\langle v_a^2 \rangle \langle \Omega^4 \rangle} = -4/3. \tag{3.18}$$

3.2.4 Scattering

In the limit of a strong non-magnetic scattering for an arbitrary Fermi surface but a constant s-wave order parameter we have, see, e.g, Ref. [102]:

$$(\lambda^2)_{ik}^{-1} = \frac{8\pi^2 e^2 N(0) \langle v_i v_k \rangle \tau}{c^2 \hbar} \Delta \tanh \frac{\Delta}{2T}.$$
 (3.19)

Here τ is the average scattering time. It is worth noting that the dirty limit does not make much sense for anisotropic gaps because T_c is suppressed even by non-magnetic scattering in the limit $\tau \to 0$. At T = 0, we have

$$(\lambda^2)_{ik}^{-1}(0) = \frac{8\pi^2 e^2 N(0) \langle v_i v_k \rangle \tau}{c^2 \hbar} \, \Delta(0) \,, \tag{3.20}$$

whereas near T_c

$$(\lambda^2)_{ik}^{-1} = \frac{8\pi^2 e^2 N(0) \langle v_i v_k \rangle \tau}{c^2 \hbar} \frac{\Delta^2}{2T_c}, \tag{3.21}$$

Since for non-magnetic scattering, T_c and $\Delta(T)$ are the same as in the clean case, in particular $\Delta = 8\pi^2 T_c^2 (1-t)/7\zeta(3)$, we obtain

$$\rho'(1) = -\frac{4\pi^2 T_c}{\Delta(0)} = -\frac{4\pi e^{\gamma}}{7\zeta(3)} = -2.66.$$
(3.22)

We thus conclude that scattering causes the slope $\rho'(1)$ to increase.

Evaluation of scattering effects on the slope ρ' near T_c for anisotropic gaps and Fermi surfaces are more involved because both T_c and Δ are affected even by non-magnetic scattering. The case of a strong pair-breaking is an exception: $\lambda^{-2} = \lambda_0^{-2}(1-t^2)$ that immediately gives $\rho'(1) = -2$.

3.3 Determination of $\lambda(0)$

The full superfluid density needed for the analysis of the experimental data and comparison with theoretical calculations depends on the choice of $\lambda(0)$:

$$\rho(t) = \frac{\lambda^2(0)}{[\lambda(0) + \Delta\lambda(t)]^2}.$$
(3.23)

Figure 3.1 shows an example of this dependence of $\rho(t)$ on $\lambda(0)$ for Nb. In the upper panel, experimental $\Delta\lambda(T)$ is shown. In the lower panel, symbols represent $\rho(t)$ calculated from measured $\Delta\lambda(t)$ with $\lambda(0)$ chosen as 15, 25 and 35 nm. Clearly, the calculated $\rho(t)$ is sensitive to the choice of $\lambda(0)$. The straight solid lines have the slope $\rho'(1)$ calculated by using Eq. (3.6) for each $\lambda(0)$. We used $\Delta C = 137.2$ mJ/mol-K

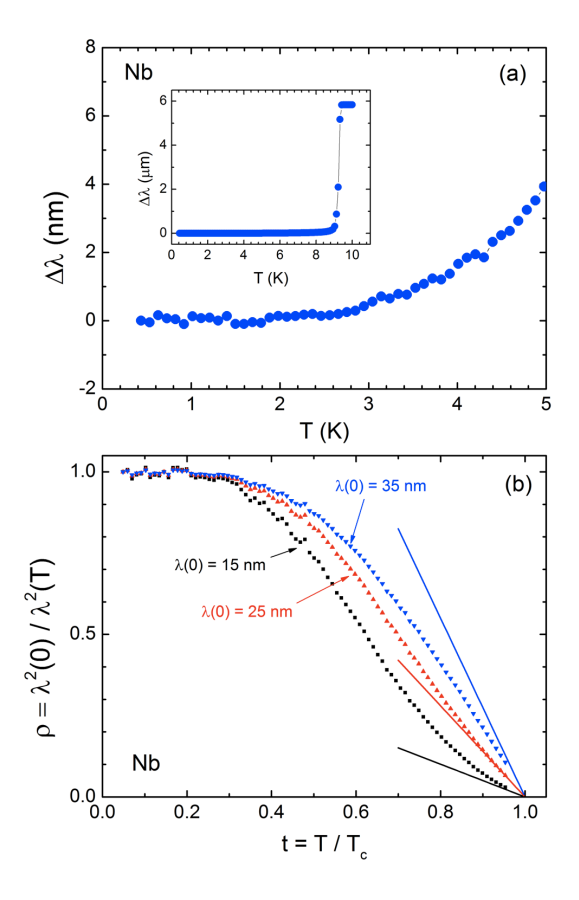


Figure 3.1 (a) London penetration depth in Nb measured by using a TDR technique. (b) Superfluid density $\rho(t)$ calculated from Eq. (3.23) using $\Delta\lambda(T)$ shown in (a) and assuming $\lambda(0) = 15$, 25, and 35 nm. Straight lines have the slope ρ' estimated from Eq. (3.6) for each $\lambda(0)$.

= 126450 erg/cm³K (Ref. [118]) since in the formulas used here the specific heat is per unit volume. To convert ΔC which is commonly reported in mJ/mol-K into erg/cm³K, one needs to calculate the mass density which requires crystallographic information. For niobium we use parameters found in Ref. [119]. Crystal structure of elemental niobium belongs to the space group Im-3m (no. 229) with lattice parameters a = b = c = 0.3303 nm, and corresponding volume is V = 0.036 nm³. There are two molecular units per the volume (Z = 2). Using these values the converted $\Delta C = 137.2$ mJ/mol-K

¹The lattice parameters used for this analysis are values determined at room temperature. Using representative values for thermal contraction at T_c by 2.5% and 5%, the unit-conversion for ΔC results in smaller values by 2.5% and 5%, respectively. This discrepancy will be taken into account for estimate of $\lambda(0)$ by using experimental uncertainties of $\pm 5\%$ in determining ΔC .

(Ref. [118]) = 126450 erg/cm³K. Using $H'_{c2}|_{T_c} = 440$ Oe/K (Ref. [120]), we obtain $-\rho'(1) = 0.49$, 1.4, and 2.7 for 15, 25, and 35 nm, respectively. While the choice of $\lambda(0) = 25$ nm shows reasonable agreement, for the choices of 15 nm and 35 nm the slopes calculated using the data and Eq. (3.23) determined by Eq. (3.6) under- and overestimates, respectively. Note that with $\lambda(0) = 15$ nm, the temperature dependence of ρ is pronouncedly concave near t = 1, and also $-\rho'(1)$ is smaller than one. The idea of our method is to utilize the Rutgers relation (3.6) and choose such a $\lambda(0)$ that would not contradict the thermodynamics near T_c .

To this end we rewrite Eq. (3.6) in the form:

$$\frac{\rho'(1)}{\lambda^2(0)} = \frac{16\pi^2 T_c \Delta C}{\phi_0 H'_{c2}(1)}.$$
(3.24)

The right-hand side here is determined from independent measurements of ΔC and H_{c2} . Thus, by taking a few test values of $\lambda(0)$, calculating $\rho(t)$ and its slope at t=1, we can decide which $\lambda(0)$ and $\rho(t,\lambda(0))$ obey the Rutgers relation.

We first apply this method to two well-studied superconductors - conventional Nb and two-band MgB₂. For Nb, we obtain $|\rho'|/\lambda^2(0) \approx 2240 \ \mu\text{m}^{-2}$ using the same thermodynamic quantities as for Fig. 3.1 [118, 120]. We now take a set of values for $\lambda(0)$ shown in top left panel of Fig. 3.2 and plot $|\rho'|/\lambda^2(0)$ vs $\lambda(0)$. The value of $\lambda(0) = 28 \pm 2 \,\text{nm}$ satisfying the Rutgers relation is obtained from the intersection of the calculated curve with the value expected from Eq. (3.24) (shown by a gray band that takes into account experimental uncertainties in determining ΔC and H'_{c2}). It is consistent with the literature values varying between 26 and 39 nm [118, 121]. The final calculated superfluid density with the choice of $\lambda(0) = 30 \,\text{nm}$ is shown in Fig. 3.2(b). The solid line is determined with calculated slope $|\rho'(1)| = 2$ which is what is predicted for isotropic s-wave superconductors.

In addition to aforementioned uncertainties, determination of the experimental $|\rho'(1)|$ is not trivial even if the quality of measurement is excellent since $\rho(t)$ near t=1 is often significantly curved due to several experimental artifacts, most importantly due to the

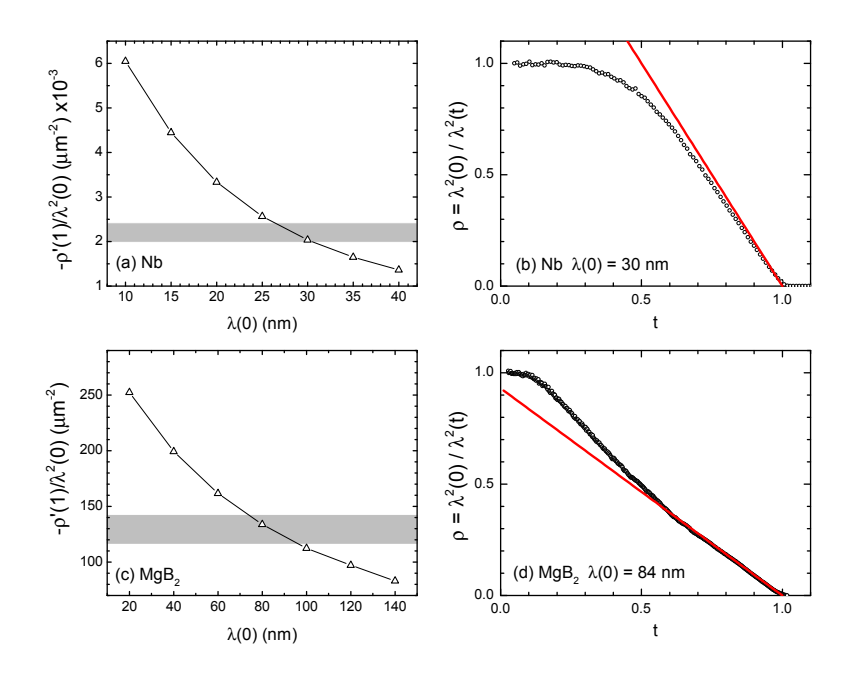


Figure 3.2 Top row - Nb, Bottom row - MgB₂. Left column: variation of $|\rho'|/\lambda^2(0)$ as a function of $\lambda(0)$ for Nb and MgB₂. Shaded horizontal bands are the estimated values of the right-hand side of Eq. (3.24) with literature values of ΔC and $H'_{c2}(1)$ including experimental uncertainties. Right column: superfluid density for the best value of $\lambda(0)$ that satisfies the Rutgers relation, Eq. (3.24).

influence of the normal skin effect near T_c , which is more pronounced for higher frequency measurements on highly conducting materials. TDR technique uses typically ~ 10 MHz, so this effect is weak in most of the materials concerned. By surveying many different superconductors, we have found that the data in the regime between t = 0.8 and 0.95 works well for determination of $\rho'(1)$. The experimental $|\rho'(1)|$ in this work is determined from the best linear fit of $\rho(t)$ data in this range.

The same procedure can be employed for a well known multi gap superconductor MgB₂ (shown in the bottom row of Fig. 3.2), where $|\rho'|/\lambda^2(0)$ is estimated to be 130 ± 12 μ m⁻² by using $\Delta C = 133$ mJ/mol-K (Ref. [17]), $|H'_{c2}(1)| = 0.45$ T/K (Ref. [16]) within $\pm 5\%$ error. The determined $\lambda(0) = 84 \pm 10$ nm is in good agreement with 100 nm estimated by μ SR technique [122, 123]. For $\lambda(0) = 84$ nm, the calculated slope

 $|\rho'(1)| = 0.91$ agrees with the expected theoretical value of 0.92.

The method described also has been used for $SrPd_2Ge_2$ for which $\lambda(0)$ was not clear. By using the determined $\lambda(0)$ we have shown that $SrPd_2Ge_2$ is a single-gap s-wave superconductor [124].

3.4 Application of Rutgers formula to unconventional superconductors

Here we examine a few superconductors for which the necessary experimental quantities have been reported in the literature. Where possible, we use $H_{c2}(T)$ determined from the specific heat jump, because resistive and magnetic measurements may determine the irreversibility field, which may differ substantially from the thermodynamic H_{c2} [138].

We have selected LiFeAs, FeTe_{0.58}Se_{0.42}, YBa₂Cu₃O_{1- δ} and MgCNi₃ representing stoichiometric pnictide, charchogenide, d-wave high- T_c cuprate and close to magnetic instability s-wave superconductors, respectively. The selected compounds have been extensively studied, and ΔC , dH_{c2}/dT , and $\lambda(0)$ have been measured by various techniques by different groups. Superfluid density was calculated from the penetration depth measured by using a TDR technique at Ames Laboratory, except for YBCO for which anisotropic superfluid density was determined by microwave cavity perturbation technique [110]. Thermodynamic parameters are discussed in the number of papers [31, 30, 32]. In-depth discussion of the specific heat is given in Refs. [32, 63]. Table 3.1 summarizes parameters used in the calculations.

Figure 3.3 shows experimental superfluid density in LiFeAs, FeTe_{0.58}Se_{0.42}, YBa₂Cu₃O_{1- δ} and MgCNi₃ with $\lambda(0) = 500$, 200, 120, and 232 nm, respectively. The agreement between ρ'_{Rut} calculated with the Rutgers relation and ρ'_{exp} extracted from the data on $\Delta\lambda(t)$, given possible uncertainties in the input experimental parameters, is rather remarkable.

realtion. V_c is the volume of the unit cell at room temperature. ΔC is the specific heat jump at T_c in mJ/mol-K. dH_{c2}/dT is slope of H_{c2} at T_c . Physical parameters used for analysis of superfluid density with Rutgers $\rho'_{Rut} = (d\rho/dt)_{Rut}$ is the calculated slope using Eq. (3.6) where $t = T/T_c$. ρ'_{exp} is an experimental slope with given $\lambda(0)$. Table 3.1

compound	V_c (Å ³)	T_c (K)	$\Delta C/T_c \; (\mathrm{mJ/mol-K}^2)$	$ dH_{c2}/dT _{T_c}$ (T/K) $\lambda(0)$ (nm)	$\lambda(0) \text{ (nm)}$	$- ho_{Rut}'$	$- ho_{exp}'$
Nb	35.937 [119]	9.3 [118]	14.8 [118]	0.044 [120]	30^a	2.0	1.8
MgB_2	29.064 [14]	39[17]	3.4[17]	0.45 [16]	84^{b}	0.91	0.83
LiFeAs	90.252 [125]	15.4 [126]	20 [126]	3.46[127]	200[128]	1.2	1.1
$\mathrm{FeTe}_{0.58}\mathrm{Se}_{0.42}$	87.084 [31]	14 [129]	20[129]	13[130]	500^{c}	1.4	1.5
$YBa_2Cu_3O_{1-\delta}$		23[63]	61[134]	$[1.9\ [135]]$	120 [105]	3.0	2.15 - 4.98 [110]
$ m MgCNi_3$	$[54.496\ [136]$	7[136]	129[136]	2.6[133]	232[137]	1.8	2.0

 a determined in this work. b determined in this work.

 $^c{\rm an}$ average value over 430-560 nm (Ref. [130, 131, 132])

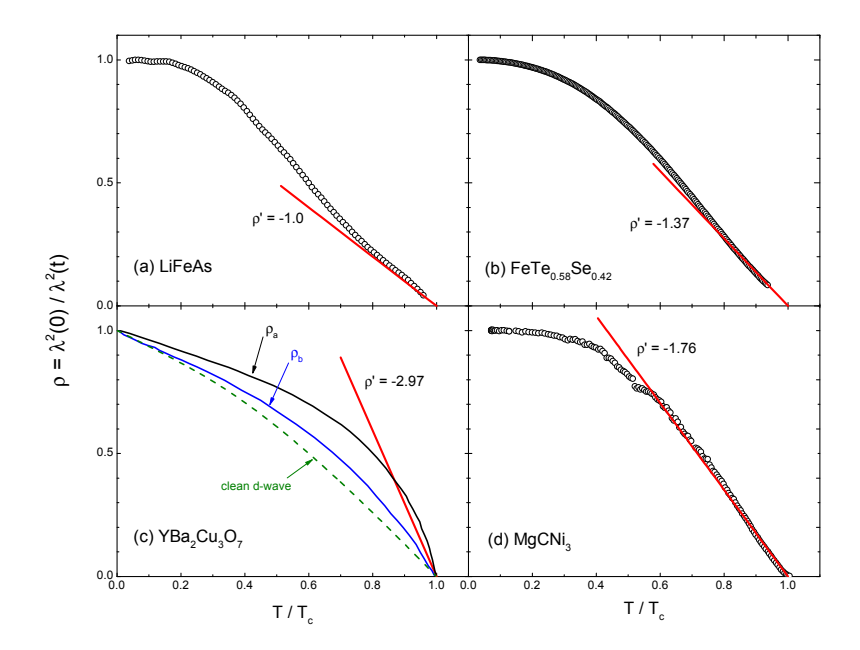


Figure 3.3 Experimental superfluid density $\rho = \lambda^2(0)/\lambda^2(T)$ in LiFeAs, FeTe_{0.58}Se_{0.42}, YBa₂Cu₃O_{1- δ}, and MgCNi₃ with $\lambda(0) = 500$, 200, 120, and 232 nm, respectively. The straight lines in each panel were estimated with the Rutgers formula. Parameters used for the calculation are summarized in Table 3.1.

In conclusion, we have shown that the thermodynamic relation Rutgers formula can be used for the analysis of superfluid density. Using this relation we have developed a method to estimate $\lambda(0)$. This method successfully estimates $\lambda(0)$ of Nb and MgB₂. This relation was applied to several superconductors of different band structure, gap anisotropy, and pairing symmetry, showing a good agreement with the theory.

CHAPTER 4. DOPING DEPENDENCE OF LONDON PENETRATION DEPTH AND SUPERFLUID DENSITY IN IRON-BASED SUPERCONDUCTORS

Since the discovery of superconductivity in LaFeAsO_{1-x}F_x [25], the symmetry of the superconducting gap in the Fe-based superconductors has been heavily studied. Up to date, however, it is not in consensus. Early results seemed consistent with the s_{\pm} -wave symmetry [57, 61, 139], but following penetration depth measurements are consistent with nodal superconducting gap in LaFeAsP [91] and over-doped BaNi122 [140]. Thermal conductivity measurements on a full series of superconducting Ba(Fe,Co)₂As₂ revealed doping dependent gap structure consistent with full-gap at optimal doping and strong anisotropic or nodal gap at the both edges of the superconducting dome [78]. A key question would be whether this doping dependence is universal for Fe-based superconductors.

In this chapter, we discuss temperature variation of the London penetration depth in various families of FeSC of different chemical substitution levels. First, we will look into doping-dependent London penetration depth in $Fe_{1+y}Te_{1-x}Se_x$ in which superconductivity arises when the double stripe AFM and spin-glass magnetism is suppressed (see Fig.1.6(b)). Second, we discuss the London penetration depth measured in $Ca_{10}(Pt_3As_8)((Fe_{1-x}Pt_x)_2As_2)_5$ (10-3-8). In this compound, the relatively large electronic anisotropy is caused due to the relatively large separation between conducting FeAs-layers. The separation in the 10-3-8 compound is \sim 11 Å which is larger than, for

example, ~ 9 Å and ~ 7 Å in La1111 and Ba122 compounds, respectively. Superconducting state is also separated from magnetism in T-x phase diagram. Magnetic structure in this compound is not fully known up to date. A NMR study suggests a stripe type, but it is different than the magnetic structure in other FeSC [141]. Next, we move on to underdoped $\mathrm{Ba}_{1-x}\mathrm{K}_x\mathrm{Fe}_2\mathrm{As}_2$ systems in which superconductivity coexists with a stripe-type AFM. Finally, we present experimental results on two extreme cases, first of which is the case of full substitution of Fe with Pd in AFe₂As₂ (A=Ca, Sr), and the second case is $\mathrm{SrPd}_2\mathrm{Ge}_2$.

4.1
$$\mathbf{Fe}_{1+y}\mathbf{Te}_{1-x}\mathbf{Se}_x$$

The majority of iron-based superconductors are prictides. The only exceptions, to date, are $K_x Fe_{2-y} Se_2$ and $Fe_{1+y} Te_{1-x} Se_x$. The former exhibits up to $T_c = 33$ K, making it interesting to study. However, presence of localized magnetic moments exhibiting the Curie-like behavior $(\chi \sim T^{-1})$ [142] makes analysis of London penetration depth difficult unless the magnetic contribution is fully known [88]. The latter $Fe_{1+y}Te_{1-x}Se_x$ becomes superconducting with the excess Fe occupying interstitial sites of the (Te,Se) (or chalcogenide layer) layers [143]. In these materials, generally referred to as "11" compounds, Fe forms square planar sheets whereas Se ions form distorted tetrahedra surrounding the Fe ions, which is similar to the structure of the Fe-prictides. The electronic structure is also similar to prictides. For "11" system it has been suggested both theoretically |144| and experimentally |145| that superconductivity could be magnetically mediated. Furthermore, the series of iron-chalcogenides from FeS through FeTe was theoretically explored within the spin-fluctuation picture, concluding that doped FeTe could exhibit the strongest superconductivity [144]. The systems over which the doping is most controlled are $\text{FeTe}_{1-x}\text{Se}_x$ [146] and $\text{FeTe}_{1-x}\text{S}_x$ [147]. So far the highest $T_c \approx 15 \text{ K}$ is reported for the Fe(Te,Se) system [146, 50]. The connection between superconductivity and magnetism in the "11" system has been demonstrated by the observation of the antiferromagnetic order in Fe_{1+y} Te [143] and a spin resonance in Fe_{1+y} (Te_{0.6}Se_{0.4}) [148].

The "11" system exhibits many interesting phenomena. The transition temperature can be enhanced up to 37 K by applying modest pressures [149], which is comparable to the T_c of iron-arsenide superconductors [44]. The connection between T_c and the pressure has been suggested to come from the enhancement of spin fluctuations [150] and from the modulation of electronic properties due to evolution of the inter-layer Se-Fe-Se separations [149]. Several experimental works explore pairing mechanism of "11" compounds. The absence of a coherence peak in NMR measurements on polycrystalline FeSe suggests unconventional superconductivity [151], while the power-law temperature dependence of the spin-relaxation rate, $1/T_1 \sim T^3$, could be reconciled with both a nodal gap or a fully-gapped s_{\pm} state. Muon spin rotation study of the penetration depth in FeSe_x was consistent with either anisotropic s-wave or a two-gap extended s-wave pairing [152]. Thermal conductivity measurements concluded multigap nodeless superconductivity in polycrystalline FeSe_x [153].

In this section, we present an experimental study of the London penetration depth, $\lambda(T)$, in single crystals of Fe_{1.03}(Te_{0.63}Se_{0.37}) and Fe(Te_{0.58}Se_{0.42}) with $T_c=12.8$ and 14.8 K, respectively. The former is slightly underdoped compounds, and spin glass behavior was observed. The latter compound is nominally optimally doped. In both samples, no evidence for paramagnetic impurity down to $\sim 0.04 \, T_c$ as seen in K_xFe_{2-y}Se₂. We found that at low temperatures $\Delta\lambda(T) \propto T^n$ with $n \approx 2.1$ and 2.3 for Fe_{1.03}(Te_{0.63}Se_{0.37}) and Fe(Te_{0.58}Se_{0.42}), respectively. The absolute value of $\lambda(0) \approx 560$ nm was determined in Fe_{1.03}(Te_{0.63}Se_{0.37}) by measuring the total $\lambda(T)$ of the sample coated with a thin Al film [105]. The in-plane superfluid density $\rho_s(T) = \lambda^2(0)/\lambda^2(T)$ was analyzed in the framework of a self-consistent two-gap γ -model [154].

Single crystals of $Fe_{1+y}Te_{1-x}Se_x$ were prepared using a solid-state reaction method [50]. Mixed powders of the $Fe(Te_{0.6}Se_{0.4})$ compositions were sealed in evacuated quartz

tubes. The sealed ampoule was slowly heated up to 930 °C and slowly cooled down to 400 °C at a rate of 3 °C/hr before the furnace was shut down. Single crystals with centimeter dimensions can easily be obtained with this method and are shown to be the pure α -phase with the P4/nmm space group by x-ray diffraction [50]. The actual concentrations were analyzed using an energy dispersive x-ray spectrometer (EDXS). The measured composition for the samples discussed in this section is Fe_{1.03}(Te_{0.63}Se_{0.37}). More detail about sample growth and characterization can be found in Ref. [50].

$4.1.1 \quad \text{Fe}_{1.03}(\text{Te}_{0.63}\text{Se}_{0.37})$

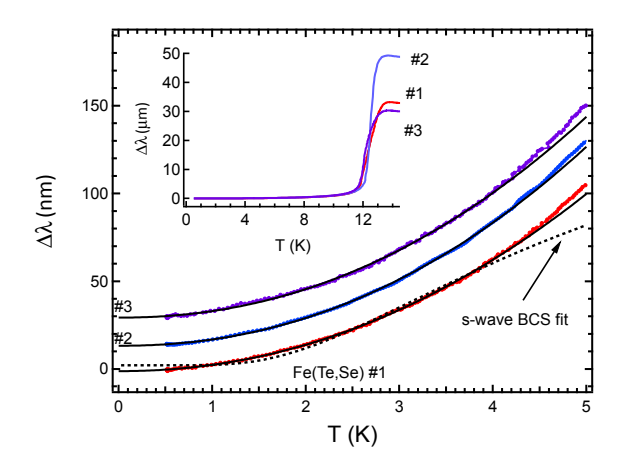


Figure 4.1 Main panel: Variation of the London penetration depth, $\Delta\lambda(T)$ for three Fe_{1.03}(Te_{0.63}Se_{0.37}) samples in the low temperature range shown along with the fitting curves assuming power-low or s-wave BCS behavior. The curves for #2 and #3 are shifted vertically for clarity. Inset: $\Delta\lambda(T)$ in full temperature range.

The inset in Fig. 4.1 shows the full-temperature range penetration depth for three $\text{Fe}_{1.03}(\text{Te}_{0.63}\text{Se}_{0.37})$ superconductors. All three samples show a relatively sharp superconducting transition reflecting the good quality of single crystals. The "maximum slope", T_c^{slope} , determined by taking the maximum of the derivative $d\Delta\lambda(T)/dT$ gives $T_c^{\text{slope}} \approx 12.0$ K. As for the onset values, $T_c^{\text{onset}} \approx 13$ K. The low-temperature variation of $\lambda(T)$ with temperatures down to $0.04\,T_c$ is examined in the main panel of

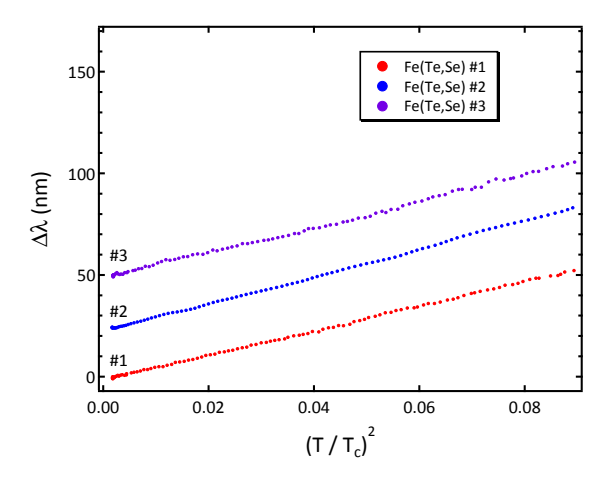


Figure 4.2 $\Delta\lambda$ plotted vs. $(T/T_c)^2$ for three Fe_{1.03}(Te_{0.63}Se_{0.37}) crystals in the temperature range up to $T_c/3$. The curves for #2 and #3 are shifted vertically for clarity.

Fig. 4.1. Such a low base-temperature provide wide temperature range to test various gap structures. The dashed line represents the best fit to a standard s-wave BCS function, $\Delta\lambda(T) = \lambda(0)\sqrt{\pi\Delta_0/2T}\exp(-\Delta_0/T)$, with $\lambda(0)$ and Δ_0 being free fitting parameters. The experimental data do not show any indication of saturation down to the lowest temperature (500 mK) and the fit is not adequate. Also obtained from the fit is $\Delta_0 = 0.5T_c$, which is impossible in a single-gap scenario, hence ruling out conventional s-wave BCS superconductivity. We will come back to a multi-gap s-wave fitting later in this section. On the other hand, fitting with the power-law, $\Delta\lambda(T) \propto AT^n$, $n = 2.10 \pm 0.01$, produces excellent agreement with the data.

In order to examine how close the overall power-law variation is to quadratic, we plot $\Delta\lambda$ versus $(T/T_c)^2$ in Fig. 4.2. All samples follow the $\Delta\lambda(T) \propto T^2$ behavior rather well. To probe how robust the power n is, we performed a data fit over a floating temperature range, from $T = T_{min}$ to T_{up} , using a functional form of $\Delta\lambda(T) = a_0 + AT^n$. The difference between the a_0 term determined from an extrapolation from the T^2 plot in Fig. 4.2 and the power-law fit turned out to be negligible, 1.5±0.5 nm, and had no significant effect on the fit. The dependence of the other fitting parameters, n and A, on

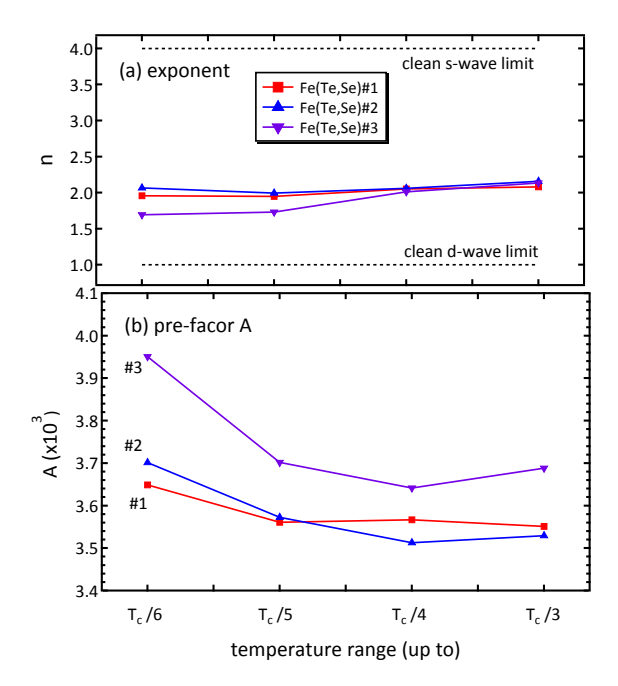


Figure 4.3 Exponent n and pre-factor A obtained by fitting to $\Delta \lambda(T) \propto AT^n$ for various upper temperature limits shown on the x-axis. The exponents in the upper panel were obtained with n and A both being free parameters. In the lower panel, A was acquired with a fixed n=2.1.

 $T_{\rm up}$ (selected in the range from $T_c/6$ to $T_c/3$) is summarized in Fig. 4.3. The upper panel of Fig. 4.3 shows the exponent n, which does not depend much on the selection of the upper limit of the fitting range. The pre-factor A obtained from the fit does not depend much on the fitting range either.

TDR technique offers precision measurement of $\Delta\lambda(T)$ in a superconductor, but the absolute value of $\lambda(0)$ cannot be determined directly. One of ways to determine with measuring a superconductor coated with Al.

To calculate the superfluid density, we need to know the absolute value of the penetration depth, $\lambda(0)$. We used the technique described in Ref. [105]. A thin aluminum layer was deposited using magnetron sputtering conducted in an argon atmosphere. The Al layer thickness, $t=100\pm10$ nm, was determined by using an Inficon XTC 2 with a 6 MHz gold quartz crystal and later directly measured by using scanning electron microscopy on the edge of a broken sample. By measuring the frequency shift from $T\ll T_c^{\rm Al}$

to $T > T_c^{\rm Al}$ and converting it into the effective penetration depth of the coated sample, $\lambda_{\rm eff}$, one can extract the full penetration depth of the material under study from

$$\lambda_{\text{eff}} = \lambda_{\text{Al}} \frac{\lambda + \lambda_{\text{Al}} \tanh(t/\lambda_{\text{Al}})}{\lambda_{\text{Al}} + \lambda \tanh(t/\lambda_{\text{Al}})}$$
(4.1)

where λ is the unknown penetration depth to be determined. Figure 4.4 shows the measured $\lambda_{\rm eff}(T)$ that is compared to the data without Al coating. In the inset, $\Delta\lambda(T)$ in Al at lowest temperatures is shown. Ideally, measurements with lower temperature are needed to determine penetration depth of Al. However, temperature variation of penetration depth in Al which is a typical weak-coupling superconductor is already well-known, so the measured penetration depth is extended to T=0 by using a weak-coupling BCS function with $\Delta(0)=1.764T_c$. The negative offset of 0.05 μ m accounts for the thickness of the Al layer and $\lambda_{Al}(T\ll T_c^{\rm Al})$. According to Eq. (4.1), data plotted this way give the actual $\lambda(T)$ and its extrapolation to T=0 gives an estimate of $\lambda(0)\approx 560\pm 20$ nm for the penetration depth of Fe(Te,Se), which is consistent with a value determined by the Rutgers relation (see Chap. 3) and a μ SR measurement [131]. More details on the Al-coating method can be found in Ref. [105, 155].

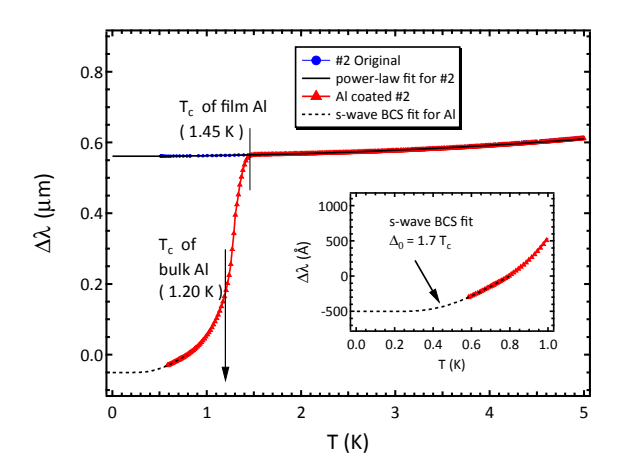


Figure 4.4 (Color online) Effective penetration depth in single crystal Fe(Te,Se) before (blue circles) and after (red triangles) coating with an Al layer. The curve is shifted up according to Eq. (4.1) and the data are extrapolated to T=0 using a T^2 fit resulting in $\lambda(0) \approx 560 \pm 20$ nm.

The superfluid density, $\rho_s(T) = \lambda^2(0)/\lambda^2(T)$, shown in Fig. 4.5, exhibits a noticeable positive curvature at elevated temperatures, similar to MgB₂ [18]. This suggests a multigap superconductivity, which we analyze in the framework of the self-consistent γ -model [154]. According to our $\Delta\lambda(T)$ measurement, multi-gap s-wave model should not work at the lowest temperatures, but it still provides a reasonable description at intermediated temperature regime. We note that our T_c criteria is effectively 10 % of transition and no data above T_c was used for our analysis in order to exclude any extrinsic effects. Fitting in the temperature range from $0.45T_c$ to T_c , shown by a solid (red) line in Fig. 4.5, produces a good agreement with the data. To limit the number of the fitting parameters, the partial densities of states were chosen to be equal in the two bands, $n_1 = 0.5$, and the first intra-band coupling parameter, $\lambda_1 = 0.5$, was chosen to produce a correct $T_c \approx 12$ K assuming a Debye temperature of 230 K found in a similar compound Fe(Te,S) [156]. The variation of λ_1 does not affect the fitting quality or relative ratios of the fitting parameters. The parameters obtained in the fit are: $\lambda_2 = 0.347$, $\lambda_{12} = 0.096$ and $\gamma = 0$. This result means that $\rho_s(T)$ at temperatures of the order of T_c is fully described by only one component, determined by the band with a smaller gap. The existence of the larger gap and small interband coupling, λ_{12} , are needed, however, to maintain a high T_c . The fit over the entire temperature range reveals a clear deviation from this clean exponential model at low temperatures. The new fitting parameters of $\lambda_2 = 0.281$, $\lambda_{12} = 0.117$ and $\gamma = 0.157$ are close to the previous set, albeit with small, but finite γ indicating 16 % contribution of the larger gap to the total superfluid density. The temperature dependent gaps obtained self-consistently in the fitting are shown in the inset to Fig. 4.5. While the fitted positive curvature and reasonable coupling parameters indicate a multi-gap nature of superconductivity in "11" iron-chalcogenide superconductors, the failure at low temperatures and apparently non-exponential behavior requires extension to the anisotropic gap and inclusion effects of (possibly strong) pairbreaking [157].

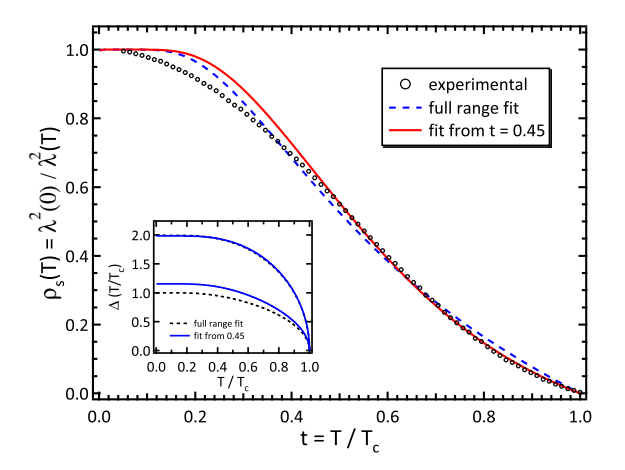


Figure 4.5 Superfluid density $\rho_s(T/T_c)$ for Fe(Te,Se)#2 calculated with experimental $\Delta\lambda(T)$ and $\lambda(0) = 560$ nm. The solid (red) line is a fit the two-gap γ -model from $0.45T_c$ to T_c . The dashed (blue) line is the fit over the full temperature range. Inset: temperature dependent superconducting gaps calculated self-consistently during the fitting.

4.1.2 $Fe(Te_{0.58}Se_{0.42})$

The T-quadratic behavior of London penetration depth in Fe_{1.03}(Te_{0.63}Se_{0.37}) is somewhat ambiguous for any conclusions about the superconducting gap symmetry in the 11 system. Here we compare with optimally doped Fe(Te_{0.58}Se_{0.42}) to get further insight about the gap symmetry in the 11 system.

The inset of Figure 4.6 presents $\chi_{ac}(T)$ in full superconducting temperature range which shows a sharp phase transition at 14.8 K. One of Fe_{1.03}(Te_{0.63}Se_{0.37}) samples with lower T_c discussed in the previous section is shown for comparison. In the main panel, the low temperature behavior of $\Delta\lambda$ up to $0.3T_c$ is shown with a solid curve determined by a power-law fitting. Data can be best fitted to a power-law function, $\Delta\lambda(T) = AT^n$, with $(n = 2.43 \pm 0.01, A = 529 \pm 5 \text{ nm/K}^{2.43})$ and $(n = 2.10 \pm 0.01, A = 807 \pm 13 \text{ nm/K}^{2.1})$ for Fe(Te_{0.58}Se_{0.42}) and Fe_{1.03}(Te_{0.63}Se_{0.37}), respectively.

For quantitative analysis of the low temperature behavior, a power-law fit, $\Delta\lambda(T)$ = AT^n was performed with four different upper temperature limits for the fit: $0.15T_c$, $0.20T_c$, $0.25T_c$ and $0.3T_c$. The results of the fitting are summarized in Fig. 4.7(b). Clearly,

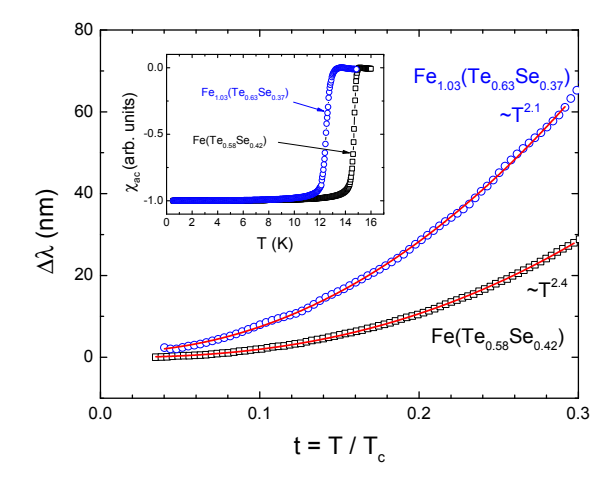


Figure 4.6 Inset: normalized χ_{ac} vs T in Fe_{1+y}Te_{1-x}Se_x. Main panel: $\Delta\lambda(t)$ in Fe(Te_{0.58}Se_{0.42}) and Fe_{1.03}(Te_{0.63}Se_{0.37}) in open squares and circles, respectively, where $t = T/T_c$. Red solid line represent best power-law fitting functions obtained by fitting data up to $0.3T_c$. Best fitting can be achieve with n = 2.4 and 2.1 for Fe(Te_{0.58}Se_{0.42}) and Fe_{1.03}(Te_{0.63}Se_{0.37}), respectively.

the fit coefficients remain fairly constant with small deviations at the lowest and the highest limits. From the best fits with T/T_c upper limit, the average exponent $n=2.36\pm0.07$ is quite comparable to the previous reports of n=2.1 [132], 2.2 [158] and 2.0 [130]. The exponent n=2.36 can be explained by the nodeless two-gap pairing symmetry with strong pair breaking effect. The behavior of the pre-factor A, which is determined to be $A_{avg}=0.8\pm0.2$ nm/K^{2.36}, also show very weak compare to what was found in Fe_{1.03}(Te_{0.63}Se_{0.37}).

The superfluid density $\rho_s = \lambda^2(0)/\lambda^2(T)$ in Fe(Te_{0.58}Se_{0.42}) is shown in Fig. 4.8. Here we use $\lambda(0) = 560$ nm determined in Fe_{1.03}(Te_{0.63}Se_{0.37}) [132]. The fitting was done with a self-consistent clean two-gap γ -model, where two gaps are calculated self-consistently at each temperature and at each iteration [154]. Since temperature diminishes the relative contribution of impurity scattering, we expect to have better agreement at the higher temperatures and deviations from exponential behavior at the low temperatures. Yet, we believe that the extracted coupling parameters are meaningful. The total superfluid density is given by $\rho_s = \gamma \rho_1 + (1 - \gamma)\rho_2$. The partial densities of states are chosen to

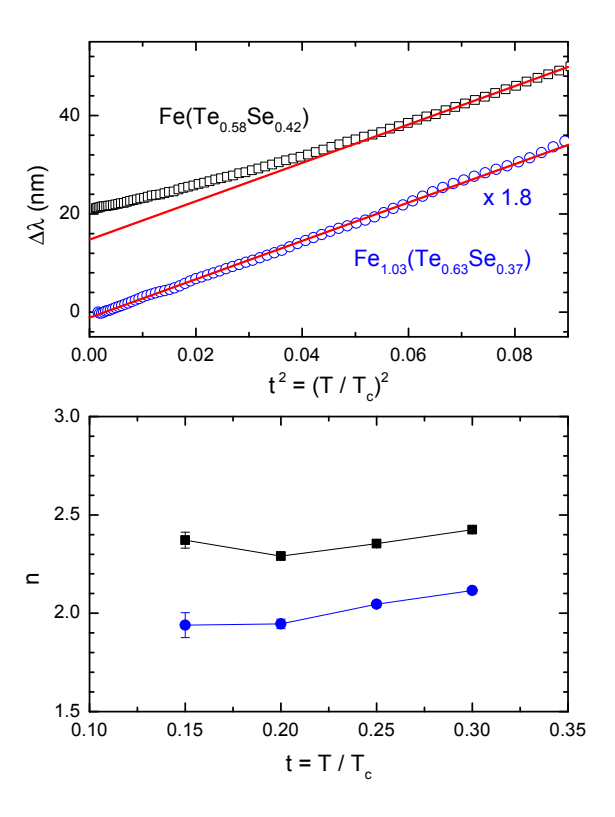


Figure 4.7 (a) $\Delta \lambda$ vs $t^2 = (T/T_c)^2$ in Fe_{1+y}Te_{1-x}Se_x. Red linear lines are guide for eyes. (b) n vs t obtained from a power-law fitting up to various upper temperature limits (t).

be equal on the two bands, $n_1 = n_2 = 0.5$ and Debye temperature of 230 K [156] was used to calculate the experimentally observed $T_c = 14.8$ K, which fixes the coupling constants (we used λ_{11}). Figure 4.8 demonstrates good agreement between experimental ρ_s (symbols) and fitting (black solid line). The parameters acquired from the fit are: $\lambda_{11} = 0.66$, $\lambda_{22} = 0.44$, $\lambda_{12} = 0.07$, $\lambda_{\text{eff}} = 0.34$, $\gamma = 0.75$ and $T_c = 14.95$ K. This result indicates that 75 % contribution of superfluid density comes from the band with ρ_1 which has the larger gap Δ_1 . We have also attempted to fit the data only in the intermediate temperature range where the effect of impurities is relatively smaller and we found fitting parameters similar to the reported above. Since our model does not include details of the Fermi surface shape, Fermi velocities and the densities of states, this is the best accuracy that we can achieve using this approach.

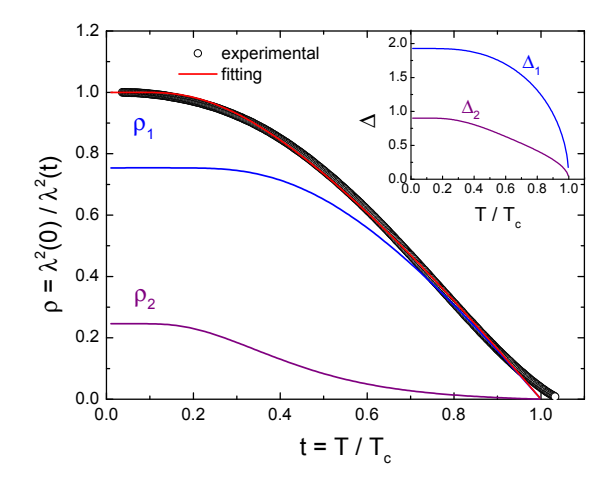


Figure 4.8 Main panel: calculate superfluid density $\rho_s = \lambda^2(0)/\lambda^2(T)$ in Fe(Te_{0.58}Se_{0.42}) is shown in symbols. $\lambda(0) = 560$ nm was used. Red solid line represents a fit to two gap model, $\rho = \gamma \rho_1 + (1 - \gamma)\rho_2$. Inset: superconducting gap functions, Δ_1 and Δ_2 .

The inset in Fig. 4.8 shows the behaviors of two superconducting gaps Δ_1 and Δ_2 versus temperature. Clearly, the smaller gap has significantly non-BCS temperature dependence. The zero temperature values of the energy gaps $\Delta_1(0)$ and $\Delta_2(0)$ are 2.5 meV $(\Delta_1(0)/k_BT_c = 1.93)$ and 1.1 meV $(\Delta_2(0)/k_BT_c = 0.9)$, respectively. From the previous measurements, such as μSR [131, 159] and penetration depth [94], two isotropic gaps were reported with gap values similar to our results. μSR studies in FeSe_{0.5}Te_{0.5} [131, 159] revealed two gaps of $\Delta_{\text{large}} \sim 2.6$ meV and $\Delta_{\text{small}} \sim 0.5$ -0.87 meV, and the penetration depth study [132] also showed that $\Delta_{\text{large}} \sim 2.1 \text{ meV}$ and $\Delta_{\text{small}} \sim 1.2 \text{ meV}$. According to scanning tunneling spectroscopy study, only one s-wave gap $\Delta \sim 2.3 \text{ meV}$ was observed in FeSe_{0.4}Te_{0.6} [160], which is similar to the large gap $\Delta_1(0)$ of our result. However, rather large single or multi-gaps were reported from specific heat [161], optical conductivity [162], point-contact Andreev reflectivity [163], and angle-resolved photoemission spectroscopy [164] suggesting strong-coupling superconductivity. The electronic specific heat in Fe(Te_{0.57}Se_{0.43}) [161] revealed two energy gaps with $\Delta_{\text{large}} \sim 7.4 \text{ meV}$ and $\Delta_{\text{small}} \sim 5.0 \text{ meV}$. From the optical conductivity in FeTe_{0.55}Se_{0.45}, two large energy gaps were also found with $\Delta_{\text{large}} \sim 5.1 \text{ meV}$ and $\Delta_{\text{small}} \sim 2.5 \text{ meV}$. The point-contact Andreev reflectivity in FeTe_{0.55}Se_{0.45} is consistent with single gap s-wave symmetry with $\Delta(1.70\text{K}) \sim 3.8$ meV. Angle-resolved photoemission spectroscopy in FeTe_{0.7}Se_{0.3} [164], an s-wave single gap of $\Delta \sim 4$ meV was also observed. Overall, the pairing symmetry in FeTe_{1-x}Se_x is still under debate, but our results strongly suggest a two-gap scenario with significant pair-breaking scattering.

4.2
$$Ca_{10}(Pt_3As_8)((Fe_{1-x}Pt_x)_2As_2)_5 (0.028 \le x \le 0.097)$$

Recently, a new family of Fe-based superconductors (FeSCs) with PtAs intermediary layers has been reported [165]. In particular, $Ca_{10}(Pt_nAs_8)[(Fe_{1-x}Pt_x)_2As_2]_5$ with n=3 (the 10-3-8 phase) and n=4 (the 10-4-8 phase) have been described [34, 166, 167, 168]. Whereas the 10-3-8 phase with rare triclinic symmetry shows superconducting T_c up to 13 K upon Pt-doping, the superconductivity of a tetragonal 10-4-8, stabilizes at a higher T_c of 38 K [167]. The availability of high purity single crystals with well - controlled level of Pt doping makes the 10-3-8 system particularly attractive [34, 166, 167, 168]. Two unique features distinguish the 10-3-8 system from other FeSCs. First, the anisotropy of the 10-3-8 system, $\gamma_H(T_c) \equiv H(T_c)_{c2,ab}/H(T_c)_{c2,c} \sim 10$ [34], is much larger than 2-4 in the 122 systems and even larger than 7-8 in the 1111 systems [169, 170, 171]. Second, a clear separation of structural (magnetic) instability and superconductivity in the T(x) phase diagram, suggested by transport measurements [34] and supported by NMR measurements [141] and by direct imaging of structural domains [33]. This is distinctly different from the 122 pnictides, where these two order parameters coexist up to the optimal doping [172].

In the cuprates, the low dimensionality of the electronic structure is believed to be responsible for their high T_c and highly anisotropic gap (d-wave) [173]. Despite obviously layered structure, the electronic anisotropy of most - studied 122 prictides is rather low, with $\gamma_H(T) \sim 2-4$ at $T = T_c$ and decreasing upon cooling [169, 170, 171]. Moreover, the

superconducting gap in the 122 pnictides is rather isotropic at the optimal doping, but evolves towards nodal structure at the dome edges [102]. To check whether the electronic anisotropy plays a role in the structure of the superconducting gap, highly anisotropic pnictides without complications due to coexisting phases and well - controlled doping level are needed and the 10-3-8 system fits these requirements.

In this section, we discuss $\lambda(T)$ in the 10-3-8 crystals in the underdoped regime up to optimal doping. The low-temperature penetration depth exhibits power-law variation, $\Delta \lambda = AT^n$, with the exponent n decreasing towards the edge of the dome. This behavior is similar to the lower-anisotropy BaK122 (hole doped) and BaCo122 (electron doped). We conclude that neither the anisotropy (at least, up to $\gamma_H \sim 10$) nor the coexistence of superconductivity and magnetism play a significant role in determining the superconducting gap structure in FeSCs.

Single crystals of $Ca_{10}(Pt_3As_8)((Fe_{1-x}Pt_x)_2As_2)_5$ were synthesized as described elsewhere [34]. The compositions of six samples were determined with wavelength dispersive spectroscopy (WDS) electron probe microanalysis as $x = 0.004\pm0.002$, 0.018 ± 0.002 , 0.028 ± 0.003 , 0.041 ± 0.002 , 0.042 ± 0.002 , and 0.097 ± 0.002 .

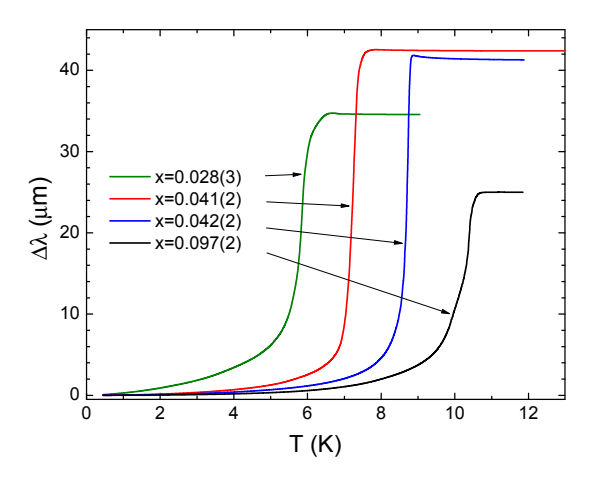


Figure 4.9 Variation of the London penetration depth, $\Delta\lambda(T)$, in the full temperature range for four underdoped compositions of the 10-3-8 system. T_c increases with Pt-doping, x, as indicated in the legend.

Figure 4.9 shows the variation of the London penetration depth, $\Delta\lambda(T)$, during a temperature sweep through the superconducting transition in 10-3-8 single crystals with x = 0.028, 0.041, 0.042, and 0.097. T_c monotonically increases with x, consistent with the transport measurements of the crystals from the same batches [34].

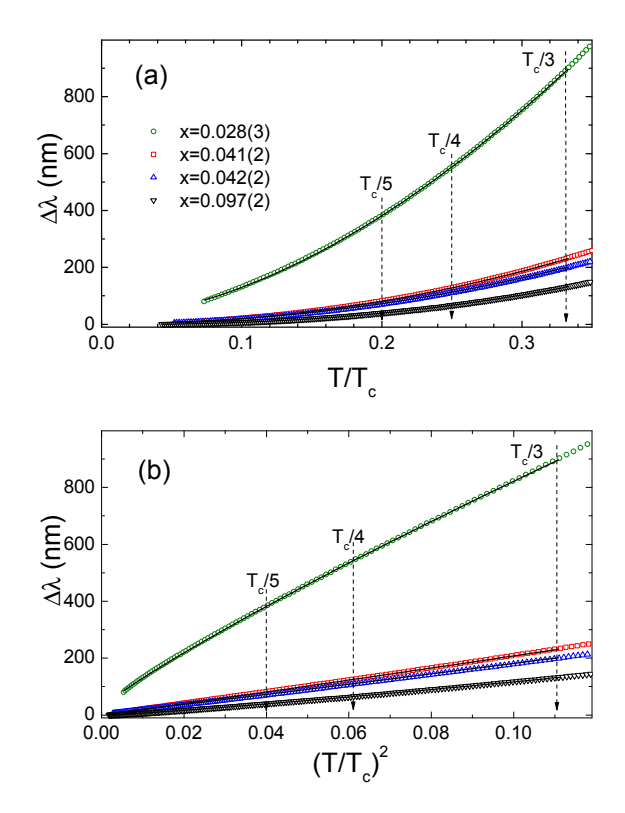


Figure 4.10 $\Delta\lambda(T)$ with temperatures between 500 mK and $\sim T_c/3$, plotted against (a) T/T_c and (b) $(T/T_c)^2$ for the 10-3-8 samples with $x=0.028,\ 0.041,\ 0.042,\$ and 0.097. The vertical dashed lines indicate the upper limits of the fitting ranges, $T_c/5$, $T_c/4$ and $T_c/3$. The solid lines are representative fits to $\Delta\lambda = AT^n$ for each doping, conducted with the upper limit of $T_c/3$. The resulting exponents n for all three fitting ranges are shown in Fig. 4.11 (a).

Figure 4.10 shows $\Delta\lambda(T)$ plotted against (a) linear, T/T_c , and (b) quadratic, $(T/T_c)^2$, normalized temperature scales. For the quantitative analysis, $\Delta\lambda(T)$ was fitted to a power-law, $\Delta\lambda(T) = AT^n$. To examine the robustness of the fits, the fitting range was varied from base temperature to $T_c/3$, $T_c/4$, and $T_c/5$ (indicated by vertical dashed lines

in Fig. 4.10). In Fig. 4.10, the symbols are experimental data and the solid lines show representative fits with the upper limit of $T_c/3$. The resulting exponents n for all three fitting ranges are shown in Fig. 4.11 (a). Figure 4.11 (b) shows the prefactor A obtained at a fixed n = 2 for different fitting ranges. To compare samples with different doping levels we used the average values (over three different fitting ranges), n_{avq} and A_{avq} .

As shown in Fig. 4.11 (a), n_{avg} decreases from 2.36 to 1.7 and the prefactor, A, dramatically increases (fivefold) as x decreases from nearly optimal doping of x = 0.097 towards heavily underdoped x = 0.028. This behavior signifies a much larger density of quasiparticles thermally excited over the gap minima in the underdoped compositions.

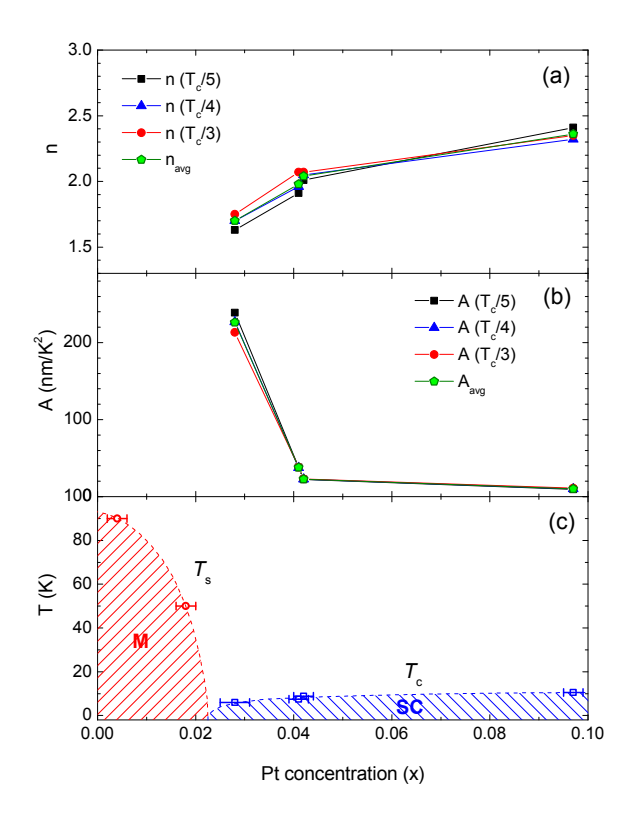


Figure 4.11 Results of the power-law fits with three different upper limits, indicated by dashed lines in Fig. 4.10 are shown along with the average values. Panel (a): the exponent n, obtained by keeping A and n as free parameters. Panel (b): the pre-factor A, obtained at a fixed n=2. Panel (c) shows the doping phase diagram with the magnetic (M) and superconducting (SC) phases clearly separated as a function of Pt-doping (x). T_s measured from resistivity [34] and T_c from TDR (this work).

A similar doping-dependent evolution of $\lambda(T)$ was found in BaCo122 [155]. For that compound, it was suggested that the underdoped side is significantly affected by the coexisting magnetic order and was explained by an increasing gap anisotropy when moving towards the edge of the "superconducting dome", consistent with thermal conductivity [77, 78] and specific heat [65] studies. In the present case of the 10-3-8 system where magnetism and superconductivity are separated, Fig. 4.11 (c), this doping-dependent evolution of n and A suggests that the development of the anisotropy of the superconducting gap upon departure from the optimal doping is a universal intrinsic feature of iron-pnictides, and is not directly related to the coexistence of magnetism and superconductivity.

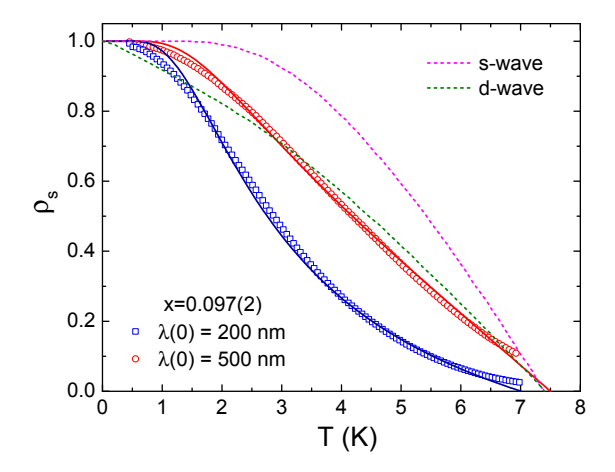


Figure 4.12 Superfluid densities, $\rho_s(T)$, of the optimally doped 10-3-8 sample with x = 0.097 for $\lambda(0) = 200$ nm (squares) and 500 nm (circles), which cover extremes of $\lambda(0)$ in FeSCs. Solid lines are the fits from the two-gap (s-wave) γ model [154]. For comparison, $\rho_s(T)$ for single-gap s-, and d-wave cases are shown as dashed lines.

The low-temperature exponent n, is sensitive to the gap anisotropy, but does not reflect possible multi-gap structure typical for the pnictides [102]. Therefore we need to analyze the superfluid density in the full temperature range. To avoid complications due to anisotropy we perform this analysis at the optimal doping. Figure 4.12 shows the superfluid density, $\rho_s(T) = (\lambda(0)/\lambda(T))^2$, calculated with $\lambda(0)$ of 200 nm and 500

nm, representing two extreme values reported for the pnictides [31]. Clearly, single - gap d-wave and s-wave are very far from the data. A much better agreement was found by using a self - consistent two-gap (s-wave) γ model [154], which only deviates at the low temperatures, presumably due to pairbreaking scattering [157]. The ratio of the superconducting gaps is about 2, similar to other FeSCs.

To summarize our findings, we observe substantial increase of the gap anisotropy in more underdoped compositions of the 10-3-8 system despite a clear separation of superconducting and magnetic domains on the T(x) phase diagram. Interestingly, similar separation is also reported in the 1111 compounds that have similarly high electronic anisotropy [174, 175]. The evolution of the gap anisotropy with doping may signify a transition between different pairing mechanisms in the different parts of the superconducting dome, for example, evolving from magnetic- to orbital-fluctuation mediated superconductivity [176, 177, 178]. Alternatively, the gap can become progressively more anisotropic within the same universal pairing scenario based on competing inter-band coupling and intra-band Coulomb repulsion and pair-breaking impurity scattering [179, 180, 181].

4.3 Ba_{1-x}K_xFe₂As₂ (0.13
$$\leq x \leq$$
 0.4)

The experimental determination of the symmetry of the superconducting gap is important for understanding the mechanism of superconductivity in iron-based superconductors [36, 182]. Measurements of London penetration depth [86, 85, 140], thermal conductivity [77, 78] and specific heat [72, 65, 183] in electron doped Ba(Fe_{1-x}Co_x)₂As₂ (BaCo122) suggest that superconducting gap shows strong evolution with doping, developing nodes at the dome edges [78, 184, 181]. This doping-evolution is consistent with observations of a fully gapped superconductivity in effectively close to optimally-doped LiFeAs [185, 186, 94, 187] and nodal superconductivity in effectively overdoped KFe₂As₂ [188, 189, 84]. It is also consistent with predicted doping-evolution for the s_{\pm}

model [190, 181]. On the other hand, nodal behavior is observed at all doping levels in isovalently substituted $BaFe_2(As_{1-x}P_x)_2$ (BaP122) [191]. This noteworthy difference in two systems based on the same parent compound prompts a detailed study of the hole doped $Ba_{1-x}K_xFe_2As_2$ (BaK122). The superconducting gap in BaK122 was studied intensively using ARPES [139, 192], NMR [193], penetration depth [194, 195] and thermal conductivity [79, 189], however, no systematic doping - dependent study reaching the dome edges was undertaken so far.

In this section we study the evolution of the temperature dependence of in-plane London penetration depth, $\Delta\lambda(T)$, in high quality single crystals of $\mathrm{Ba}_{1-x}\mathrm{K}_x\mathrm{Fe}_2\mathrm{As}_2$. We find that the optimally doped samples show exponentially weak temperature dependence in $T\to 0$ limit, suggesting a fully gapped superconductivity. This conclusion is consistent with the temperature-dependent superfluid density in these samples, which can be well fitted using self-consistent γ -model with two full gaps in the clean limit [154]. The lowest- T_c samples show an exceptionally strong sub-quadratic temperature dependence. Fitting the experimental $\Delta\lambda(T)$ below $T_c/3$ to a power-law, $\Delta\lambda(T) = AT^n$, we find a monotonic decrease of the exponent n with concomitant sharp increase of the pre-factor A towards the low x edge of the superconducting dome. Comparison with close to T-linear behavior found in heavily overdoped KFe₂As₂ [84], suggests a universal development of nodes at the edges of the superconducting dome in both electron- and hole-doped $\mathrm{BaFe}_2\mathrm{As}_2$ -based superconductors.

Single crystals of $\text{Ba}_{1-x}K_x\text{Fe}_2\text{As}_2$ were grown using high temperature FeAs flux method [196]. $\Delta\lambda(T)$ was measured using tunnel-diode resonator technique [97, 101]. Placing a sample into the inductor causes the shift of the resonant frequency, $\Delta f(T) = -G4\pi\chi(T)$. Here $4\pi\chi(T)$ is magnetic susceptibility and G is a calibration constant determined by physically pulling the sample out of the coil. With the characteristic sample size, R, $4\pi\chi = (\lambda/R) \tanh(R/\lambda) - 1$, from which $\Delta\lambda$ can be obtained [100, 101]. The excitation field in the inductor, $H_{ac} \sim 20$ mOe, is much smaller than H_{c1} .

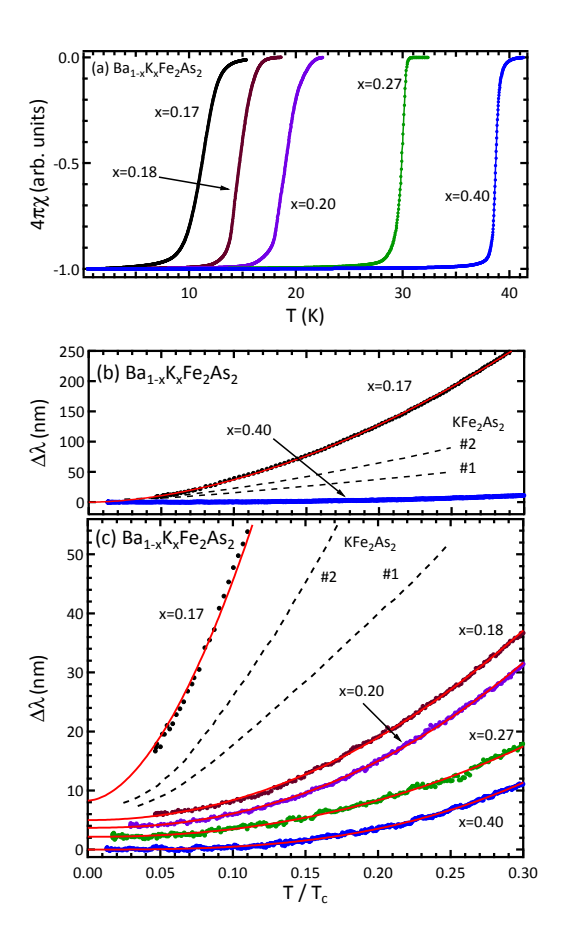


Figure 4.13 Temperature variation of London penetration depth $\Delta\lambda(T)$ in under doped $\mathrm{Ba}_{1-x}\mathrm{K}_x\mathrm{Fe}_2\mathrm{As}_2$. (a) Normalized $\Delta\lambda(T)$. (b) and (c) Low-temperature parts of $\Delta\lambda(T)$. Experimental data are displayed with solid circles. Solid red line represent power-law fitting curves. Two dashed lines are data for pure KFe₂As₂ from Ref. [191].

To compare sharpness of the superconducting transition, Fig. 4.13(a) shows normalized RF susceptibility of $Ba_{1-x}K_xFe_2As_2$ samples used in this study. The superconducting transition remains quite sharp even for the most underdoped samples where $T_c(x)$ is very sensitive to small variations of x. The values of x were determined by the empirical fit of the experimental $T_c(x)$ data [196, 197]. The values of T_c were determined from the position of the maximum in the first derivative, $d\Delta\lambda(T)/dT$. In our samples we obtained T_c of 11.2, 14.5, 18.6, 30.0, and 38.7 K, corresponding to potassium concentrations of x = 0.17, 0.18, 0.20, 0.27, and 0.40, respectively. The low-temperature variation of

 $\Delta\lambda(T)$ up to $T_c/3$ is shown in Figs. 4.13(b) and (c). Figure 4.13(b) compares the data for limiting compositions x=0.17 and 0.40, revealing a big difference in the magnitude of $\Delta\lambda(T)$. Two curves for pure KFe₂As₂ are shown for reference [191]. Figure 4.13(c) shows $\Delta\lambda(T)$ on the same scale for all concentrations. The data are offset for clarity and red lines represent the power-law fit. However, a closer look shows significant deviations of the data in heavily underdoped (x = 0.17) and in optimally doped (x = 0.4) samples. At lowest temperatures, it becomes significantly sub-quadratic for the former and closer to exponential for the latter.

First we attempted to fit the data for two highest T_c samples to the single gap s-wave BCS function, $\Delta\lambda(T)/\lambda(0) = \sqrt{\pi\Delta_0/2k_BT} \exp(-\Delta_0/k_BT)$, where Δ_0 is the size of gap at T=0. The Δ_0 values from the best fittings are 0.73 k_BT_c and 0.87 k_BT_c for x=0.27, and 0.40, respectively. While the fit quality was good, both Δ_0 values are much smaller than in single full-gap superconductors where $\Delta_0=1.76~k_BT_c$. Such small gaps are expected in superconductors with $\Delta_{\min}<\Delta_{\max}$, either due to gap angular variation (anisotropy) or variation between different Fermi surface sheets.

A standard way to analyze $\Delta\lambda(T)$ is to fit it from the lowest temperature up to $T_{\rm up} \approx T_c/3$. In a single -gap s-wave superconductor this limit is determined by reaching nearly constant value of the superconducting gap Δ_0 , below which the temperature dependence is exponential. For various nodal gaps, the dependence is expected to be power-law, T-linear for line nodes and T^2 for point nodes in clean limits. For the anisotropic gap or multi-gap superconductors with the variation of the gap magnitude over the Fermi surface between $\Delta_{\rm max}$ and $\Delta_{\rm min}$, the $T_{\rm up}$ is determined by $\Delta_{\rm min}$, while T_c by $\Delta_{\rm max}$, so that $T_{\rm up}$ range of characteristic temperature dependence can be smaller than $T_c/3$.

We therefore check the alteration of the fitting parameters by choosing different temperatures for the upper limit, $T_{\rm up} < T_c/3$. The dependence of n and A on $T_{\rm up}$ is shown in Fig. 4.14(b). The highest-and lowest- T_c samples exhibit monotonic increase and decrease of n on $T_{\rm up} \to 0$, approaching very different values of 4 and 1.5, respectively.

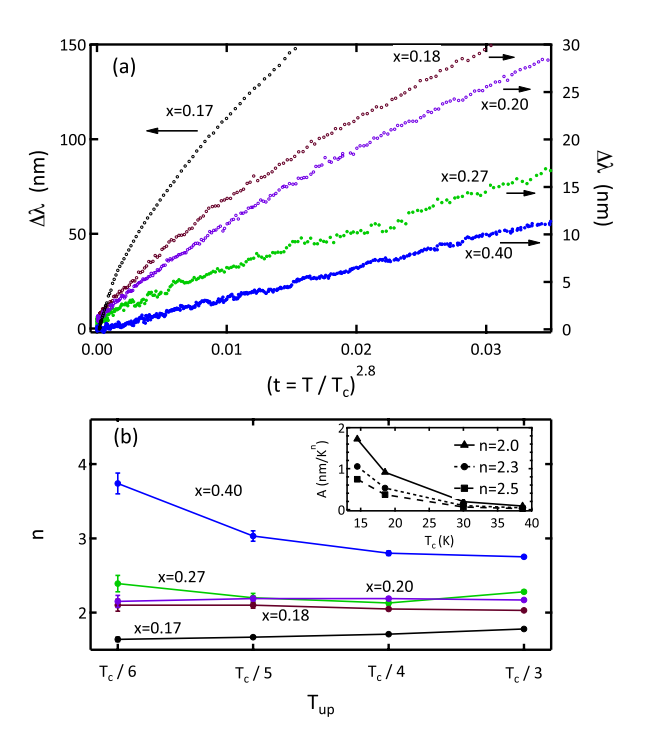


Figure 4.14 (a) $\Delta\lambda$ vs. $(T/T_c)^{2.8}$ up to $T_c/3$. (b) Variation of exponent n obtained from a power-law fitting, $\Delta\lambda = A(T/T_c)^n$, as a function of the upper end temperature of the fitting range. Inset: A vs. T_c . The three curves represented by triangle, circle, and square were obtained with fixed n = 2.0, 2.3, and 2.5, respectively.

The exponents n for samples with x = 0.18, 0.20, and 0.27 do not show a significant variation with $T_{\rm up} < T_c/3$, indicating robust power-law behavior, but show systematic increase of n with x. The decrease of n with decrease of x can be clearly seen by in the top panel of Fig. 4.14, in which all data are plotted vs $(T/T_c)^{2.78}$, where n = 2.78 is the exponent for the optimally doped samples. The dependence of the power-law pre-factor A on T_c was analyzed by fixing n=2.0, 2.3, and 2.5 and is shown in the inset revealing a significant increase with decreasing T_c . The A value for sample x=0.17 is 30 nm/K^{1.78}, out of scale for the plot and is not shown.

A smaller than weak-coupling value of Δ_{min} obtained from low-temperature BCS formula implies two-gap superconductivity and the analysis must be extended to the full-temperature range. The most convenient quantity is the superfluid density, which

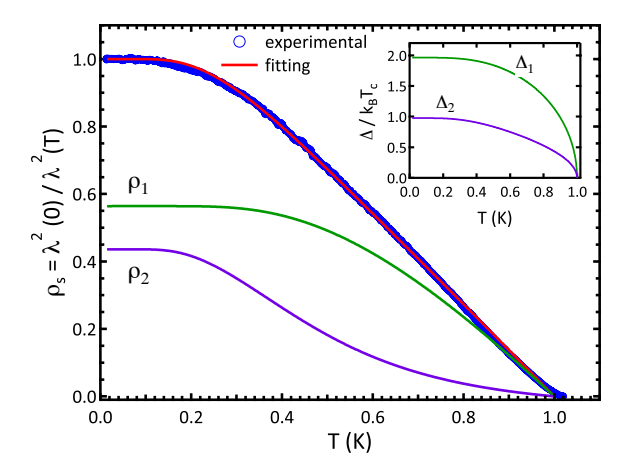


Figure 4.15 Symbols: superfluid density $\rho_s(T) = \lambda^2(0)/\lambda^2(T)$ calculated with $\lambda(0) = 200$ nm in Ba_{0.6}K_{0.4}Fe₂As₂ [198]. Solid lines represent the fit to a two-gap γ model, $\rho_s = \gamma \rho_1 + (1 - \gamma)\rho_2$. Inset: superconducting gaps $\Delta_1(T)$ and $\Delta_1(T)$ calculated self-consistently during the fitting.

can be calculated from the first principles. In the optimally doped samples, we fit the data using clean-limit γ -model [154]. Symbols in Fig. 4.15 show superfluid density, $\rho_s(T) =$ $\lambda^2(0)/\lambda^2(T)$, for the sample with x=0.40 calculated with $\lambda(0)=200$ nm determined by infrared spectroscopy experiments [198]. We note that the slope of superfluid density at T_c determined by using the Rutgers relation is -3.6 with $\Delta C = 125 \text{ mJ/mol-K}^2$ [199] and $\partial H_{c2}/\partial T|_{T_c}=-6.7$ [199], which is significantly different from experimental value -1.5 obtained by fitting the experimental ρ_s in Fig. 4.15. One natural explanation for such a large discrepancy between calculations and the experiment may be due to magnetic order parameter coexisting with superconductivity, but this has to be verified. In addition, the calculated value is somewhat big to account for multigap superconductivity. For further superfluid analysis, we use the experimental value $\lambda(0) = 200 \text{ nm}$ [198]. Solid lines show self-consistent γ -model fit for two-full-gap superconducting state [154] with $\rho_s = \gamma \rho_1 + (1 - \gamma)\rho_2$, where ρ_1 and ρ_2 are partial superfluid densities. Insert shows two superconducting gaps Δ_1 and Δ_2 calculated during the fitting procedure. The estimated gap values are 6.5 and 3.3 meV. Specific heat jump produced the value of ~ 6 meV for the larger gap [200].

Upon departure from optimal doping, the exponent n shows notable evolution with x decreasing from 4 to about 1.5. London penetration depth is very sensitive to pairbreaking disorder, modifying $\Delta\lambda(T)$ at low temperatures [89, 66]. In Ba122 - derived compounds it was also suggested experimentally [195, 194, 201, 157]. Within the s_{\pm} theory [57], $\lambda(T)$ should be exponential in the clean limit [94, 93]. However, pair-breaking scattering (which in this case can be caused by non-magnetic impurities and dopant ions) turn the behavior into a power-law with the exponent n approaching 2 in the dirty limit [90, 89, 202]. Since the superconductivity in BaK122 is induced by doping, we cannot ignore the effect of disorder on the variation of exponents. However, it would be natural to expect increase of scattering with x, and thus decrease of the exponent, opposite to the trend in our data. Similarly, disorder effect cannot explain nodal state in the end member of BaK122, very pure KFe₂As₂ with n=1.2 [191, 189]. In addition, our most underdoped sample shows the exponent n = 1.5 clearly well below the limiting value of 2 for pair-breaking scattering. Thus we conclude that the variation of the exponent n, found in our study, is caused by the changes in the superconducting gap structure with doping.

The evolution of the power-law behavior in $Ba_{1-x}K_xFe_2As_2$ superconductors is summarized in Fig. 4.16(a). Solid circles show exponent n with the error bar estimated from the fitting to the different temperature ranges (such as shown in Fig. 4.14(b)) and open circles show the pre-factor A calculated for a fixed exponent n=2.3. Also shown are the exponents for two stoichiometric (clean) compounds, KFe₂As₂ [191] and LiFeAs [94]. The dashed line represents our picture of the exponent variation with doping that, in our opinion, reflects developing anisotropy of the superconducting gap. To relate to the phase diagram, Fig. 4.16(b) shows magnetic and superconducting transitions vs doping from neutron scattering [197]. The pre-factors of the power-law fit show a sharp increase in the AFM region, similar to FeCo122 [155], which indicates microscopic coexistence of superconductivity and long-range magnetic order [203].

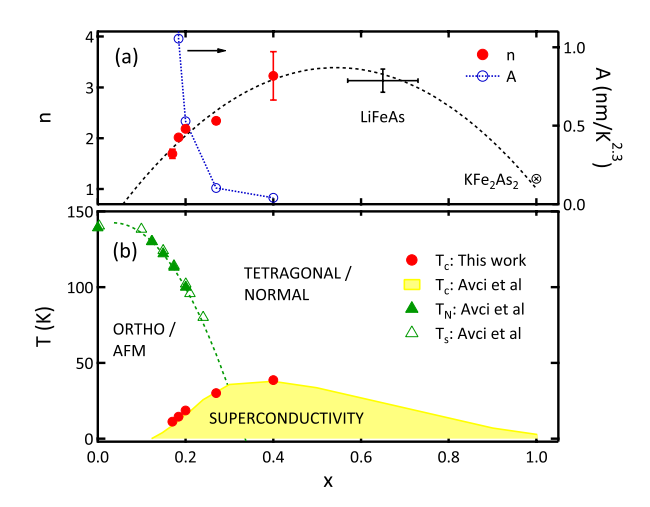


Figure 4.16 (a) n vs. x diagram. The red solid circles represent n from various temperature range between $T_c/6$ and $T_c/3$. The exponent $n \approx 1$ and 3.1 in KFe₂As₂ [191] and LiFeAs [94], respectively, are from elsewhere. (b) T-x phase diagram. The superconducting dome and AFM region were constructed with data from elsewhere [197].

In conclusion, the measurements of $\lambda(T)$ in $\mathrm{Ba}_{1-x}\mathrm{K}_x\mathrm{Fe}_2\mathrm{As}_2$ suggest the evolution of the superconducting gap upon departure from the optimal doping from full isotropic to highly anisotropic and, perhaps, nodal at the dome edges.

4.4 Full substitution of Fe with Pd: APd_2As_2 (A = Ca, Sr) and $SrPd_2Ge_2$

These compounds are interesting particularly because of compositional similarity to the newly discovered isostructral Fe-and Ni-pnictide superconductors with comparable T_c such as KFe₂As₂, BaNi₂As₂, and SrNi₂P₂. Although there is strong experimental evidence for nodal superconductivity in KFe₂As₂ (Ref. [191, 204]), the Ni-based ones have been shown to be fully gapped by thermodynamic and thermal transport measurements [205, 206]. This naturally prompts the question: what the structure of a superconducting gap is in these compounds? So far, not much work has been done on these materials in this direction. Tunneling spectroscopy between $0.17T_c$ and T_c is consistent with a

single, isotropic gap superconductor [207]. To verify this, however, the thermodynamic, thermal transport, and penetration depth measurements down to much lower temperatures are necessary to provide objective conclusions regarding the gap-symmetry in these superconductors.

In this section, we discuss London penetration depth, $\lambda(T)$, in single crystals of APd₂As₂ (A = Ca, Sr) and SrPd₂Ge₂ taken in a dilution refrigerator with temperatures down to 50 mK. The low - temperature variation of the London penetration depth, $\Delta\lambda(T)$, clearly indicates exponential saturation in all compounds. In APd2As2, the low temperature $\Delta\lambda$ is consistent with a BCS prediction for weak-coupling superconductor. In SrPd₂Ge₂, the thermodynamic Rutgers formula was used to estimate $\lambda(0) = 426$ nm which was used to calculate the superfluid density, $\rho_s(T) = \lambda^2(0)/\lambda^2(T)$. Analysis of $\rho_s(T)$ in the full temperature range shows that it is best described by a single - gap behavior, perhaps with somewhat stronger coupling.

4.4.1 APd₂As₂ (A = Ca, Sr)

Figure 4.17 shows the temperature variation of the ab-plane magnetic penetration depth, $\Delta\lambda(T)$, measured in CaPd₂As₂ and SrPd₂As₂ crystals, represented by open circles and triangles, respectively. The absolute value of the penetration depth was obtained using the TDR technique by matching the frequency shift, $\Delta f(T)$, to the skin depth, δ , calculated from the resistivity [208]. The superconducting transition temperature was determined as the temperature of the maximum of $\Delta\lambda(T)/dT$. The determined T_c 's are 1.34 K and 1.26 K for CaPd₂As₂ and SrPd₂As₂, respectively. These values are higher than the bulk T_c 's of 1.27(3) K and 0.92(5) K determined from respective $\Delta C_p(T)$ data [208]. Even so, the actual onset of the diamagnetic reponse is observed at even higher temperature Tc onset = 1.50 K and 1.72 K for Ca and Sr respectively. The temperature dependences of $\Delta\lambda$ for the two compounds up to T_c are shown in the inset of Fig. 4.17

At low temperatures, the $\Delta\lambda(T)$ in Fig. 4.17 of each sample shows a clear saturation

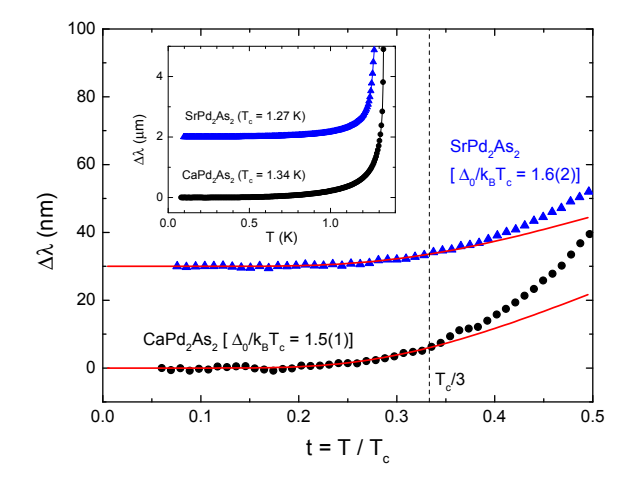


Figure 4.17 $\Delta\lambda(T)$ measured in CaPd₂As₂ (filled circles) and SrPd₂As₂ (filled triangles). The data for SrPd₂As₂ are shifted vertically upwards by 30 nm for clarity. The solid curve for each compound is the best fit of the data by s-wave BCS function for $T < 0.3T_c$. The vertical dashed line is the upper temperature limit for the fits. Inset: $\Delta\lambda(T)$ for both compounds up to $T = T_c$. The data for SrPd₂As₂ are all shifted upwards by 2 μ m for clarity.

on cooling, which is an indication of a fully-gapped superconducting order parameter in both compounds. The experimental data are fitted well up to $T = T_c/3$ by a single-gap BCS equation. The fitting parameters are $\lambda(0) = 210 \pm 60$ nm and $\Delta(0)/k_B = 2.02 \pm 0.14$ K for Ca and $\lambda(0) = 170 \pm 70$ nm and $\Delta(0)/k_B = 2.05 \pm 0.20$ K for Sr. The listed errors are systematic errors obtained from the spread of the fitting parameters depending on different choices of the upper temperature limit near $T_c/3$.

Using the bulk T_c values determined by heat capacity measurements [208] and the above values of $\Delta(0)/k_B$, we obtain $\alpha = 1.59(14)$ for Ca and 2.22(0.32) for SrPd₂As₂. The value of α for CaPd₂As₂ is identical within the error vars to the value of 1.58(2) in Eq that was determined from the heat capacity jump, both of which are smaller than the BCS value 1.764 expected for an isotropic weak-coupling BCS superconductor. This reduction is most likely due to a moderate anisotropy of the order parameter rather than multiple order parameters because well-known multi-gap superconductors such as MgB₂, NbSe₂, and LiFeAs have shown much lower values of alpha for the smaller gap.

The accuracy of alpha for Sr that we could write down is uncertain, and will therefore not be further discussed.

4.4.2 SrPd₂Ge₂

Superconductivity in the tetragonal ThCr₂Si₂-type SrPd₂Ge₂ was discovered first in polycrystalline [209] and later in single crystals [210] with the superconducting phase transition temperature (T_c) at 3.0 K and 2.7 K, respectively. The upper critical field (H_{c2}) was estimated to be 4920 Oe at T=0 by using Helfand-Werthamer (HW) theory [211] based on the experimental data obtained only down to $T=0.7T_c$ [210]. It has been found that T_c and H_{c2} can be slightly increased by chemical doping [212]. The London penetration depth and coherence length are reported to be $\lambda(0)=566$ nm and $\xi(0)=21$ nm [207] and $\lambda(0)=345\pm30$ nm $\xi(0)=25.6\pm0.5$ nm [213]. These values give the Ginzburg - Landau parameter of $\kappa=27$ [207] and $\kappa=13.5$ [213], which makes SrPd₂Ge₂ a strong type-II superconductor. Furthermore, thermodynamic [210] and tunneling spectroscopy measurements are consistent with a slightly strong - coupling s-wave Bardeen-Cooper-Schrieffer (BCS) superconductor with the zero-temperature value of the superconducting gap of $\Delta_0 \approx 2k_B T_c$ [207, 213], - not far from the weak coupling value of 1.76.

Figure 4.18 shows temperature variation of the in-plane London penetration depth, $\Delta\lambda(T)$, measured in a single crystal of SrPd₂Ge₂ superconductor which exhibits a very sharp superconducting phase transition at $T_c = 2.7$ K as shown in the inset, indicating a high quality, homogeneous sample. In the main panel, $\Delta\lambda(T)$ is shown with temperatures up to about $0.67T_c$. The saturation in $T \to 0$ limit and almost flat temperature dependence, $\Delta\lambda(T_c/3) < 10$ nm, indicate fully gapped superconductivity. Experimental $\Delta\lambda(T)$ can best fit to a power-law function, $\Delta\lambda(T) = AT^n$, with the exponent of $n = 2.7 \pm 0.1$ and pre-factor of $A = 12.2 \pm 0.4$ nm/K^{2.7}. The fitting curve is shown in red solid line. A power-law function with such a high exponent has very weak vari-

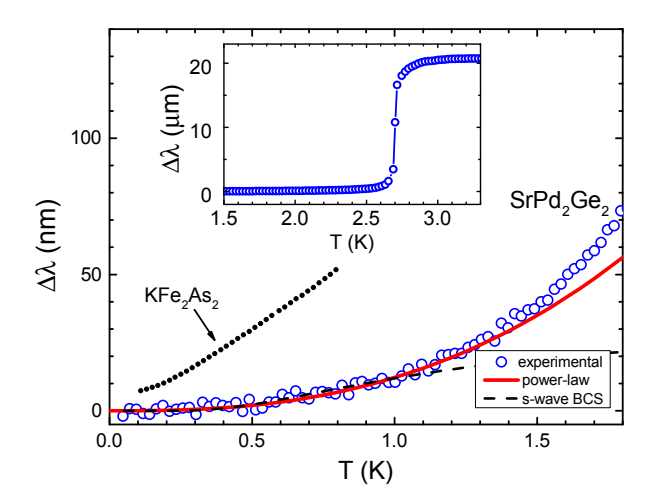


Figure 4.18 In-plane London penetration depth in a single crystal of $SrPd_2Ge_2$. Main panel: Open circles represent experimental data. Solid and dashed lines represent power-law and BCS (single gap s-wave) low - temperature fitting. Dotted shows the data for KFe_2As_2 taken from Ref. [191] for comparison. Inset: London penetration depth in the full temperature range demonstrating a sharp transition at $T_c=2.7~{\rm K}$

ation at low temperatures, indistinguishable from the exponential behavior which is predicted for a fully open superconducting gap. In fact, the BCS low - temperature form, $\Delta\lambda(T) = \lambda(0)\sqrt{\pi\Delta_0/2k_BT} \exp(-\Delta_0/k_BT)$, where Δ_0 is the maximum gap value at T=0, fits the data equally well for $T < T_c/3$ where it is expected to be valid. However, the best fitting is achieved with $\lambda(0)=50$ nm and $\Delta_0=0.74k_BT_c$. The latter is impossible in the single - gap clean limit where $\Delta_0\approx 1.76k_BT_c$ is expected. The value of $\lambda(0)$ is also much smaller than the reported value of 566 nm [207]. Similar low - temperatures features can be seen in two - band superconductors such as MgB₂ (Ref. [18]), 2H-NbSe₂ (Ref. [214]), Lu₂Fe₃Si₅ (Ref. [215]), and more recently LiFeAs (Ref. [94]). However, as we show below, analysis of the superfluid density in the full temperature range is inconsistent with a two - gap clean behavior. Instead, it is more likely that we are dealing with moderate pair - breaking scattering (maybe due to well-known magnetic impurities in Pd) which results in a finite density of states inside the gap. We also point out that these temperature variation is very small compared to a known nodal

superconductor KFe₂As₂ (Ref. [191, 204]) with similar T_c , but exhibiting much stronger temperature dependence of $\Delta\lambda$, indicating significant amount of quasiparticles generated at the low temperatures, most likely due to nodes in the gap.

For a metallic sample, the measured penetration depth above T_c is determined either by the skin depth δ or sample size. In case of skin depth limiting, the value of $\lambda(T > T_c)$ shown in the inset in Fig. 4.18 is one half of the actual skin depth [111]. Therefore, we can estimate normal state resistivity from the measurements using $\rho = (2\pi\omega/c^2)\delta^2$ [94]. For SrPd₂Ge₂ with $\omega/2\pi = f_0 = 17$ MHz and $\delta/2 \approx 20~\mu\text{m}$, the calculated resistivity is approximately 12 $\mu\Omega$ cm which is much less than the experimental value of 68 $\mu\Omega$ cm (Ref. [210]). Therefore, we conclude that it is in a sample - size limited regime. Using the same equation, the estimated skin depth is 180 nm which is close to half width of the sample.

Finally, we note that the data exhibit a smooth transition from superconducting penetration depth to the normal state between $T = T_c$ and $T^* \approx 3.0$ K, which has also been seen in transport measurement. [210] Interestingly, $T^* = 3$ K is the onset of superconductivity observed in a polycrystalline sample [209]. Similar feature has also been observed in a related superconductor BaNi₂As₂ [216]. Perhaps this feature requires further study.

While the low - temperature behavior is important, the superconducting gap can be probed at all energy scales by the analysis the superfluid density, $\rho_s(T) = \lambda^2(0)/\lambda^2(T)$, in the entire temperature range [102]. However, superfluid density requires knowledge of the absolute value of $\lambda(0)$. For SrPd₂Ge₂ $\lambda(0) = 566$ nm was estimated using a dirty limit [207] and $\lambda(0) \approx 390$ nm was extracted from field - dependent magnetization [210] within the London approximation and $\lambda(0) \approx 345 \pm 5$ nm was estimated from the measurements of the field of first penetration [213]. So, the variation of the literature values is quite significant and we have to resort to another, thermodynamic, approach based on the Rutgers formula. In the Ginzburg-Landau regime, i.e. near T_c , it can be

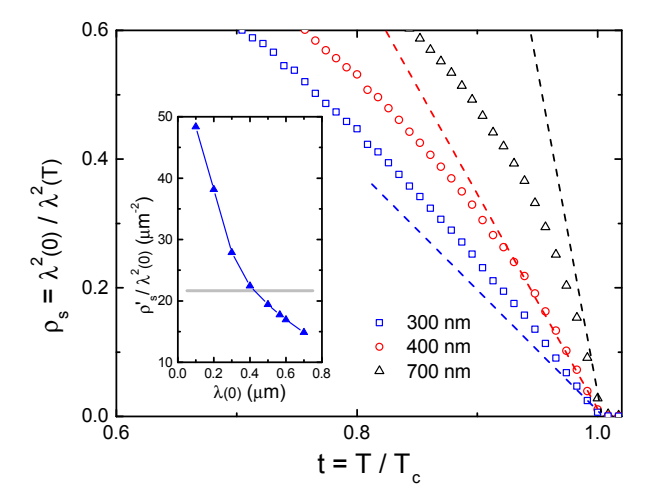


Figure 4.19 Main panel: Calculated superfluid density, ρ_s , with various $\lambda(0)$'s. The slope of dashed lines was determined with ΔC_p and $|dH_{c2}/dT|_{T_c}$ using the Rutgers formula as described in the text. Inset: Variation of $|\partial \rho_s/\partial t|_{T_c}/\lambda^2(0)$ with varying $\lambda(0)$. Here ρ_s' was determined from the experimental data. The gray band is a theoretical estimate with 5% hypothetical error in ΔC_p and $|dH_{c2}/dT|_{T_c}$.

shown that

$$\left| \frac{\partial \rho_s}{\partial t} \right|_{T_c} = \frac{16\pi^2 \lambda^2(0)}{\phi_0 |\partial H_{c2}/\partial T|_{T_c}} \Delta C_p \tag{4.2}$$

where $\phi_0 = 2.07 \times 10^{-7}$ G cm² is a flux quantum and $|\partial H_{c2}/\partial T|_{T_c} = 0.26$ T/K is determined experimentally [124]. Specific heat jump $\Delta C_p = 7381$ erg/cm³K is taken from Ref. [212]. Applying these thermodynamic values suggests $|\partial \rho/\partial t|_{T_c}/\lambda^2(0) = 21.7$ μ m⁻² where $t = T/T_c$ is the reduced temperature. This quantity can be compared with the actual slope of calculated $\rho_s(t)$ with various $\lambda(0)$ at T_c as shown in Fig. 4.19. In the main panel, the open symbols represent the calculated superfluid density with 300, 400, and 700 nm in triangle, circle, and square, respectively. The dashed lines are determined with the slope calculated by Eq. 4.2 for three values of $\lambda(0)$ quoted above. The line with 400 nm shows very good agreement with calculated ρ_s while the line with 300 nm significantly underestimates, and the one with 700 nm overestimates. This procedure can be repeated with various values of $\lambda(0)$. The result is summarized in the inset where the solid triangle represents experimental slopes obtained by fitting experimental

data near T_c to a linear line. The gray horizontal band represents the theoretical value of $|\partial \rho/\partial t|_{T_c}/\lambda^2(0) = 21.7 \pm 2.2 \ \mu\text{m}^{-2}$ determined with a 10 % hypothetical error in $|\partial H_{c2}/\partial T|_{T_c}$ and ΔC_p . In this way, $\lambda(0)$ can be determined at the intersection of the theoretical line and experimental results, which provides that $\lambda(0) = 426 \pm 60$ nm that lies between the literature values. With this value, the slope of ρ_s at T_c is determined to be -3.9.

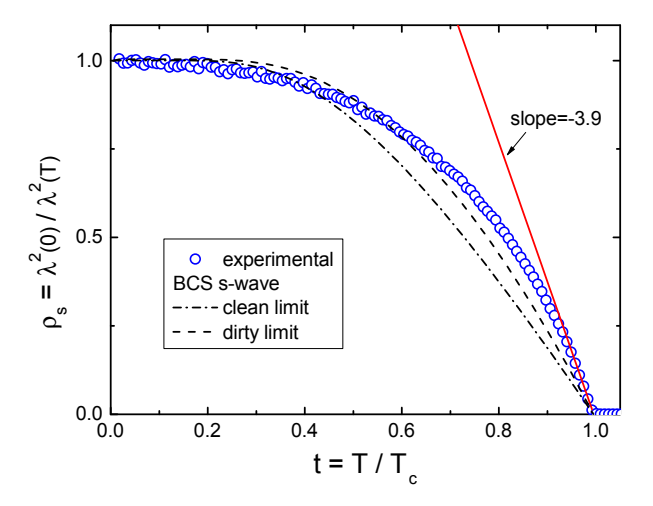


Figure 4.20 Calculated superfluid density, $\rho_s(T) = \lambda^2(0)/\lambda^2(T)$ using $\lambda(0) = 426$ nm. Open circles represent the experimental data. The dashed dots and dashed lines represent single - gap weak - coupling s-wave BCS superconductor in clean and dirty limit, respectively.

The calculated superfluid density with $\lambda(0) = 426$ nm is shown in Fig. 4.20. The dot - dashed and dashed lines show expectation for clean and dirty limit of a single-gap BCS superconductor in the weak - coupling limit, respectively. An attempt to use a two-gap (clean) γ -model [154] in the full-temperature range converges to a single - gap limit with $\Delta(0)/k_BT_c = 2.2$. Therefore, the gap symmetry of SrPd₂Ge₂ is most likely represented by a single gap s-wave, perhaps with somewhat enhanced coupling strength. It was noted previously that the shape of $\rho_s(T)$ is rather close to a nonlocal - limiting case, expected in type I superconductors such as aluminum and cadmium [217]. Similar argument was made in the work by T. K. Kim *et al.* in which SrPd₂Ge₂ appeared to be

type I according to the intrinsic electronic structure despite the fact that experimental $\xi(0)$ and $\lambda(0)$ put it in a strong type-II regime [207]. In any case, our study confirms that simple analysis with an isotropic Fermi surface is not sufficient and, perhaps, the results could be explained by taking into account a realistic band structure. We can, however, conclude that no nodes are present in the superconducting gap.

4.5 Summary

In Fe_{1+y}Te_{1-x}Se_x, a robust power-law behavior of the low-temperature London penetration depth was found for $\Delta\lambda(T) \propto T^n$ with $n \approx 2.1$ and 2.3 for Fe_{1.03}(Te_{0.63}Se_{0.37}) and Fe(Te_{0.58}Se_{0.42}), respectively. The absolute value, $\lambda(0) \approx 560 \pm 20$ nm, was determined in Fe_{1.03}(Te_{0.63}Se_{0.37}) by the Al-coating technique. The analysis of the superfluid density showed a clear signature of nodeless two-gap superconducting state with strong pair breaking effect.

In $Ca_{10}(Pt_3As_8)[(Fe_{1-x}Pt_x)_2As_2]_5$, the power-law fit of the low temperature part of $\Delta\lambda(T)$ showed that the exponent, n, monotonically changes from 2.36 at the optimal doping to 1.7 in heavily underdoped regime, which can be explained by an increasing anisotropy of the superconducting gap at the edges of the superconducting dome.

In $Ba_{1-x}K_xFe_2As_2$ (0.13 $\leq x \leq$ 0.40) where superconductivity coexists with magnetism, the measurements of $\Delta\lambda(T)$ suggest the evolution of the superconducting gap upon departure from the optimal doping from full isotropic to highly anisotropic and at the dome edges.

This doping evolution of gap anisotropy is universally found in all charge-doped Fepictides, $Ba_{1-x}K_xFe_2As_2$ and $Ca_{10}(Pt_3As_8)[(Fe_{1-x}Pt_x)_2As_2]_5$ similar to previous reports for $Ba(Fe,Co)_2As_2$, Na(Fe,Co)As, and $Na_{1-\delta}FeAs$. Observation of this evolution in all these materials irrespective of degree of anisotropy and coexistence vs. separation of magnetism and superconductivity in a phase diagram suggests that this evolution is intrinsic property of Fe-based superconductors. Theoretically it was suggested that this evolution comes from the competing inter-band pairing and intra-band repulsion in the superconducting pairing [179].

Related low T_c materials $SrPd_2Ge_2$ and APd_2As_2 (A=Ca,Sr) in which Fe is completely substituted by Pd show very different behavior. In these compounds, temperature variation of the London penetration depth is consistent with conventional full-gap superconductivity.

CHAPTER 5. EFFECT OF DISORDER ON LONDON PENETRATION DEPTH IN IRON-BASED SUPERCONDUCTORS

5.1 Superconducting gap structure in stoichiometric LiFeAs and KFe_2As_2

Studies of the superconducting gap structure play an important role in the determination of the mechanism responsible for superconducting pairing. In FeAs-based superconductors, the situation regarding the gap structure remains controversial. Since doping inevitably introduces scattering [218], which is pairbreaking in iron pnictides [219, 89, 90, 66, 157, 132], measurements of stoichiometric intrinsic superconductors become of utmost importance. LiFeAs and KFe₂As₂ with $T_c \approx 18$ K and 3.4 K are among very few such compounds. They are the cleanest systems with a high residual resistivity ratio (RRR) of about 50 [220] and 1000 [221], much higher than BaP122 (5 to 8 for different doping) [42], BaCo122 (3 to 4) [222] and BaK122 (7 to 10) [196], pure Ba122 (7 to 10 under pressure) [223]. Since T_c of LiFeAs decreases with pressure [224, 46], which is observed only in optimally and overdoped compounds [225], we can assign its "equivalent" doping level as slightly overdoped, as opposed to underdoped NaFeAs, whose T_c goes through a maximum with pressure [226] and heavily overdoped KFe₂As₂. This doping assignment is consistent with the temperature-dependent resistivity, discussed later. With the much reduced effect of pairbreaking scattering, comparison of these stoichio-

metric compounds can bring an insight into the intrinsic evolution of the superconducting gap.

In this chapter, we discuss experimental results on the in-plane London penetration depth, $\lambda(T)$, in single crystals of LiFeAs and KFe₂As₂ both of which do not show any apparent long-range magnetic ordering. While both penetration depth and the superfluid density in LiFeAs are both consistent with fully gapped superconductivity, both of them in KFe₂As₂ are consistent with a nodal superconductor. We use the self-consistent clean two-gap γ -model [154] to analyze the superfluid density in LiFeAs. Our results imply that the ground state of FeAs-based superconductors in the clean limit is not universal. Superconducting gap structure at almost optimal doping is given by s_{\pm} symmetry with two distinct gaps, $\Delta_1/T_c \sim 2$ and $\Delta_2/T_c \sim 1$, but effectively heavy-hole doped one shows nodal superconductivity.

5.1.1 Nodeless multi-gap superconductivity in LiFeAs

Single crystals of LiFeAs were grown in a sealed tungsten crucible using Bridgeman method [220, 227]. After growth, samples were only exposed to Ar in glovebox and transported under Ar in sealed ampoules. Immediately after opening, $(0.5-1) \times (0.5-1) \times (0.1-0.3)$ mm³ pieces of the same crystal (all surfaces cleaved in Apiezon N grease) were used for TDR, transport and magnetization measurements. Samples from two different batches were measured, and we found compatible results in all measurements, with bulk superconducting transition consistent with previous reports [220, 227]. In what follows we present all results for samples from batch #1. Low resistance contacts (~ 0.1 m Ω) were tin-soldered [228] and in-plane resistivity was measured using a four probe technique in Quantum Design PPMS. The transition temperature, T_c , was determined at the maximum of the derivative $d\Delta\lambda(T)/dT$, Table 5.1. The London penetration depth was measured with the TDR technique [101]. The sample was inserted into a 2 mm inner diameter copper coil that produced an rf excitation field (at $f \approx 14$ MHz) with amplitude

a power-law fitting with fixed n=3.1. Δ_0 was obtained from a s-wave BCS fitting, $\Delta\lambda(T)=\lambda_0\sqrt{\pi\Delta_0/2k_BT}\exp{-\Delta_0/k_BT}$. are obtained from a power-law fitting, $\Delta \lambda(T) = A'T^n$. A was obtained with Sample properties and parameters of exponential and power-law fits. T_c^{onset} is determined at the onset of superconducting transition in measured $\Delta\lambda(T)$ as cooling. T_c was determined at the maximum of $d\Delta\lambda/dT$. Both n and A' Table 5.1

$(\mathrm{pm/K^{3.1}})$ $\Delta_0 (k_B T_c)$	106.1 ± 0.7 1.09 ± 0.02	107.1 ± 0.7 0.94 ± 0.02	110.1 ± 0.9 0.95 ± 0.02
$A' (\mathrm{pm/K}^n) A (\mathrm{j}$	64.8 ± 4.8 1	136.9 ± 10.2 1	119.7 ± 12.4 1
n	0.7 ± 0.2 3.39 ± 0.04	2.96 ± 0.04	1.1 ± 0.2 3.05 ± 0.06
$\Delta T_c (\mathrm{K})$	0.7 ± 0.2	0.9 ± 0.2	1.1 ± 0.2
T_c (K)	17.5 ± 0.1	17.2 ± 0.1	16.9 ± 0.1
$T_c^{ m onset}(K)$	18.2 ± 0.1	18.1 ± 0.1	18.0 ± 0.1
sample		#5	#3

 $H_{ac} \sim 20$ mOe, much smaller than H_{c1} . Measurements of the in-plane penetration depth, $\Delta \lambda_{ab}(T)$, were done with $H_{ac} \parallel c$ -axis, while with $H_{ac} \perp c$ we measured $\Delta \lambda_{c,mix}(T)$ that contains a linear combination of λ_{ab} and λ_{c} [229].

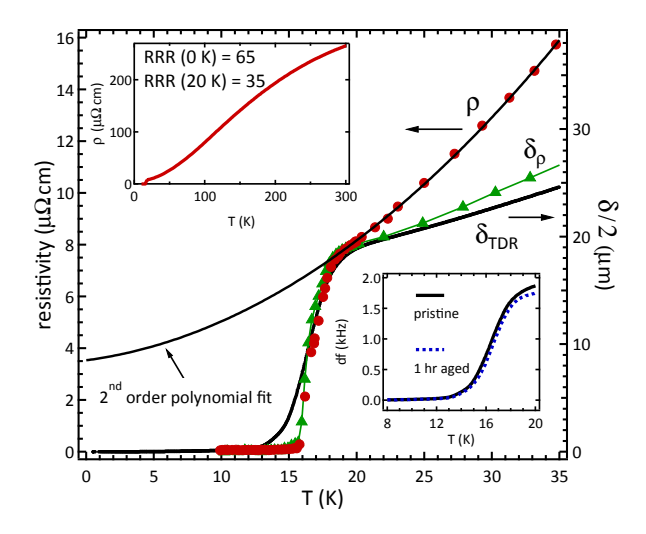


Figure 5.1 Left axis: resistivity (symbols) along with the 2^{nd} order polynomial fit from T_c to 50 K used to determine the residual resistivity, $\rho(0) = 3.7 \ \mu\Omega \cdot \text{cm}$. Right axis: skin depth, δ , measured by TDR, δ_{TDR} compared to that calculated from resistivity, δ_{ρ} . Upper inset: $\rho(T)$ in the full temperature range. Lower inset: TDR data for pristine and air-aged samples (see text).

The main panel in Fig. 5.1 shows the temperature-dependent resistivity, $\rho(T)$ (left axis), and skin depth, $\delta(T)$ (right axis). The resistive superconducting transition starts at 18 K and ends at 16 K as cooling. $\rho(T)$ up to room temperature is shown in the top inset. The residual resistivity ratio, $RRR = \rho(300K)/\rho(20~K) = 35$ and it reaches the value of 65 when extrapolated to T = 0 using a 2^{nd} order polynomial. This behavior is consistent with the T-dependent resistivity of BaCo122 in the overdoped regime [230]. The calculated skin depth, $\delta_{\rho}(T) = (c/2\pi)\sqrt{\rho/f}$, (in CGS units) compares well with the TDR data for $T > T_c$, where $\Delta f/f_0 = G[1 - \Re\{\tanh{(\alpha R)/(\alpha R)}\}]$, $\alpha = (1 - i)/\delta$ [231] when we use $\rho(300K)=250~\mu\Omega\cdot\text{cm}$, the lowest directly measured value among our crystals. A very good quantitative match of two independent measurements gives us a confidence in both resistivity data and the TDR calibration.

To check for degradation effects, a sample was washed and intentionally exposed to air for an hour and the measurements were repeated, as shown in the lower inset in Fig. 5.1. After the exposure, the sample surface lost its shiny metallic gloss and the total frequency shift through the transition (proportional to the sample surface area A) decreased. This reduction without affecting the transition temperature and width suggests that the degradation happens on the surface and superconductivity of our samples is bulk in nature.

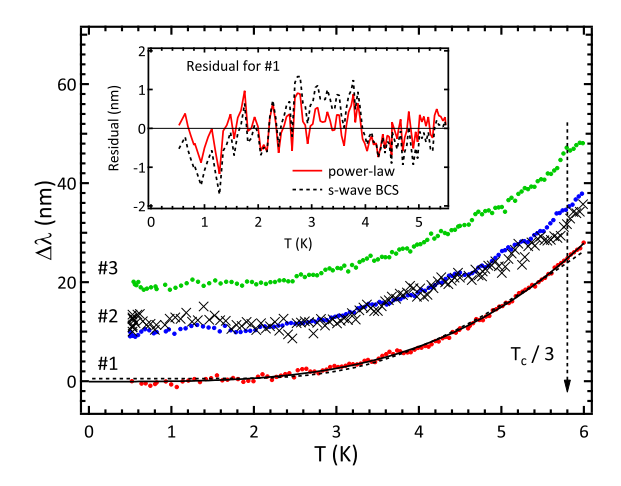


Figure 5.2 Main panel: $\Delta \lambda_{ab}(T)$ in three LiFeAs crystals (solid dots) and $\Delta \lambda_{c,mix}(T)$ for sample #2 (crosses). Analysis (shown for #1) was done assuming both power-law (solid lines) and exponential (dashed line) T-dependences. The data for samples #2 and #3 (shifted vertically for clarity by 10 and 20 nm, respectively) were analyzed in a similar way, see Table 5.1. Inset: comparison of the fit residuals for sample #1 for the power-law and exponential functions.

 $\Delta\lambda_{ab}(T)$ in three LiFeAs crystals is shown up to $T_c/3$ in Fig. 5.2 by solid dots. $\Delta\lambda_{ab}(T)$ was analyzed using (1) power-law, $\Delta\lambda(T) = AT^n$ (with A and n being free parameters), as expected for nodal superconductors, and (2) exponential BCS form, $\Delta\lambda(T) = \tilde{\lambda_0}\sqrt{\pi\Delta_0/2T}\exp{(-\Delta_0/T)}$ (with $\tilde{\lambda_0}$ and Δ_0 as free parameters). The best fit results for sample #1 are shown with solid (power-law) and dashed (exponential) lines. The fit residuals are shown in the inset. The exponential fit quality is as good as the power-law, although $\Delta_0/T_c = 1.09 \pm 0.02$ is smaller than the value of 1.76 expected for

a conventional single fully-gapped s-wave pairing and $\tilde{\lambda}_0 = 280 \pm 15$ nm is somewhat larger than the experimental 200 nm [128, 186]. This is naturally explained by two-gap superconductivity in LiFeAs. The superconducting T_c and best fit parameters (obtained from fitting up to $T_c/3$) for all samples are summarized in Table 5.1. T_c^{onset} was defined at 90% of the rf susceptibility variation over the transition: the mean T_c was defined at the maximum of $d\Delta\lambda(T)/dT$ and $\Delta T_c = T_c^{\text{onset}} - T_c$. Δ_0/T_c from the single-gap exponential BCS behavior. The power-law coefficient A' was obtained with the exponent n as a free parameter, while A was obtained with a fixed n = 3.1 (average of 3 samples). Crosses in Fig. 5.10 show $\Delta\lambda_{c,mix}(T)$ for sample #2. A clear saturation of $\Delta\lambda_{c,mix}(T)$ at low temperatures suggests exponential behavior of λ_c . Thermal contraction is ruled out as it would only give a total change of about 1 nm from 0 to T_c [232] and it could only lead to a non-exponential behavior.

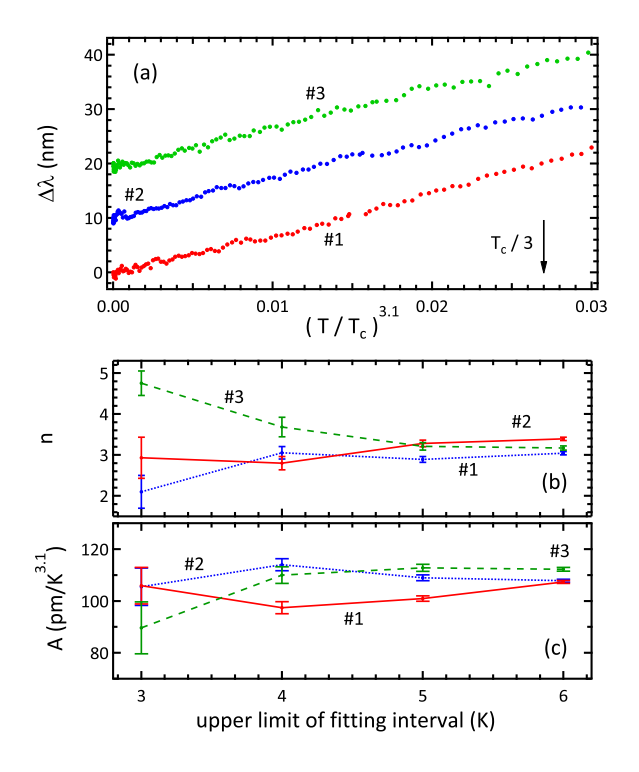


Figure 5.3 (a) $\Delta\lambda$ vs. $T^{3.1}$ (average exponent n over 3 samples); (b) exponent n and (c) prefactor A, obtained by fitting to $\Delta\lambda(T) \propto AT^n$ for various upper temperature limits shown on the x-axis.

Figure 5.3(a) shows $\Delta\lambda(T)$ vs. T^n with n=3.1 which is the average exponent for three samples. The dependence of the parameters, n and A, on the fitting temperature range is summarized in Fig. 5.3 (b) and (c), respectively. As expected, the exponent n is more scattered for the shortest fit interval, otherwise n and A do not depend much on the fitting range from base temperature to 6 K and give n > 3 for all samples, with the average value 3.13 ± 0.23 . With n fixed at this average value, we determined the prefactor $A = 107.8 \pm 2.1 \ \mu\text{m/K}^{3.1}$.

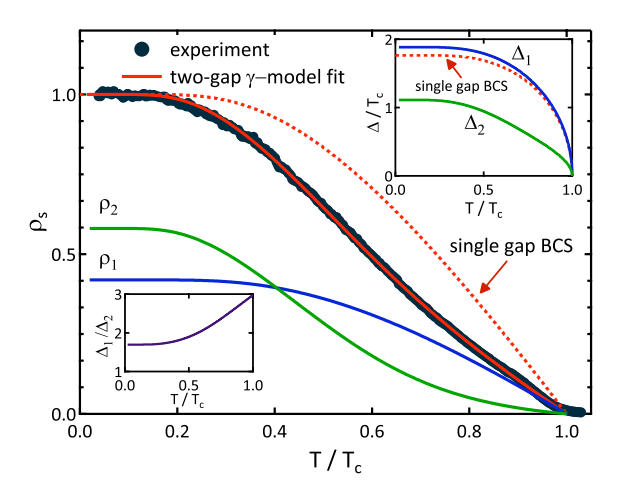


Figure 5.4 Symbols: superfluid density, $\rho_s(T)$ calculated with $\lambda(0) = 200$ nm. Solid lines represent the fit to a two-gap γ -model, $\rho_s = \gamma \rho_1 + (1 - \gamma) \rho_2$. Dashed line is a single-gap BCS solution. Upper inset: superconducting gaps, $\Delta_1(T)$ and $\Delta_2(T)$ calculated self-consistently during the fitting. Lower inset: Δ_1/Δ_2 as a function of temperature.

The superfluid density, $\rho_s(T) = [1 + \Delta \lambda(T)/\lambda(0)]^{-2}$ is the quantity to compare with the calculations for different gap structures. Figure 5.4 shows $\rho_s(T)$ for crystal #1 calculated with $\lambda(0) = 200$ nm [128, 186]. The calculated superfluid density using this $\lambda(0)$ value provides slope $\rho'_s(T_c)$ which is consistent with the Rutgers formula (see Fig. 3.3). A noticeable positive curvature above $T_c/2$ is similar to other Fe-based superconductors [233] and MgB₂ [18], suggesting multigap superconductivity. We analyze $\rho_s(T)$ in the framework of the self-consistent γ -model [154]. LiFeAs is a compensated metal with 2D cylindrical hole and somewhat warped electron Fermi surface sheets [234, 185]. To re-

duce the number of fitting parameters, yet capturing compensated multiband structure, we consider a simplest model of two cylindrical bands with the mass ratio, $\mu = m_1/m_2$, whence the partial density of states of the first band, $n_1 = \mu/(1 + \mu)$. The total superfluid density is $\rho_s = \gamma \rho_1 + (1 - \gamma)\rho_2$ with $\gamma = 1/(1 + \mu)$. We also use the Debye temperature of 240 K [126] to calculate T_c , which allows fixing one of the in-band pairing potentials, λ_{11} . This leaves three free fit parameters: the second in-band potential, λ_{22} , inter-band coupling, λ_{12} , and the mass ratio, μ . Figure 5.4 shows that $\rho_s(T)$ can be well described in the entire temperature range by this clean-limit weak-coupling BCS model. In the fitting, the two gaps were calculated self-consistently (which is the major difference between this one and the popular, but not self-consistent, α - model [17]) and the self-consistent $\Delta_1(T)$ and $\Delta_2(T)$ are shown in the upper inset in Fig. 5.4, while the gap ratio is shown in the lower inset indicating strong non-single-gap-BCS behavior of the small gap. The best fit, gives $\Delta_1(0)/T_c \sim 1.885$ and $\Delta_2(0)/T_c \sim 1.111$. As expected, one of the gaps is larger and the other is smaller than the single-gap value of 1.76, which is always the case for a self-consistent two-gap solution. The best fit parameters are: $\lambda_{11} = 0.630, \ \lambda_{22} = 0.642, \ \lambda_{12} = 0.061 \ \text{and} \ \mu = 1.384.$ The determined mass ratio gives $n_1 = 0.581$ and $\gamma = 0.419$. This is consistent with bandstructure calculations that yield $n_1 = 0.57$ and $\mu = 1.34$ (private communication with Mazin), and ARPES experiments that find $\mu \approx 1.7$ [185]. The effective coupling strength, $\lambda_{eff} = 0.374$, is not far from 0.35 estimated for 122 [235] and 0.21 for 1111 [236] prictides. (The value of 0.21 is an upper limit for the total electron-phonon interaction and the higher values would represent total strength of electron-boson coupling). The electron band with a smaller gap gives about 1.5 times larger contribution to the total ρ_s resulting in a crossing of the partial densities at low temperatures. Similar result was obtained from magnetization measurements [237]. We stress that while $\Delta_1(T)$, $\Delta_2(T)$ and μ (hence, n_1 , n_2 and γ) and λ_{eff} are unique self-consistent solutions describing the data, the coupling matrix λ_{ij} is not unique. There are other combinations that could produce similar results and λ_{ij}

has to be calculated from first principles.

5.1.2 Nodal superconducting gap in KFe_2As_2

The discussion of the superconducting pairing mechanism in iron-based superconductors was guided by early observations of full superconducting gap [28] and neutron resonance peak [61]. Based on these observations, Mazin *et al.* suggested pairing mechanism, in which superconducting order parameter changes sign between but the remains full on all sheets of the Fermi surface [57, 36]. Verification of this so called s_{\pm} pairing quickly became a focal point of studies of the superconducting gap structure.

Probably the first clear deviations from full-gap s_{\pm} scenario were found in NMR and heat capacity studies of KFe₂As₂ [188], which represents the terminal overdoped composition of (Ba,K)Fe₂As₂ series [44, 238] (we abbreviate the materials as K122 and BaK122 in the following). Systematic doping studies over the superconducting dome in electron-doped Ba(Fe_{1-x}Co_x)₂As₂ (BaCo122) [77, 78, 86, 155, 239, 63, 71], NaFe_{1-x}Co_xAs [240] and hole doped BaK122 [241] suggest that the superconducting gap in all these cases universally develops pronounced anisotropy at the dome edges. Thus K122 is not unique as a nodal superconductor, and understanding of its superconducting gap is of great importance for the whole iron-based family.

Evolution of the superconducting gap with doping distinguishes iron-based superconductors from cuprates, in which d-wave pairing is observed in all doping regimes. Several theoretical explanations of this fact were suggested [242, 243, 179]. Doping evolution was explained in s_{\pm} scenario as a result of the competition between inter-band pairing and intra-band Coulomb repulsion [179, 180]. Alternatively, it was explained as a result of a phase transition between s_{\pm} and d-wave superconducting states [243]. Important difference is that nodes in the gap structure are accidental in the first scenario, but symmetry protected in the second.

The conclusion about existence of line nodes in superconducting gap in KFe₂As₂ [188]

is supported by now by numerous experiments. London penetration depth studies found close to T-linear dependence [84]. Small angle neutron scattering [244] found hexagonal vortex lattice, which the authors argued as an evidence for horizontal line nodes in the gap. Thermal conductivity studies reveal finite residual linear term in zero field, which rapidly increases with magnetic field [189]. Moreover, residual linear term was found to be independent of heat flow direction [204] and impurity scattering [204, 245], suggesting symmetry imposed vertical line nodes in the superconducting gap structure, similar to the d-wave superconducting state of the cuprates [19]. The specific heat of the samples revealed rapid rise of the residual term on Na doping, as expected in d-wave scenario [246]. Moreover, non-monotonic dependence of T_c on pressure was explained as an evidence of a phase transition in the superconducting state of KFe₂As₂ [247].

These observations, however, are disputed by recent ARPES [248] studies in pure samples, which both suggest extreme multi-band scenario with the existence of vertical line nodes on one sheet of the Fermi surface, and large full gap on the others. It is important to notice though that neither ARPES nor heat capacity measurements directly probe a response of the superconducting condensate, which allows alternative interpretation of the data as being surface in origin in the former case [247] and of magnetic origin in the latter [64].

In this section, we report systematic studies of the London penetration depth, its anisotropy and response to isoelectron substitution in KFe₂As₂. We show that response of the superfluid to pair-breaking non-magnetic disorder is consistent with symmetry imposed nodes in the superconducting gap and inconsistent with extreme multi-band scenario. Our observations may be suggestive that gaps in heat capacity and ARPES measurements are of non-superconducting origin.

Single crystals of KFe₂As₂ were grown using the KAs flux method as explained in detail in Ref. [221]. Small resistance contacts ($\sim 10\mu\Omega$) were tin-soldered and in-plane resistivity was measured using a four probe technique in *Quantum Design PPMS*. The

London penetration depth was measured with a TDR technique in ³He cryostat and dilution refrigerator with operation frequency of 14 MHz and 17 MHz, respectively. The sample was inserted into a 2 mm inner diameter copper coil that produced an rf excitation field with amplitude $H_{ac} \sim 20$ mOe, much smaller than typical H_{c1} . Measurements of the in-plane penetration depth, $\Delta \lambda_{ab}(T)$, were done with $H_{ac} \parallel c$ -axis, while with $H_{ac} \perp c$ we measured $\Delta \lambda_{c,mix}(T)$ that contains a linear combination of λ_{ab} and λ_c [102]. The shift of the resonant frequency (in cgs units), $\Delta f(T) = -G4\pi\chi(T)$, where $\chi(T)$ is the differential magnetic susceptibility, $G = f_0 V_s/2V_c(1-N)$ is a constant, N is the demagnetization factor, V_s is the sample volume and V_c is the coil volume. The constant G was determined from the full frequency change by physically pulling the sample out of the coil. With the characteristic sample size, R, $4\pi\chi = (\lambda/R) \tanh(R/\lambda) - 1$, from which $\Delta\lambda$ can be obtained [100, 102].

In the top panels of Fig. 5.5 we show temperature-dependent resistivity of pure K122, x=0, and of Na-doped sample with x=0.07. Zoom on the superconducting transition range in panel (b) shows a T^2 fit of the $\rho(T)$ curves used to evaluate residual resistivity of the samples. Based on measurements on array of 12 crystals from the same batch, we adopted that $\rho(300K)$ for pure KFe₂As₂ is $300\pm30~\mu\Omega$ cm. The resistivity value for Nadoped samples is indistinguishable from that of the pure material at high temperatures, so we adopted the same $\rho(300K)$. The $\rho(T)$ of two sets of samples are identical as well, except for increased residual resistivity and suppression of the superconducting transition temperature in x=0.07 samples. Extrapolated to T=0 the residual resistivities are $0.100\pm0.050~(x=0)$ and $1.7~\mu\Omega$ cm (x=0.07).

Scattering on non-magnetic alloy disorder in $K_{1-x}Na_xFe_2As_2$ introduces strong pair breaking effect, and strongly suppresses T_c . In Fig. 5.5 (c) we show T_c as a function of ρ_0 as determined in this study using $\rho=0$ criterion. For reference we show similar data obtained on Co doping in $K(Fe_{1-x}Co_x)_2As_2$, Ref. [245]. Despite the fact that Cosubstitution acts as electron-doping, while Na substitution is clearly isoelectronic, both

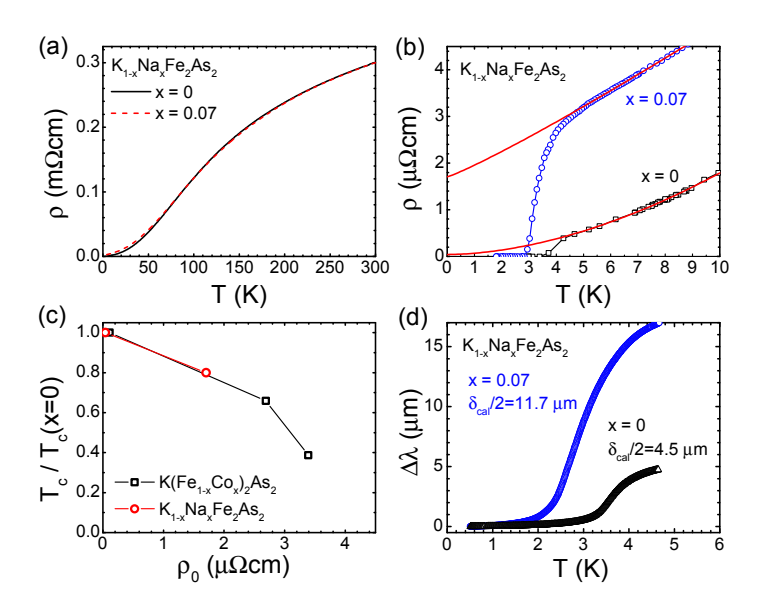


Figure 5.5 Electrical resistivity of $K_{1-x}Na_xFe_2As_2$ with x=0 and x=0.07 shown over full temperature range (panel a) and zoomed on the superconducting transition region (panel b). Lines in panel (b) show T^2 fit of the resistivity used for T=0 extrapolation. Bottom left panel shows superconducting T_c as a function of residual resistivity in isoelectron-substituted $K_{1-x}Na_xFe_2As_2$ (circles) in comparison with electron-doped $K(Fe_{1-x}Co_x)_2As_2$ (squares). Bottom right panel (d) shows penetration depth measurements in samples with x=0 and x=0.07 over the whole superconducting temperature range up to T_c . The difference in the $\Delta\lambda$ value above T_c in samples x=0 and x=0.07 reflects the difference in the normal state skin depth, proportional to the square root of electrical resistivity.

types of substitution introduce similar pair-breaking, suggestive that scattering, rather than electron count, plays primary role in T_c suppression.

In the bottom panel (d) of Fig. 5.5 we show temperature variation of London penetration depth in samples x=0 and x=0.07 over the temperature range from base temperature to above T_c . The data were taken using a TDR setup in a 3He cryostat down to T = 0.5 K, and in a dilution refrigerator in ~ 50 mK to ~ 3 K range. The superconducting transition is rather smooth in both x=0 and x=0.07 samples, which is similar to the results of previous radio frequency measurements on this compound [84]. The big width of the transition is caused not by the sample inhomogeneity, but small and strongly temperature-dependent normal state skin-depth. In samples of this low resistivity, the normal state skin effect makes significant contribution to the measured signal close to T_c . For resistivity value of 0.5 $\mu\Omega$ cm we can estimate skin depth at our experimental frequency of 14 MHz as $\delta \approx 8.6 \ \mu m$. Thus when the superconducting London penetration depth (which should diverge on approaching T_c on warming), becomes comparable to the normal state skin depth, the transition is no longer sharp and becomes of a broad crossover type. This contribution of the skin depth makes determination of T_c from purely TDR measurements on the same crystals very criterion dependent. In the following we rely on resistivity measurements on samples from the same batch for reference.

The variation of London penetration depth as a function of reduced temperature, $t = T/T_c$, provides information about the nodal structure of the superconducting gap. This statement is valid in a characteristic temperature range t < 0.3, for which the superconducting gap Δ can be considered as temperature-independent. For full gap superconductors, $\Delta\lambda(T)$ is exponential, as shown in Fig. 5.6(a) for optimally doped BaK122, x=0.40 [249]. For gap with line nodes, temperature variation shows power-law dependence $\Delta\lambda(T) = At^n$, where n depends on sample purity and takes values between n=1 (clean limit) to 2 (dirty limit). Same power-law dependence is expected for s_{\pm} , however with exponent n decreasing with pair-breaking scattering from n=4 (clean case,

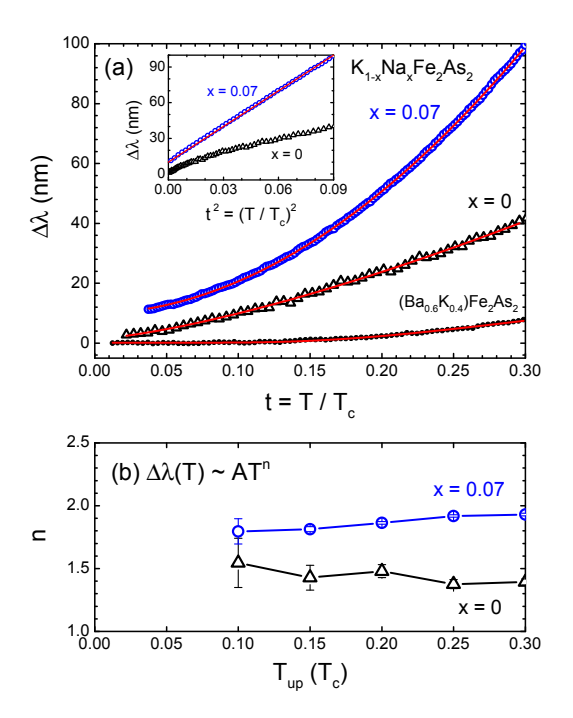


Figure 5.6 Top panel (a) shows $\Delta\lambda(T)$ for samples of $K_{1-x}Na_xFe_2As_2$ x=0 and x=0.07 in comparison with optimally doped $Ba_{1-y}K_yFe_2As_2$ y=0.4 [249]. The data are shown over characteristic temperature range up to $0.3T_c$, in which the gap of single-gap superconductors can be considered as constant. Solid lines show best fits of the data with power-law function $\Delta\lambda = a_0 + AT^2$ for x=0 and x=0.07, and exponential function $\sqrt{2\Delta_0/T}\exp(-\Delta_0/T)$ for BaK122. Data for sample x=0.07 were offset for clarity. Inset in top panel shows data for samples x=0 and x=0.07 plotted vs. square of the reduced temperature, $t=T/T_c$, straight line is guide for eyes. Bottom panel (b) shows dependence of the exponent n of the power-law fit, $\Delta\lambda = AT^n$, on the temperature T_{up} of the high-temperature end of the fitting range. The low-temperature end was always fixed at base temperature.

indistinguishable experimentally from exponential function) to about n=1.6 [90]. In top panel of Fig. 5.6 we show $\Delta\lambda$ vs t of KNa122 samples with x=0 and x=0.07. Inset shows the same data plotted as $\Delta\lambda(t^2)$. It is clear that the exponent n increases with doping and x=0.07 samples approaches the value n=2, both of the observations consistent with the superconducting gap with line nodes.

The data between the base temperature and t = 0.3 can be best fitted to the powerlaw function with (n = 1.39 and A = 200 nm) and (n = 1.93 and A = 911 nm) for K122 and KNa122, respectively. The observed n in KNa122 are in the range expected in a line-node scenario with moderate scattering. According to Hirschfeld-Goldenfeld's theory [82], $\Delta \lambda(T)$ can be characterized by a function, $T^2/(T + T^*)$ where T^* is the crossover temperature from T to T^2 at low temperatures. Our fit using this formula gives $T^* = 0.5T_c$, indicating a relatively clean case.

Alternatively, this crossover behavior can be due to multi-band effects in superconductivity. For multi-band superconductors the upper end of the characteristic $\Delta\lambda(T)$ dependence is determined by the smaller gap Δ_{min} , and shrinks proportional to Δ_{min}/Δ . Because the bounds of the interval of the characteristic behavior are unknown a priori, for quantitative analysis of the data we made power-law fitting with $\Delta\lambda(t) = a_0 + At^n$ over floating temperature interval. The low-temperature end of this interval was always kept fixed at base temperature, and the exponent of the power-law fit n was determined as a function the high-temperature end T_{up} . This dependence for KNa122 samples with x=0 and x=0.07 is shown in bottom panel of Fig. 5.6.

Additional information on the direction of nodes in the superconducting gap can be obtained from penetration depth anisotropy. In Fig. 5.7 we show T-variation of the frequency shift $\Delta f(T)$ in TDR measurements for orientation of ac magnetic field H along tetragonal c-axis and along ab-plane. Oscillating field H along c-axis induces supercurrent in the ab plane, so measured $\Delta\lambda(T)$ is proportional to the in-plane λ . For Happlied along the ab plane we measure the linear combination of both in-plane λ and inter-

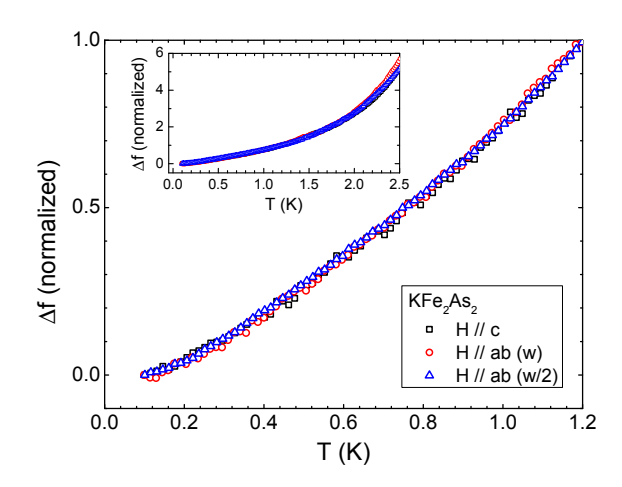


Figure 5.7 $\Delta f(T)$ in a sample of KFe₂As₂ positioned in a different way with respect to the ac- magnetic field H generated by the TDR inductor coil, in configuration $H \parallel c$ (in-plane penetration depth $\lambda_a b$, squares) and H along ab-plane (mixed penetration depth, circles). Triangles show the data for $H \parallel ab$, taken on a sample with the width (w) reduced two times compared to the initial measurements (circles), representing different mixture of λ_{ab} and λ_c . Inset shows the same data over a broader temperature range up to $0.76T_c$. Identical temperature dependence in all cases provides a clear evidence for the same functional form $\Delta\lambda(T)$ of both in-plane and inter-plane penetration depth.

plane λ_c , with relative contributions proportional to sample geometry. The combined response of the supercurrent is associated with the so-called $\Delta \lambda_{mixed}$, see Ref. [102] for details. For H along the ab-plane, the contribution from in-plane λ can be changed by reducing dimensions of the specimen, and, in principle, λ along c-axis can be extracted [102]. In our experiment, the width w of the sample perpendicular to H_{ac} was reduced to w/2 while maintaining thickness of the sample, so the contribution of in-plane λ into measured λ_{mix} has been reduced by half. We did not go into quantitative analysis of the data because cutting of small samples of soft KFe₂As₂ crystals always introduced cracks, affecting geometry in poorly controlled way. However, as can be seen in Fig. 5.7, three curves taken in sample with different geometry exhibit exactly the same temperature dependences over practically full superconducting temperature range as shown in the inset. The only way to explain this observation is to assume anisotropic superconducting gap structure with vertical line nodes.

A further insight into the structure of the superconducting gap in KFe₂As₂ can be obtained through the analysis of the temperature-dependent superfluid density, $\rho_s(T) = \lambda^2(0)/\lambda^2(T)$. This quantity can be studied over the full superconducting temperature range, and compared with various models. To calculate superfluid density we have to know $\lambda(0)$, which does not come from standard TDR experiment. For sample with x=0 we calculated $\rho_s(T)$ using $\lambda(0) = 0.26 \ \mu \text{m}$ following Ref. [84]. For sample with x=0.07 we estimated $\lambda(0) = 1 \ \mu \text{m}$ using Homes scaling law based on resistivity and T_c data [252, 253] The resulting $\rho_s(T)$ are shown in Fig. 5.8 using normalized scale $\rho_s/\rho_s(0)$ vs T/T_c . The low-temperature part of $\rho_s(T)$ for both pure and doped samples are shown

¹The slope of the experimental superfluid density at T_c , $\rho'_s(T/T_c)|_{T_c} \equiv \rho'_s(1)$, calculated in KFe₂As₂ with $\lambda(0) = 260$ nm [84], was compared to the Rutgers formula estimate. Using literature values of $\Delta C = 164$ mJ/mol-K [250] and $H'_{c2}(1) = -0.55$ T/K [250], we obtained $\rho'_s(1) = -2.5$, using another value of $\Delta C = 228$ mJ/mol-K [251] with the same $H'_{c2}(1)$, we obtained $\rho'_s(1) = -3.7$. Both estimates are significantly higher than the experimental value $|\rho'_s(1)| \sim 1.5$. The origin of this discrepancy can be partially caused by strong curvature of ρ_s near T_c caused by comparable London penetration depth and normal skindepth. Another possibility is non-superconducting contribution to the magnitude of the specific heat jump [64], a problem similar to that found in application of the Rutgers formula for optimally doped Ba_{1-x}K_xFe₂As₂ (see section 4.3). Additional complication may come from the proximity to a state with different gap symmetry [247], which can lead to over-estimate of $\rho'_s(1)$.

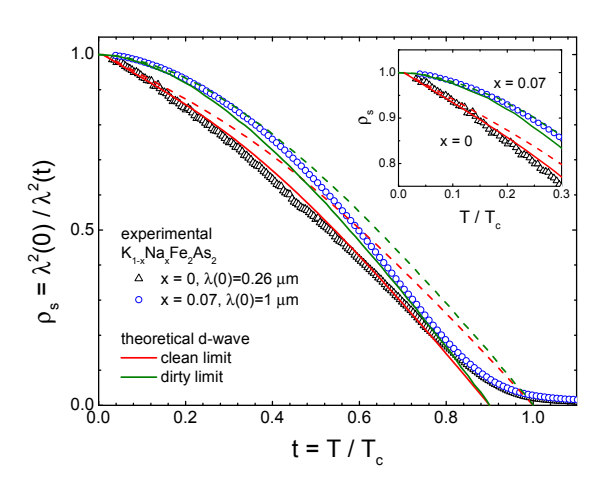


Figure 5.8 Temperature-dependent superfluid density, $\rho_s = \lambda^2(0)/\lambda^2(T)$, in samples of $K_{1-x}Na_xFe_2As_2$ calculated from $\Delta\lambda(T)$ data of Fig. 5.6 using $\lambda(0) = 260$ nm for x=0, Ref. [84], and $\lambda(0) = 1$ μ m for x=0.07. Data are shown on normalized scale as $\rho_s/\rho_s(0)$) vs T/T_c . Superconducting T_c was determined from resistivity measurements using zero resistivity criterion. Red and green lines show theoretically expected superfluid density $\rho(T)$ in a clean and dirty d-wave superconductor. The anomalously slow variation of the superfluid density at T_c is caused by the interplay of London penetration depth and of the skin depth close to T_c , the data for temperatures below $T_c/2$, when the effect of skin depth becomes negligible, are in good agreement with clean (x=0) and dirty (x=0.07) d-wave cases (see zoom in the inset).

in the inset of Fig. 5.12.

For reference we show expected temperature dependent superfluid density in clean and dirty d-wave cases, which are representative of all superconductors with linear line nodes. Because of uncertainty of T_c determination in the same experiment and strong interplay of London penetration depth with normal state skin-depth in these very conductive materials, the data are not very well defined close to T_c . The flat $\rho_s(T)$ at T_c is clearly an artifact of this interplay, and we neglect it in comparison with theory. In pure material with skin depth 4.5 μ m and $\lambda(0)=0.26$ μ m, the London penetration depth becomes much smaller than skin-depth at temperatures of order of $0.8T_c$. Below this temperature $\rho_s(T)$ indeed follows expectations for a d-wave superconductor, though with somewhat suppressed T_c . In Na-doped sample the dependence also follows expectations for dirty d-wave superconductors.

When analyzing $\rho_s(T)$, we should notice that deviation from d-wave calculations do not leave room for any full gap contribution to superfluid density. If it was present, at a level more that 0.1 of the total ρ_s , it would result in significant exceeding of $\rho_s(T)$ over the curve for a d-wave case. Based on this comparison we can disregard any contributions from full gap-superfluid in both clean x=0 and x=0.07 samples with the accuracy of less than 0.1 of total superfluid density.

Along with the power-law behavior of $\Delta\lambda(T) \sim T^{1.4}$ at low temperatures, our observations leave very little room for non-nodal contribution to the superfluid density of KFe₂As₂. The response of the superfluid in both clean and dirty samples is not only consistent with the existence of line nodes in the superconducting gap, but does not leave much room for any contribution from Fermi surfaces with full gap, as suggested by ARPES [248]. Considering significant anomalies in the normal state of KFe₂As₂, resembling thous of heavy fermion materials, we speculate that specific heat jump in KFe₂As₂ may contain magnetic contribution, which is a plausible scenario for CeCoIn₅. Whether this is the case remains an interesting question for future studies.

In conclusion, our resistivity and TDR penetration depth studies on high quality pure and isoelectron Na substituted KFe₂As₂ find the behavior which is consistent with expectation with line nodes in the superconducting gap of the material. Analysis of the superfluid density shows that the contribution of superfluid density from full-gap Fermi surfaces is less than 0.1 of total superfluid density. These data can be viewed as strong support of nodal superconducting gap on all Fermi surfaces contributing to superconductivity.

5.2 Irradiation effect on London penetration depth in

Ba(Fe_{1-x}
$$T_x$$
)₂As₂ (T =Co, Ni) and Ba_{1-x} K_x Fe₂As₂ superconductors

The mechanism of superconductivity in Fe-based pnictides [25] has not yet been established despite extensive experimental [254] and theoretical [190, 38] efforts. While the pairing "glue" is widely discussed, it seems that the pairing between bands with different signs of the order parameter explains the majority of the observations [57]. In particular, the Anderson theorem does not work for this state and even non-magnetic impurity scattering is pair-breaking [190, 89, 157]. This is especially important, since most Fe-based compounds become superconducting only upon substantial doping, which also leads to an intrinsic disorder making the analysis of the experimental data difficult.

One way to test the pairing state is to deliberately introduce defects that do not contribute extra charge but rather only induce additional scattering. In earlier studies, especially in the cuprates, various ways of controlling the scattering rate have been suggested and the effects have been examined by using transport [255] and magnetic [256] measurements. Irradiation with heavy ions, which has been used to produce efficient pinning centers, also results in the enhanced rates evident from the significant increase of normal state resistivity [257, 258] as well as suppression of T_c .

The temperature dependence of the penetration depth is a powerful tool for examining the order parameter in iron-based superconductors. At low temperatures, an exponentially activated dependence implies a finite, minimum gap magnitude in the density of states vs. energy near the Fermi level. The behavior at higher temperatures can signal gaps of different magnitude. Currently, one of the most plausible pairing scenarios in iron - based superconductors is so-called s_{\pm} state proposed some time ago [57, 259] but proof of a sign change remains a challenge. Several authors [89, 90] have shown that impurities alter the temperature dependence of many thermodynamic quantities in a manner that is sensitive to the relative sign. In particular, for the s_{\pm} state one expects to move from exponentially activated to a power law temperature dependence with increasing impurity concentration. As far as suppression of T_c is concerned, there are several predictions and several experiments that seem to be controversial. Originally a very fast rate of suppression was predicted [260], which however was later revised [261, 245].

Isolating the role of impurities is difficult since they may also change the carrier concentration which may in turn change the pairing state. Columnar defects produced by heavy ion irradiation offer an alternative. Columns do not ostensibly change the carrier concentration or add magnetic scattering centers and their density may be varied by controlled amounts. Since columns are also effective pinning centers [262, 263], their effect on the superconducting properties is important to understand.

5.2.1 London penetration depth in $Ba(Fe_{1-x}T_x)_2As_2$ (T=Co, Ni) superconductors irradiated with heavy ions

In this section, we discuss the in-plane London penetration depth measured by using the tunnel diode resonator (TDR) technique in single crystals of optimally Co-and Ni-doped BaFe₂As₂ superconductors irradiated with 1.4 GeV ²⁰⁸Pb⁵⁶⁺ ions at different fluences. While the phase diagrams in terms of T_c vs. electron count are practically identical for the two systems [264], the atomic percentage of Ni required to achieve the

same T_c is one half compared to the Co-doped samples. We find that both compositions have shown similar evolution of $\Delta\lambda(T)$ upon irradiation. The penetration depth follows the power-law behavior at low temperatures, $\Delta\lambda(T) \propto AT^n$ with 2.2 < n < 2.8. The pre-factor, A, increases and the exponent, n, decreases upon irradiation dose. The T_c is suppressed by irradiation while the transition width remains nearly same. These findings are supported by theoretical analysis that provides the most convincing case for the nodeless s_{\pm} state.

Single crystals of Ba(Fe_{1-x}T_x)₂As₂ (T=Co, Ni denoted FeCo122 and FeNi122, respectively) were grown out of FeAs flux using a high temperature solution growth technique [264, 222]. X-ray diffraction, resistivity, magnetization, and wavelength dispersive spectroscopy (WDS) elemental analysis have all shown good quality single crystals at the optimal dopings with a small variation of the dopant concentration over the sample and sharp superconducting transitions, T_c = 22.5 K for FeCo122 and 18.9 K for FeNi122 [264, 222].

To examine the effect of irradiation, $\sim 2 \times 0.5 \times 0.02 - 0.05$ mm³ single crystals were selected and then cut into several pieces preserving the width and the thickness. Hence, the results reported here compare sets of samples, where the samples in each set are parts of the same original larger crystal. Several such sets were prepared and a reference piece was kept unirradiated from each set. The thickness was chosen in the range of $\sim 20 - 50 \mu \text{m}$ to be smaller than the penetration depth of the radiation particle, $60 - 70 \mu \text{m}$. Irradiation with 1.4 GeV ²⁰⁸Pb⁵⁶⁺ ions was performed at the Argonne Tandem Linear Accelerator System (ATLAS) with an ion flux of $\sim 5 \times 10^{11}$ ions·s⁻¹·m⁻². The actual total dose was recorded in each run. The density of defects (d) created by the irradiation is usually expressed in terms of the ma T_c hing field, $B_{\phi} = \Phi_0 d$, which is obtained assuming one flux quanta, $\Phi_0 \approx 2.07 \times 10^{-7}$ G·cm² per ion track. Here we studied samples with $B_{\phi} = 0.5$, 1.0, and 2.0 T corresponding to $d = 2.4 \times 10^{10}$ cm⁻², 4.8×10^{10} cm⁻² and 9.7×10^{10} cm⁻². The same samples were studied by magneto-optical

imaging, and strong Meissner screening and large uniform enhancement of pinning have shown that the irradiation produced uniformly distributed defects [265].

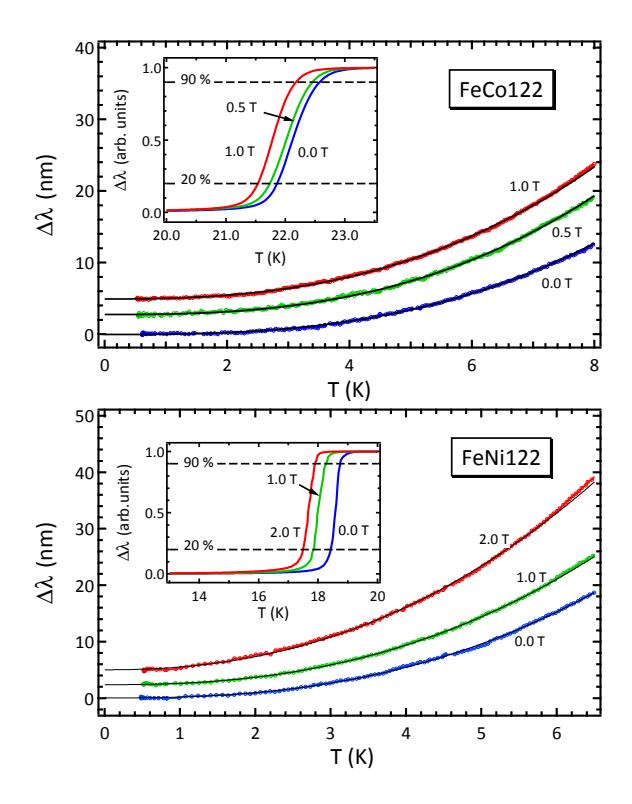


Figure 5.9 Variation of the in-plane London penetration depth, $\Delta\lambda(T)$, for irradiated FeCo122 (top panel) and FeNi122 (bottom panel). The low-temperature variations are shown in the main frame of each panel along with the best power-law fits. The curves are offset vertically for clarity. The variations in the vicinity of T_c are shown in the insets of each panel.

Figure 5.9 shows $\Delta\lambda(T)$ for FeCo122 (top panel) and FeNi122 (bottom panel). The low-temperature region up to $\approx T_c/3$ is shown in the main frame of each panel. Vertical offsets were applied for clarity. The normalized penetration depths in the vicinity of T_c are shown in the inset of each panel to highlight the suppression of T_c as the radiation dose increases. Whereas T_c is clearly suppressed, the transition width remains nearly the same (see Fig. 5.11 below). All samples exhibit a power-law variation of $\Delta\lambda(T) \propto T^n$ with 2.5 < n < 2.8 up to $T_c/3$, while the exponential fitting failed in all cases. The best fitting curves are shown by solid lines in Fig. 5.9. We note that the

set of FeCo122 samples used in this study exhibits higher exponents, n, compared to our previous works [85, 140]. This variation of n previously observed in other studies [86, 195, 140] is likely due to disorder variations, as we clearly demonstrate in this work. Consequently, it is important to conduct the comparison on the same sample. Magneto-optical characterization showed homogeneous superconducting response, and the widths of the superconducting transitions were much smaller than the absolute shift due to irradiation [265]. Therefore, it is very likely that the reported here effects are caused by the enhanced scattering induced by the heavy-ion bombardment.

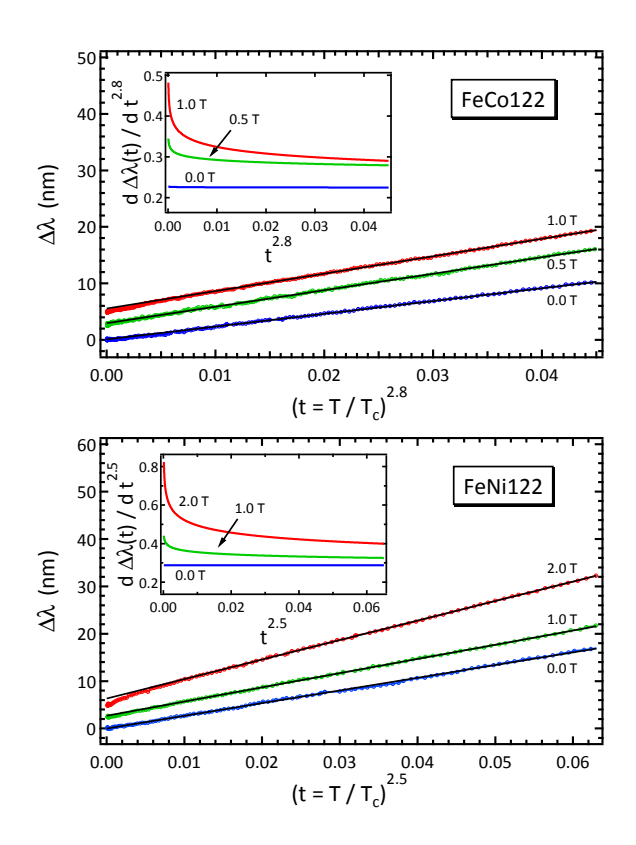


Figure 5.10 Detailed comparison of the functional form of $\Delta\lambda(T)$ for irradiated FeCo122 and FeNi122. In the main panels, $\Delta\lambda(T)$ is plotted vs. $(t = T/T_c)^{n_0}$ with the exponents n taken from the best fits of unirradiated samples: $n_0 = 2.8$ and 2.5 for FeCo122 and FeNi122, respectively (see Fig.5.9). Apparently, irradiation causes low-temperature deviations, which are better seen in the derivatives, $d\Delta\lambda(t)/dt^{n_0}$ plotted in the insets.

To further analyze the power-law behavior and its variation with irradiation, we

plot $\Delta\lambda$ as a function of $(t = T/T_c)^{n_0}$ in Fig. 5.10, where the n_0 values for FeCo122 and FeNi122 were chosen from the best power-law fits of the unirradiated samples (see Fig. 5.11). While the data for unirradiated samples appear as almost perfect straight lines showing robust power-law behavior, the curves for irradiated samples show downturns at low temperatures indicating smaller exponents. In order to emphasize this observation and disentangle the change from the pre-factors, the derivatives, $d\Delta\lambda(t)/dt^{n_0}$, are shown in the inset of each frame of Fig. 5.10.

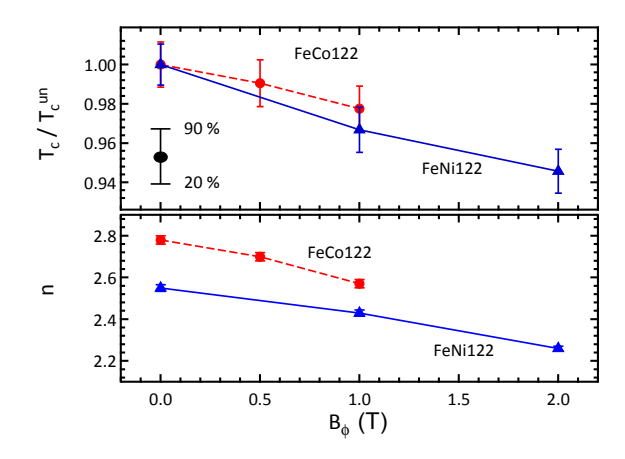


Figure 5.11 Top panel: The evolution of T_c and the width of the transition with irradiation. The vertical bars correspond to temperatures where diamagnetic response changed from 90% (onset) to 20% (end of the transition), see insets in Fig. 5.9. Lower panel: exponent n vs. B_{ϕ} .

The variations of T_c and n upon irradiation are illustrated in Fig. 5.11. Dashed lines and circles show FeCo122, solid lines and triangles show FeNi122. The upper panel shows variation of T_c and width of the transition estimated by taking 90% and 20% cuts of the transition curves (see insets in Fig. 5.9). Since B_{ϕ} is directly proportional to the area density of the ions, d, we can say that T_c decreases roughly linearly with d. The same trend is evident for the exponent n shown in the lower panel of Fig. 5.11. The fitting pre-factor A increases slightly upon increase of irradiation dose, but remains smaller than measured previously in unirradiated samples [85, 86, 107]. Whereas pre-factor may vary depending on the model for the gap, the exponent behaves more systematically.

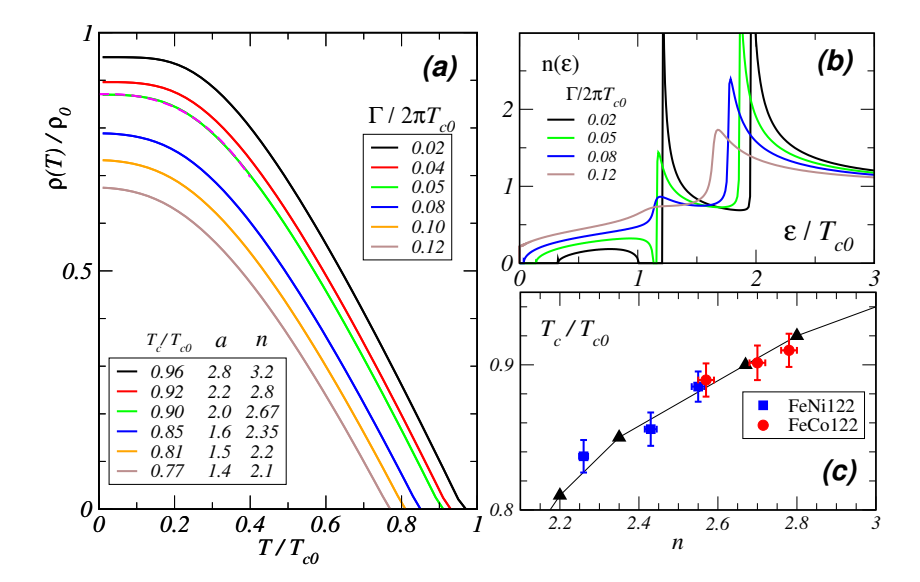


Figure 5.12 (a) Superfluid density, and (b) the density of states $n(\varepsilon) = N(\varepsilon)/N_f$ computed for s_{\pm} state with sign-changing isotropic gaps, and impurity parameters between the Born and unitary limits, with strong interband scattering. The dashed line in (a) is an example of power-law fit $\rho(T)/\rho_0 = \rho(0)/\rho_0 - a(T/T_{c0})^n$ for $0 < T < 0.4\,T_{c0}$; best fitting parameters for a set of $\Gamma = n_{imp}/\pi N_f$ are listed in the table. (b) As impurity concentration ($\sim \Gamma$) increases, the band of mid-gap states approaches Fermi level and the power n is reduced. (c) T_c vs. power n, from the theoretical model (triangles) and experiment (squares and circles).

Our experimental results fit comfortably within the hypothesis of an s_{\pm} superconductivity with two isotropic gaps. The superfluid density in linear response is,

$$\rho(T) = \sum_{i=1,2} \pi T \sum_{\varepsilon_m} N_{f,i} \int_{FS_i} d\hat{\mathbf{p}} [\mathbf{v}_{f,i} \otimes \mathbf{v}_{f,i}]_{xx} \frac{\tilde{\Delta}_i^2}{(\tilde{\varepsilon}_m^2 + \tilde{\Delta}_i^2)^{3/2}}$$
(5.1)

where we sum over the contributions from the electron and hole bands; $\mathbf{v}_{f,i}$ and $N_{f,i}$ are the Fermi velocity and density of states in these bands, taken equal for the calculations. Two order parameters $\Delta_{1,2}$ are computed self-consistently together with the t-matrix treatment of impurity effects, that renormalize the Matsubara energies $\tilde{\varepsilon}_m = \varepsilon_m - \Sigma_{imp,i}$ and the gaps $\tilde{\Delta}_i = \Delta_i + \Delta_{imp,i}$ [266]. Impurities are characterized by the strength of the potential for scattering within each band, $v_{11}(=v_{22})$, giving via the phase shift $\delta = \tan^{-1}(\pi N_f v_{11})$, the ratio of potentials for inter-band and intra-band scattering rates, $\delta v = v_{12}/v_{11}$, and impurity scattering rate $\Gamma = n_{imp}/\pi N_f$.

The essential results are presented in Fig. 5.12 while the full calculations will be published elsewhere (Appendix Vorontsov2010). The best agreement with the experiment is obtained for two isotropic gaps, $\Delta_2 \approx -0.6\Delta_1$, strong inter-band scattering $\delta v = 0.9$ and phase shift $\delta = 60^{\circ}$ between the Born ($\delta \rightarrow 0$) and unitary limits ($\delta \rightarrow 90^{\circ}$). Calculated $\rho(T)$ was fitted to the power law, $\rho(T)/\rho_0 \approx \rho(0)/\rho_0 - a \left(T/T_c^{\rm un}\right)^n$, which is directly related to the penetration depth, $\Delta \lambda(T)/\lambda_0 \approx a'(T/T_c)^n$, with ρ_0 and λ_0 being the T=0 superfluid density and penetration depth in the clean system, and $a' = (a/2)[T_c/T_{c0}]^n[\rho_0/\rho(0)]^{3/2}$. We find that with increase in Γ the power n decreases from $n \gtrsim 3$ to $n \approx 2$ (see Fig. 5.12(a)), in a perfect agreement with experiment. The values of n depend sensitively on the structure of the low-energy density of states, which is shown in Fig. 5.12(b). The intermediate strength of scatterers is important for creation of a small band of mid-gap states separated from the continuum. Such band does not appear in either Born or unitary limit, which was probably the reason for power laws of $n \lesssim 2$ [90]. As the disorder increased, these states close the gap in the spectrum, while slowly increasing in magnitude, driving the low-temperature power-law dependence from exponential like, n > 3, to $n \approx 2$. The prefactor a', on the other hand, slightly decreases with disorder, opposite to experimental increase of about 10% in $A' = AT_c^n$.

However, this trend can be reversed by considering different ratios of the gaps on two FSs and different impurity parameters.

Finally, in Fig. 5.12(c) we show the central result of our study: the suppression of T_c as a function of n. Note that these two quantities are obtained independently of each other. Assuming that the unirradiated samples have some disorder due to doping, and scaling their transition temperatures to lie on the theoretical curve, one finds that the $T_c(B_\phi)$ of the irradiated samples also fall on this curve. This comparison tacitly implies that the doping- and the radiation-induced disorders are of the same type, - assumption that is left for future investigations.

5.2.2 London penetration depth in $Ba_{1-x}K_xFe_2As_2$ irradiated with heavy ion

In this section we discuss penetration depth measurements on single crystals of Ba_{0.6}K_{0.4}Fe₂As₂, a 122 superconductor that is roughly the hole-doped counterpart to $Ba(Fe_{1-x}Co_x)_2As_2$ but with a crucial difference. Substitution of Co for Fe leads to considerably higher scattering rates in $Ba(Fe_{1-x}Co_x)_2As_2$ [157] than in $Ba_{1-x}K_xFe_2As_2$ [195, 194], making the latter material a better candidate for tests of pairing symmetry. In fact, recent thermal conductivity measurements in $Ba_{1-x}K_xFe_2As_2$ show a transition from nodeless to nodal pairing state upon doping towards pure KFe₂As₂ [204]. By studying both pristine and irradiated samples taken from the same crystal we isolate the effect of columnar defects on both the penetration depth and T_c as first carried out on $Ba(Fe_{1-x}Co_x)_2As_2$ and $Ba(Fe_{1-x}Ni_x)_2As_2$ where a good agreement with s_{\pm} pairing was found [201]. Remarkably, in the case of $Ba_{1-x}K_xFe_2As_2$ heavy ion irradiation does not change T_c at all, even with a column to column spacing of a few coherence lengths. However, very dense columnar defects do cause the penetration depth to acquire a T^2 power law. Our results could imply that pairing in $Ba_{1-x}K_xFe_2As_2$ is mostly determined by the in-band channels and therefore it is unclear whether it is s_{++} or s_{\pm} , because the latter is stable in the opposite regime [261, 245]. We note that London penetration depth remains exponential at low temperatures even in the dirty limit of conventional isotropic s-wave superconductor [102].

Measurements were performed on two sets of (nominally) optimally doped single crystal Ba_{0.6}K_{0.4}Fe₂As₂ [267]. Single crystals of Ba_{1-x}K_xFe₂As₂ were grown using high temperature FeAs flux method [196]. Irradiation with 1.4 GeV ²⁰⁸Pb ions was performed at the Argonne Tandem Linear Accelerator. Heavy ions formed tracks along the c-axis with an average stopping distance of 60-70 μ m, larger than the thickness of the crystals. For the first set, a single crystal with $T_c = 39$ K was cut into several smaller segments. One segment was left unirradiated ($B_{\phi} = 0$) while the other segments had irradiation doses corresponding to $B_{\phi} = 2$ T and 4 T. The penetration depth was measured at the

Ames Laboratory. Two other samples were taken from a single crystal with $T_c = 36.8$ K. One kept unirradiated while the second had a column density of $B_{\phi} = 21$ T. Changes in the penetration depth with temperature were measured at the University of Illinois with the tunnel diode resonator method described in several previous publications [101].

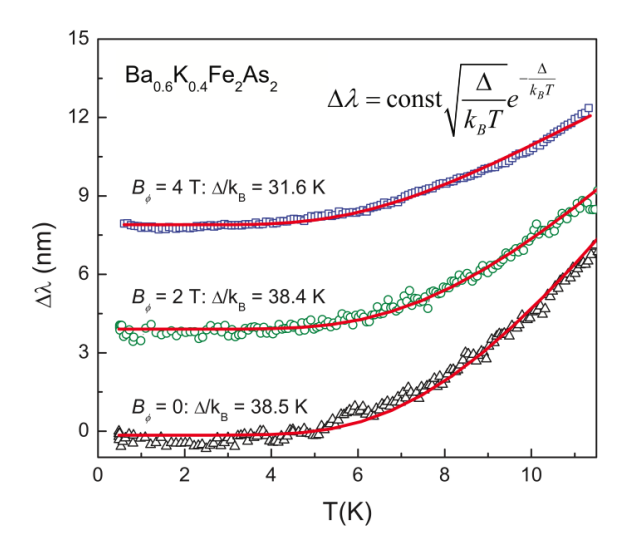


Figure 5.13 Change in penetration depth for the first set of three samples ($T_c = 39 \text{ K}$). For columnar defect densities of $B_{\phi} = 0$, 2, 4 T. Fits to BCS temperature dependence are shown as solid curves. Ref. [249]

Figure 5.13 shows the penetration depth in the low temperature region $(T/T_c < 0.32)$ for the first set of samples $(T_c = 39 \text{ K})$. Over the temperature range shown the data for each irradiation level was fit to a single gap BCS form.² The gap values were $\Delta_0/k_BT_c = 0.99$ $(B_\phi = 0)$, 0.99 $(B_\phi = 2 \text{ T})$ and 0.81 $(B_\phi = 4 \text{ T})$. In each case the BCS expression provided a superior fit to a power law. For comparison, STM measurements give $\Delta_0/k_BT_c = 1.1$ for the minimum gap energy [267] and ellipsometry experiments have also reported $\Delta_0/k_BT_c = 1.1$ [268]. Figure 5.14 shows similar data for the second sample group $(T_c = 36.8 \text{ K})$. Data for the unirradiated sample was best fit to a BCS form with $\Delta_0/k_BT_c = 0.97$. The lower panel of Fig. 5.14 shows data for the heavily irradiated $(B_\phi = 21 \text{ T})$ sample. In this case a T^2 power law provided a clearly superior

 $^{^2\}Delta\lambda(T)=\lambda(0)\sqrt{\pi\Delta_0/2k_BT}\exp(-\Delta_0/k_BT)$ where $\lambda(0)$ and Δ_0 are set as free fitting parameters.

fit to the BCS form. There was no evidence of a low temperature upturn in frequency that can arise from magnetic impurities. Therefore any scattering from the columnar defects should be regarded as nonmagnetic. Figure 5.15 shows data in the vicinity of T_c . For the first set (lower panel) the midpoint transition temperature of $T_c = 39$ K was unaffected by irradiation for all three matching fields. This data should be contrasted with a systematic suppression of T_c for similar irradiation levels in Ba(Fe_{1-x}T_x)₂As₂ (T = Co, Ni) [201]. For the second set of samples (upper panel) the midpoint transition of $T_c = 36.8$ K was the same for both unirradiated and irradiated samples. It should be noted that the highest irradiation level of $B_{\phi} = 21$ T corresponds to an average column separation of 10 nm. TEM images show that the columns themselves have a mean diameter of 5 nm so the superfluid is confined to regions of order 5 nm or less, i.e., roughly 2 coherence lengths. In such a confined geometry one might expect a suppression of the order parameter, though we have no evidence for it.

The data presented here appear difficult to reconcile. The evolution from BCS-like or at least T^n with n > 2 temperature dependence toward T^2 with increased scattering has been reported in several different iron-based superconductors [102]. It is predicted to occur with an s_{\pm} order parameter but not for an s_{++} pairing state [89, 90, 261, 245]. Indeed, no such evolution has been reported in MgB₂, currently our best candidate for s_{++} pairing. However, the insensitivity of T_c to defect density is an extreme example of a trend throughout the 122 family of superconductors; namely that T_c sensitivity to impurity scattering is not universal and depends on details of the pairing interactions as well as bandstructure [261, 245, 259]. If defects produce purely intraband scattering then one expects Andersons theorem to hold and no T_c suppression is expected in either an s_{++} or an s_{\pm} state. Nonmagnetic interband scattering does suppress T_c in a multigap superconductor, the degree to which depends upon the band to band variation of the energy gap [269, 270]. Owing to the factor of two ratio of energy gaps, MgB₂ might be expected to show strong T_c suppression but it does not [271]. Peculiarities of the MgB₂

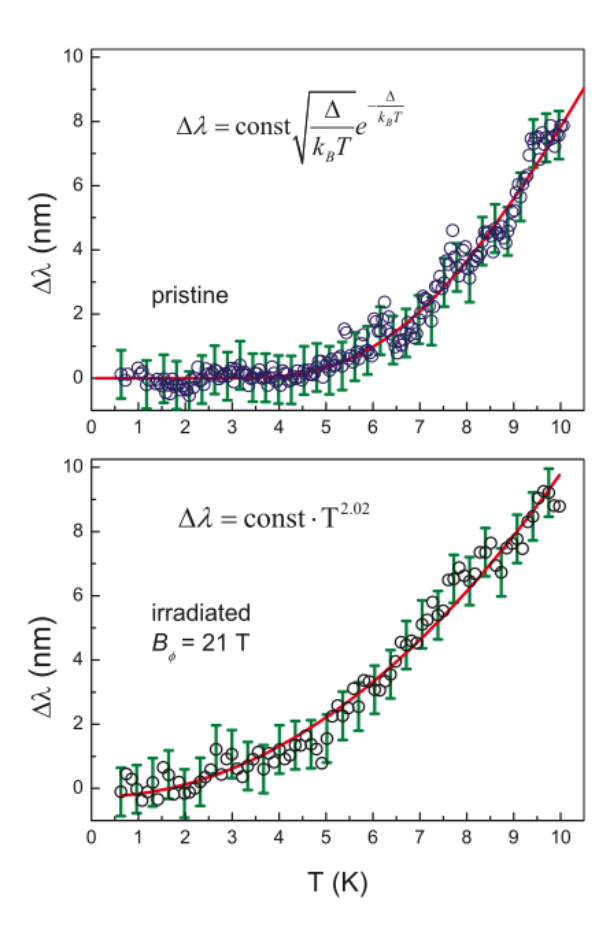


Figure 5.14 Change in penetration depth for the second set of samples ($T_c = 36.8 \text{ K}$). Upper panel: data fro unirradiated sample with BCS-like fit. Lower panel: Sample with $B_{\phi} = 21 \text{ T}$ matching field showing quadratic power law fit. Ref. [249]

electronic structure apparently strongly reduce interband scattering [269, 270] and T_c suppression is instead very weak.

In the experiment described in the previous section, penetration depth in irradiated samples of Ba(Fe_{1-x}T_x)₂As₂ (T = Co, Ni) [201] showed an evolution from T^3 to T^2 power law with increasing irradiation level, consistent with s_{\pm} pairing. The change in power law with increased defect density was accompanied by a continuous decrease in T_c , also explained within an s_{\pm} picture and demonstrating that columnar defects can produce interband scattering. Due to the substitution of Co or Ni for Fe, the electron-doped 122 superconductors have higher scattering rates than Ba_{0.6}K_{0.4}Fe₂As₂ and an exponential

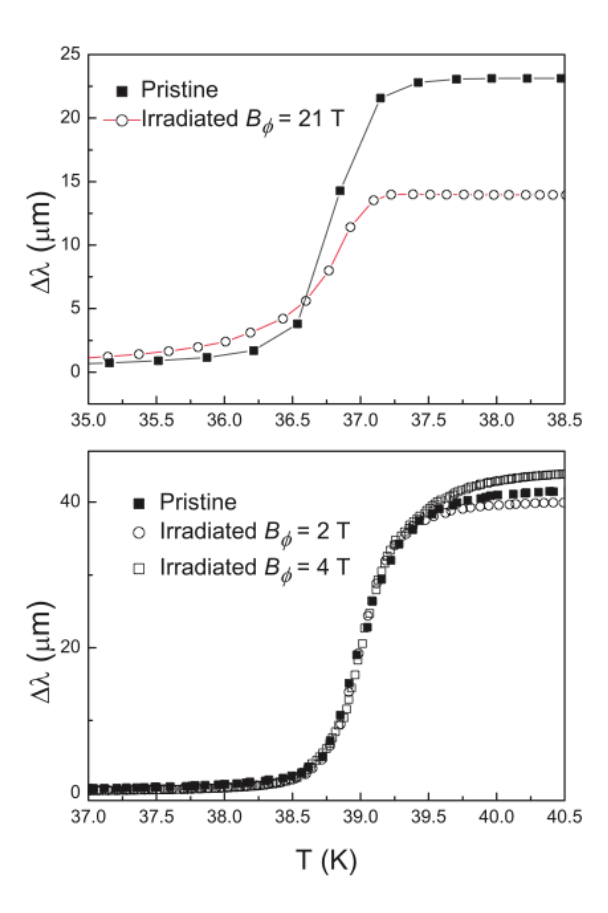


Figure 5.15 Change in penetration depth near T_c for both sets of samples and different irradiation levels. Ref. [249]

temperature dependence of the penetration depth was not observed. Indeed, Charnunkha et. al. found that differences in infrared reflectance data between Ba(Fe_{1-x}Co_x)₂As₂ and Ba_{0.6}K_{0.4}Fe₂As₂ could be accounted for entirely by the disparity in scattering rates, assuming that both materials pair in an s_{\pm} state [268].

Our data are consistent with recent models [261, 245] that argue that the sign of the interband pairing interaction is crucial. In the pure superconductor both repulsive and attractive interband coupling can lead to an s_{\pm} state. However, the difference is revealed upon addition of nonmagnetic impurities. For repulsive interactions T_c suppression follows an Abrikosov-Gor'kov [11] scenario in which a generalized scattering rate of order $\hbar\Gamma \sim T_{c0}$ drives T_c to zero, all the while maintaining an s_{\pm} symmetry. For attractive

interband coupling, T_c suppression by impurities is much weaker but as the scattering rate increases the gap structure eventually crosses over from s_{\pm} to s_{++} . The penetration depth in the pure state is exponentially activated, as we observe, and with increased scattering it approaches the T-quadratic dependence that we also observe. For strong enough scattering they predict the formation of an s_{++} state, for which activated behavior should once again be observed. This scenario is consistent with our data, suggesting attractive interband interactions and a scattering rate even at the highest irradiation level that is not sufficient to induce s_{++} superconductivity. An alternative picture invokes a competition between superconducting and spin density wave (SDW) order [272]. For doping somewhat below optimal, superconductivity in $Ba_{1-x}K_xFe_2As_2$ coexists with a spin density wave [267]. Disorder generally suppresses the SDW transition, a process that may enhance s_{\pm} superconductivity despite interband scattering. Moreover, SDW cannot coexist with s_{++} superconductivity [203], so the s_{\pm} pairing is likely. The behavior of T_c therefore depends on the level of doping as well as the strength and character of the scattering. This model could also reconcile the appearance of a \mathbb{T}^2 power law with negligible change in T_c . However, there is no evidence within our measurements for the coexistence of an SDW with the superconducting phase so an alternative probe would be needed to test this model.

Our results could imply that pairing in $Ba_{1-x}K_xFe_2As_2$ is mostly determined by the in-band channels and therefore it is unclear whether it is s_{\pm} . It is also possible that for some reason columnar defect in BaK122 mostly affect the intraband scattering.

5.3 Summary

Temperature variation of the London penetration depth was measured in two stoichiometric superconductors: LiFeAs and KFe₂As₂. Using known from the literature values of $\lambda(0)$, we calculated a superfluid density and found fully gapped and line nodal supercon-

ducting states in LiFeAs and KFe₂As₂, respectively. Variation of superfluid density in the whole temperature range in LiFeAs could be well described in two s-wave gap model in clean limit. On the other hand, superfluid density in KFe₂As₂ is consistent with the presence of line nodes in the gap. Na-doping into KFe₂As₂ change the low-temperature $\Delta\lambda$ to T-quadratic which is consistent with symmetry imposed d-wave state with vertical line nodes. These observations are in line with studies of thermal conductivity (which is not as sensitive to scattering) in LiFeAs [187] and KFe₂As₂ [204]. Considering similar full-gap superconducting state in optimally doped BaK122 [273], overall, this establishes a common trend for all Fe-based superconductors to have a superconducting gap that evolves from full to nodal when moving towards the edge of the superconducting dome.

The effect of heavy ion irradiation on $\lambda(T)$ was studied in optimally electron-doped Ba(Fe,T)₂As₂ (T=Co, Ni). We found that the disorder leads to suppression of T_c and the reduction of the power-law exponent 2 < n < 3. This is naturally explained in terms of the isotropic extended s_{\pm} -wave state [190, 38] with pair-breaking interband scattering [190, 157, 202]. Taken together with reports of fully gapped states from thermal conductivity [77] and angle resolved photoemission spectroscopy [274], our results present a convincing case in favor of the extended s_{\pm} pairing symmetry with nodeless order parameter in the optimally doped 122 system.

On the other hand, in optimally hole-doped (Ba,K)Fe₂As₂, T_c remains the same in heavy ion irradiated samples with B_{ϕ} at least up to 21 T in which the inter columnar distance is comparable to the coherence length. Our results imply that pairing in Ba_{1-x}K_xFe₂As₂ is mostly determined by the in-band channel and therefore it can be different from s_{\pm} pairing. Alternative scenario is that columnar defect in (Ba,K)Fe₂As₂ predominantly affect inter-band scattering.

CHAPTER 6. CONCLUSIONS

In this thesis, the low temperature London penetration depth and superfluid density were studied in several families of the Fe-based, and related, superconductors. The penetration depth data presented in this thesis were measured by using a tunnel diode resonator technique in a 3 He cryostat and extended to lower temperatures (~ 50 mK) using a dilution refrigerator with technique developed in the course of thesis.

For the analysis of superconducting gap structure we measured and characterized the low temperature dependence of London penetration depth and temperature dependent superfluid density, calculated from measured penetration depth and separately measured $\lambda(0)$. Measurements of $\lambda(0)$ were performed using the Al-coating technique, and original contribution of this thesis is use of thermodynamic Rutgers formula for $\lambda(0)$ determination. We were able to modify original Rutgers relation so that it allows quantitative analysis of the superfluid density from knowledge of other thermodynamic quantities such as heat capacity jump and slope of the upper critical field.

Extension of measurements down to 50 mK using a dilution refrigerator enabled us to study materials with low T_c . We found that all related low T_c superconductors including $SrPd_2Ge_2$ and APd_2As_2 (A=Ca,Sr) are full gap s-wave superconductors. In sharp contrast, low T_c Fe-based superconductor KFe_2As_2 is shown to be nodal with symmetry imposed nodes and the superfluid density closely following expectation for d-wave superconducting state. Doping evolution of the superconducting gap in $Ba_{1-x}K_xFe_2As_2$ shows that, similar to previously studied case of $Ba(Fe,Co)_2As_2$, the superconducting gap develops extreme anisotropy at the edges of the superconducting dome and is full

at the optimal doping. This full gap picture of the superconducting gap is found in stoichiometric LiFeAs as well. The doping evolution trend of the superconducting gap was verified in another family of materials $Ca_{10}(Pt_3As_8)[(Fe_{1-x}Pt_x)_2As_2]_5$ in which exponent of the power-law monotonically changes from 2.36 at optimal doping to 1.7 in heavily underdoped compositions. Because magnetism and superconductivity coexist in the phase diagram of underdoped BaK122 and are separated in 10-3-8, similar gap structure in both materials suggests that the long range magnetic order does not affect nodal structure, contrary to expectation for conventional superconductors. Study of the penetration depth and superfluid density in $Fe_{1+y}Te_{1-x}Se_x$ found a robust power-law behavior of the low-temperature $\Delta\lambda(T) \propto T^n$ with $n \approx 2.1$ and 2.3 for $Fe_{1.03}(Te_{0.63}Se_{0.37})$ and $Fe(Te_{0.58}Se_{0.42})$, respectively. The absolute value, $\lambda(0) \approx 560 \pm 20$ nm, was determined in $Fe_{1.03}(Te_{0.63}Se_{0.37})$ by the Al-coating technique. The analysis of the superfluid density shows a clear signature of nodeless two-gap superconducting state with strong pair breaking effect. Except for nodal superconducting gap structure in KFe₂As₂ all these observations do not contradict superconducting g_{\pm} pairing.

To get further insight into the superconducting pairing mechanism we studied effect of deliberately introduced disorder. Na-doping into KFe₂As₂ was shown to increase residual electrical resistivity, and suppress T_c showing pairbreaking character of scattering. Disorder changes exponent from T-linear to T^2 , as expected for superconducting gap with vertical line nodes. Temperature dependent superfluid density in a Na-doped sample in the whole temperature range closely follows expectation for dirty d-wave state. Irradiation with heavy ions in optimally electron-doped Ba(Fe,T)₂As₂ (T=Co, Ni) results in slight suppression of T_c and decrease of the exponent of the power-law function. Taken together with reports of the fully gapped states from other measurements, our results present a convincing case in favor of the extended s_{\pm} pairing symmetry with nodeless order parameter in the optimally doped 122 system.

Experimental results presented in this thesis support evolution of the superconducting

gap from isotropic and full at optimal doping to highly anisotropic at the edges of the superconducting dome. Unfortunately, for hole-doped BaK122 materials high quality single crystals are not available for over-doped compounds at the moment, similar to Ca10-3-8. Different symmetry of the superconducting gap at optimal doping and at terminal KFe₂As₂ suggest a phase transition as a function of doping. Similar phase transition was suggested to happen in KFe₂As₂ under pressure [247]. Study of this phase transition maybe important future continuation of this thesis. This would require development of London penetration depth measurement under pressure. In principle, TDR measurements can be performed with a small pickup coil inside a pressure cell, but this would require to overcome issues related to thermal instability of the TDR circuit as well as non-trivial background signal.

As can be seen from this study, stoichiometric KFe₂As₂ and LiFeAs offer unique opportunity to study materials free of substitutional disorder. Another way to study evolution of the superconducting gap in clean materials is to use pressure as a tuning parameter. It is known that stoichiometric BaFe₂As₂ can be tuned across the whole superconducting dome by application of pressure of order of 100 kbar. Provided we have capability to measure London penetration depth under pressure, this experiment would allow us to study the evolution of superconducting gap in clean materials for all doping regime.

BIBLIOGRAPHY

- [1] J. Bardeen, Physics Today **43**, 25 (1990).
- [2] F. London and H. London, Proceedings of the Royal Society of London. Series A, Mathematical and Physical Sciences **149**, 71 (1935).
- [3] V. L. Ginzburg and L. D. Landau, Zh. Eksp. Teo. Fiz. 20, 1064 (1950).
- [4] E. Maxwell, Phys. Rev. **78**, 477 (1950).
- [5] W. S. Corak, B. B. Goodman, C. B. Satterthwaite, and A. Wexler, Phys. Rev. 102, 656 (1956).
- [6] L. N. Cooper, Phys. Rev. **104**, 1189 (1956).
- [7] J. Bardeen, L. N. Cooper, and J. R. Schrieffer, Phys. Rev. 108, 1175 (1957).
- [8] W. L. McMillan, Phys. Rev. **167**, 331 (1968).
- [9] M. L. Cohen and P. W. Anderson, AIP Conference Proceedings 4, 17 (1972).
- [10] P. Anderson, Journal of Physics and Chemistry of Solids 11, 26 (1959).
- [11] A. A. Abrikosov and L. P. Gor'kov, Sov. Phys.-JETP 12, 1243 (1961).
- [12] R. J. Cava, H. Takagi, B. Batlogg, H. W. Zandbergen, J. J. Krajewski, W. F. Peck, R. B. van Dover, R. J. Felder, T. Siegrist, K. Mizuhashi, J. O. Lee, H. Eisaki, S. A. Carter, and S. Uchida, Nature 367, 146 (1994).

- [13] P. C. Canfield, P. L. Gammel, and D. J. Bishop, Physics Today 51, 40 (1998).
- [14] J. Nagamatsu, N. Nakagawa, T. Muranaka, Y. Zenitani, and J. Akimitsu, Nature 410, 63 (2001).
- [15] P. C. Canfield and G. W. Crabtree, Physics Today 56, 34 (2003).
- [16] S. L. Bud'ko, G. Lapertot, C. Petrovic, C. E. Cunningham, N. Anderson, and P. C. Canfield, Phys. Rev. Lett. 86, 1877 (2001).
- [17] F. Bouquet, Y. Wang, R. A. Fisher, D. G. Hinks, J. D. Jorgensen, A. Junod, and N. E. Phillips, EPL (Europhysics Letters) 56, 856 (2001).
- [18] J. D. Fletcher, A. Carrington, O. J. Taylor, S. M. Kazakov, and J. Karpinski, Phys. Rev. Lett. 95, 097005 (2005).
- [19] C. C. Tsuei and J. R. Kirtley, Rev. Mod. Phys. 72, 969 (2000).
- [20] F. Steglich, J. Aarts, C. D. Bredl, W. Lieke, D. Meschede, W. Franz, and H. Schäfer, Phys. Rev. Lett. 43, 1892 (1979).
- [21] G. R. Stewart, Rev. Mod. Phys. 56, 755 (1984).
- [22] N. D. Mathur, F. M. Grosche, S. R. Julian, I. R. Walker, D. M. Freye, R. K. W. Haselwimmer, and G. G. Lonzarich, Nature 394, 39 (1998).
- [23] C. Petrovic, P. G. Pagliuso, M. F. Hundley, R. Movshovich, J. L. Sarrao, J. D. Thompson, Z. Fisk, and P. Monthoux, Journal of Physics: Condensed Matter 13, L337 (2001).
- [24] J. D. Thompson and Z. Fisk, Journal of the Physical Society of Japan 81, 011002 (2012).
- [25] Y. Kamihara, T. Watanabe, M. Hirano, and H. Hosono, J. Am. Chem. Soc. 130, 3296 (2008).

- [26] Z.-A. Ren, G.-C. Che, X.-L. Dong, J. Yang, W. Lu, W. Yi, X.-L. Shen, Z.-C. Li, L.-L. Sun, F. Zhou, and Z.-X. Zhao, EPL (Europhysics Letters) 83, 17002 (2008).
- [27] N. Spyrison, M. A. Tanatar, K. Cho, Y. Song, P. Dai, C. Zhang, and R. Prozorov, Phys. Rev. B 86, 144528 (2012).
- [28] T. Y. Chen, Z. Tesanovic, R. H. Liu, X. H. Chen, and C. L. Chien, Nature 453, 1224 (2008).
- [29] T. Kondo, A. F. Santander-Syro, O. Copie, C. Liu, M. E. Tillman, E. D. Mun, J. Schmalian, S. L. Bud'ko, M. A. Tanatar, P. C. Canfield, and A. Kaminski, Phys. Rev. Lett. 101, 147003 (2008).
- [30] P. C. Canfield and S. L. Bud'ko, Annual Review of Condensed Matter Physics 1, 27 (2010).
- [31] D. C. Johnston, Advances in Physics 59, 803 (2010).
- [32] G. R. Stewart, Rev. Mod. Phys. 83, 1589 (2011).
- [33] K. Cho, M. A. Tanatar, H. Kim, W. E. Straszheim, N. Ni, R. J. Cava, and R. Prozorov, Phys. Rev. B 85, 020504 (2012).
- [34] N. Ni, J. M. Allred, B. C. Chan, and R. J. Cava, Proceedings of the National Academy of Sciences 108, E1019 (2011).
- [35] J. Paglione and R. L. Greene, Nat Phys **6**, 645 (2010).
- [36] I. I. Mazin, Nature **464**, 183 (2010).
- [37] N. E. Hussey, M. Abdel-Jawad, A. Carrington, A. P. Mackenzie, and L. Balicas, Nature 425, 814 (2003).
- [38] I. I. Mazin and J. Schmalian, Physica C 469, 614 (2009).

- [39] N. Doiron-Leyraud, C. Proust, D. LeBoeuf, J. Levallois, J.-B. Bonnemaison, R. Liang, D. A. Bonn, W. N. Hardy, and L. Taillefer, Nature 447, 565 (2007).
- [40] S. Nandi, M. G. Kim, A. Kreyssig, R. M. Fernandes, D. K. Pratt, A. Thaler, N. Ni, S. L. Bud'ko, P. C. Canfield, J. Schmalian, R. J. McQueeney, and A. I. Goldman, Phys. Rev. Lett. 104, 057006 (2010).
- [41] S. Avci, O. Chmaissem, D. Y. Chung, S. Rosenkranz, E. A. Goremychkin, J. P. Castellan, I. S. Todorov, J. A. Schlueter, H. Claus, A. Daoud-Aladine, D. D. Khalyavin, M. G. Kanatzidis, and R. Osborn, Phys. Rev. B 85, 184507 (2012).
- [42] S. Kasahara, T. Shibauchi, K. Hashimoto, K. Ikada, S. Tonegawa, R. Okazaki, H. Shishido, H. Ikeda, H. Takeya, K. Hirata, T. Terashima, and Y. Matsuda, Phys. Rev. B 81, 184519 (2010).
- [43] C. Meingast, O. Kraut, T. Wolf, H. Wühl, A. Erb, and G. Müller-Vogt, Phys. Rev. Lett. 67, 1634 (1991).
- [44] M. Rotter, M. Tegel, and D. Johrendt, Phys. Rev. Lett. 101, 107006 (2008).
- [45] A. Thaler, N. Ni, A. Kracher, J. Q. Yan, S. L. Bud'ko, and P. C. Canfield, Phys. Rev. B 82, 014534 (2010).
- [46] M. Gooch, B. Lv, J. H. Tapp, Z. Tang, B. Lorenz, A. M. Guloy, and P. C. W. Chu, EPL 85, 27005 (2009).
- [47] J. Zhao, Q. Huang, C. de la Cruz, S. Li, J. W. Lynn, Y. Chen, M. A. Green, G. F. Chen, G. Li, Z. Li, J. L. Luo, N. L. Wang, and P. Dai, Nat Mater 7, 953 (2008).
- [48] N. Katayama, S. Ji, D. Louca, S. Lee, M. Fujita, T. J. Sato, J. Wen, Z. Xu, G. Gu, G. Xu, Z. Lin, M. Enoki, S. Chang, K. Yamada, and J. M. Tranquada, Journal of the Physical Society of Japan 79, 113702 (2010).

- [49] G. F. Chen, Z. Li, D. Wu, G. Li, W. Z. Hu, J. Dong, P. Zheng, J. L. Luo, and N. L. Wang, Phys. Rev. Lett. 100, 247002 (2008).
- [50] M. H. Fang, H. M. Pham, B. Qian, T. J. Liu, E. K. Vehstedt, Y. Liu, L. Spinu, and Z. Q. Mao, Phys. Rev. B 78, 224503 (2008).
- [51] T. M. McQueen, Q. Huang, V. Ksenofontov, C. Felser, Q. Xu, H. Zandbergen, Y. S. Hor, J. Allred, A. J. Williams, D. Qu, J. Checkelsky, N. P. Ong, and R. J. Cava, Phys. Rev. B 79, 014522 (2009).
- [52] E. Boaknin, R. W. Hill, C. Proust, C. Lupien, L. Taillefer, and P. C. Canfield, Phys. Rev. Lett. 87, 237001 (2001).
- [53] T. Baba, T. Yokoya, S. Tsuda, T. Watanabe, M. Nohara, H. Takagi, T. Oguchi, and S. Shin, Phys. Rev. B 81, 180509 (2010).
- [54] P. Szabó, P. Samuely, J. Kačmarčik, T. Klein, J. Marcus, D. Fruchart, S. Miraglia,C. Marcenat, and A. G. M. Jansen, Phys. Rev. Lett. 87, 137005 (2001).
- [55] M. Iavarone, G. Karapetrov, A. E. Koshelev, W. K. Kwok, G. W. Crabtree, D. G. Hinks, W. N. Kang, E.-M. Choi, H. J. Kim, H.-J. Kim, and S. I. Lee, Phys. Rev. Lett. 89, 187002 (2002).
- [56] M. Putti, M. Affronte, C. Ferdeghini, P. Manfrinetti, C. Tarantini, and E. Lehmann, Phys. Rev. Lett. 96, 077003 (2006).
- [57] I. I. Mazin, D. J. Singh, M. D. Johannes, and M. H. Du, Phys. Rev. Lett. 101, 057003 (2008).
- [58] R. H. Liu, T. Wu, G. Wu, H. Chen, X. F. Wang, Y. L. Xie, J. J. Ying, Y. J. Yan,
 Q. J. Li, B. C. Shi, W. S. Chu, Z. Y. Wu, and X. H. Chen, Nature 459, 64 (2009).

- [59] P. M. Shirage, K. Miyazawa, K. Kihou, H. Kito, Y. Yoshida, Y. Tanaka, H. Eisaki, and A. Iyo, Phys. Rev. Lett. 105, 037004 (2010).
- [60] C. Stock, C. Broholm, J. Hudis, H. J. Kang, and C. Petrovic, Phys. Rev. Lett. 100, 087001 (2008).
- [61] A. D. Christianson, E. A. Goremychkin, R. Osborn, S. Rosenkranz, M. D. Lumsden, C. D. Malliakas, I. S. Todorov, H. Claus, D. Y. Chung, M. G. Kanatzidis, R. I. Bewley, and T. Guidi, Nature 456, 930 (2008).
- [62] D. J. Van Harlingen, Rev. Mod. Phys. 67, 515 (1995).
- [63] J. S. Kim, B. D. Faeth, and G. R. Stewart, Phys. Rev. B 86, 054509 (2012).
- [64] J. S. Kim, E. G. Kim, G. R. Stewart, X. H. Chen, and X. F. Wang, Phys. Rev. B 83, 172502 (2011).
- [65] S. L. Bud'ko, N. Ni, and P. C. Canfield, Phys. Rev. B 79, 220516 (2009).
- [66] V. G. Kogan, Phys. Rev. B **80**, 214532 (2009).
- [67] V. G. Kogan, Phys. Rev. B 81, 184528 (2010).
- [68] M. G. Vavilov, A. V. Chubukov, and A. B. Vorontsov, Phys. Rev. B 84, 140502 (2011).
- [69] J. Zaanen, Phys. Rev. B 80, 212502 (2009).
- [70] M. Sigrist and K. Ueda, Rev. Mod. Phys. **63**, 239 (1991).
- [71] K. Gofryk, A. S. Sefat, E. D. Bauer, M. A. McGuire, B. C. Sales, D. Mandrus, J. D. Thompson, and F. Ronning, New Journal of Physics 12, 023006 (2010).
- [72] K. Gofryk, A. B. Vorontsov, I. Vekhter, A. S. Sefat, T. Imai, E. D. Bauer, J. D. Thompson, and F. Ronning, Phys. Rev. B 83, 064513 (2011).

- [73] G. E. Volovik, JETP Lett. **58**, 469 (1993).
- [74] C. Kübert and P. Hirschfeld, Solid State Communications 105, 459 (1998).
- [75] D.-J. Jang, A. B. Vorontsov, I. Vekhter, K. Gofryk, Z. Yang, S. Ju, J. B. Hong, J. H. Han, Y. S. Kwon, F. Ronning, J. D. Thompson, and T. Park, New Journal of Physics 13, 023036 (2011).
- [76] G. Mu, B. Zeng, P. Cheng, Z.-S. Wang, L. Fang, B. Shen, L. Shan, C. Ren, and H.-H. Wen, Chinese Physics Letters 27, 037402 (2010).
- [77] M. A. Tanatar, J.-P. Reid, H. Shakeripour, X. G. Luo, N. Doiron-Leyraud, N. Ni, S. L. Bud'ko, P. C. Canfield, R. Prozorov, and L. Taillefer, Phys. Rev. Lett. 104, 067002 (2010).
- [78] J.-P. Reid, M. A. Tanatar, X. G. Luo, H. Shakeripour, N. Doiron-Leyraud, N. Ni, S. L. Bud'ko, P. C. Canfield, R. Prozorov, and L. Taillefer, Phys. Rev. B 82, 064501 (2010).
- [79] X. G. Luo, M. A. Tanatar, J.-P. Reid, H. Shakeripour, N. Doiron-Leyraud, N. Ni, S. L. Bud'ko, P. C. Canfield, H. Luo, Z. Wang, H.-H. Wen, R. Prozorov, and L. Taillefer, Phys. Rev. B 80, 140503 (2009).
- [80] B. S. Chandrasekhar and D. Eizel, Ann. Physik 2, 535 (1993).
- [81] D. Xu, S. K. Yip, and J. A. Sauls, Phys. Rev. B **51**, 16233 (1995).
- [82] P. J. Hirschfeld and N. Goldenfeld, Phys. Rev. B 48, 4219 (1993).
- [83] L. Malone, J. D. Fletcher, A. Serafin, A. Carrington, N. D. Zhigadlo, Z. Bukowski, S. Katrych, and J. Karpinski, Phys. Rev. B 79, 140501 (2009).

- [84] K. Hashimoto, A. Serafin, S. Tonegawa, R. Katsumata, R. Okazaki, T. Saito, H. Fukazawa, Y. Kohori, K. Kihou, C. H. Lee, A. Iyo, H. Eisaki, H. Ikeda, Y. Matsuda, A. Carrington, and T. Shibauchi, Phys. Rev. B 82, 014526 (2010).
- [85] R. T. Gordon, N. Ni, C. Martin, M. A. Tanatar, M. D. Vannette, H. Kim, G. D. Samolyuk, J. Schmalian, S. Nandi, A. Kreyssig, A. I. Goldman, J. Q. Yan, S. L. Bud'ko, P. C. Canfield, and R. Prozorov, Phys. Rev. Lett. 102, 127004 (2009).
- [86] R. T. Gordon, C. Martin, H. Kim, N. Ni, M. A. Tanatar, J. Schmalian, I. I. Mazin, S. L. Bud'ko, P. C. Canfield, and R. Prozorov, Phys. Rev. B 79, 100506(R) (2009).
- [87] C. Martin, M. E. Tillman, H. Kim, M. A. Tanatar, S. K. Kim, A. Kreyssig, R. T. Gordon, M. D. Vannette, S. Nandi, V. G. Kogan, S. L. Bud'ko, P. C. Canfield, A. I. Goldman, and R. Prozorov, Phys. Rev. Lett. 102, 247002 (2009).
- [88] J. R. Cooper, Phys. Rev. B **54**, R3753 (1996).
- [89] Y. Bang, EPL (Europhysics Letters) 86, 47001 (2009).
- [90] A. B. Vorontsov, M. G. Vavilov, and A. V. Chubukov, Phys. Rev. B 79, 140507 (2009).
- [91] J. D. Fletcher, A. Serafin, L. Malone, J. G. Analytis, J.-H. Chu, A. S. Erickson, I. R. Fisher, and A. Carrington, Phys. Rev. Lett. 102, 147001 (2009).
- [92] C. W. Hicks, T. M. Lippman, M. E. Huber, H. G. Analytis, J.-H. Chu, and A. S. Erickson, Phys. Rev. Lett. 103, 127003 (2009).
- [93] Y. Imai, H. Takahashi, K. Kitagawa, K. Matsubayashi, N. Nakai, Y. Nagai, Y. Uwatoko, M. Machida, and A. Maeda, Journal of the Physical Society of Japan 80, 013704 (2011).

- [94] H. Kim, M. A. Tanatar, Y. J. Song, Y. S. Kwon, and R. Prozorov, Phys. Rev. B 83, 100502 (2011).
- [95] K. Hashimoto, S. Kasahara, R. Katsumata, Y. Mizukami, M. Yamashita, H. Ikeda, T. Terashima, A. Carrington, Y. Matsuda, and T. Shibauchi, Phys. Rev. Lett. 108, 047003 (2012).
- [96] C. Boghosian, H. Meyer, and J. E. Rives, Phys. Rev. **146**, 110 (1966).
- [97] C. T. V. Degrift, Review of Scientific Instruments 46, 599 (1975).
- [98] M. D. Vannette, Ph.D. thesis, Iowa State University (2009).
- [99] R. T. Gordon, Ph.D. thesis, Iowa State University (2011).
- [100] R. Prozorov, R. W. Giannetta, A. Carrington, and F. M. Araujo-Moreira, Phys. Rev. B 62, 115 (2000).
- [101] R. Prozorov and R. W. Giannetta, Superconductor Science and Technology 19, R41 (2006).
- [102] R. Prozorov and V. G. Kogan, Reports on Progress in Physics 74, 124505 (2011).
- [103] J. E. Sonier, Reports on Progress in Physics **70**, 1717 (2007).
- [104] D. N. Basov and T. Timusk, Rev. Mod. Phys. 77, 721 (2005).
- [105] R. Prozorov, R. W. Giannetta, A. Carrington, P. Fournier, R. L. Greene, P. Guptasarma, D. G. Hinks, and A. R. Banks, Appl. Phys. Lett. 77, 4202 (2000).
- [106] T. M. Lippman, B. Kalisky, H. Kim, M. A. Tanatar, S. L. Budko, P. C. Canfield, R. Prozorov, and K. A. Moler, Physica C: Superconductivity 483, 91 (2012).
- [107] L. Luan, O. M. Auslaender, T. M. Lippman, C. W. Hicks, B. Kalisky, J.-H. Chu, J. G. Analytis, I. R. Fisher, J. R. Kirtley, and K. A. Moler, arXiv:0909.0744v2 (2010).

- [108] J. R. Kirtley, Reports on Progress in Physics 73, 126501 (2010).
- [109] A. Rutgers, Physica 1, 1055 (1934).
- [110] S. Kamal, R. Liang, A. Hosseini, D. A. Bonn, and W. N. Hardy, Phys. Rev. B 58, R8933 (1998).
- [111] E. M. Lifshitz, L. D. Landau, and L. P. Pitaevskii, *Electrodynamics of Continuous Media*, 2nd ed. (Butterworth-Heinemann, 1984).
- [112] R. Parks, *Superconductivity*, Superconductivity No. v. 2 (Marcel Dekker, Incorporated, 1969).
- [113] V. G. Kogan, Phys. Rev. B **66**, 020509 (2002).
- [114] D. Markowitz and L. P. Kadanoff, Phys. Rev. 131, 563 (1963).
- [115] K. D. Belashchenko, M. v. Schilfgaarde, and V. P. Antropov, Phys. Rev. B 64, 092503 (2001).
- [116] H. J. Choi, D. Roundy, H. Sun, M. L. Cohen, and S. G. Louie, Phys. Rev. B 66, 020513 (2002).
- [117] V. G. Kogan and R. Prozorov, Reports on Progress in Physics 75, 114502 (2012).
- [118] H. W. Weber, E. Seidl, C. Laa, E. Schachinger, M. Prohammer, A. Junod, and D. Eckert, Phys. Rev. B 44, 7585 (1991).
- [119] M. Ito, H. Muta, M. Uno, and S. Yamanaka, Journal of Alloys and Compounds 425, 164 (2006).
- [120] S. J. Williamson, Phys. Rev. B 2, 3545 (1970).
- [121] B. W. Maxfield and W. L. McLean, Phys. Rev. **139**, A1515 (1965).

- [122] C. Niedermayer, C. Bernhard, T. Holden, R. K. Kremer, and K. Ahn, Phys. Rev. B 65, 094512 (2002).
- [123] K. Ohishi, T. Muranaka, J. Akimitsu, A. Koda, W. Higemoto, and R. Kadono, Journal of the Physical Society of Japan 72, 29 (2003).
- [124] H. Kim, N. H. Sung, B. K. Cho, M. A. Tanatar, and R. Prozorov, Phys. Rev. B 87, 094515 (2013).
- [125] J. H. Tapp, Z. Tang, B. Lv, K. Sasmal, B. Lorenz, P. C. W. Chu, and A. M. Guloy, Phys. Rev. B 78, 060505 (2008).
- [126] F. Wei, F. Chen, K. Sasmal, B. Lv, Z. J. Tang, Y. Y. Xue, A. M. Guloy, and C. W. Chu, Phys. Rev. B 81, 134527 (2010).
- [127] K. Cho, H. Kim, M. A. Tanatar, Y. J. Song, Y. S. Kwon, W. A. Coniglio, C. C. Agosta, A. Gurevich, and R. Prozorov, Phys. Rev. B 83, 060502 (2011).
- [128] F. L. Pratt, P. J. Baker, S. J. Blundell, T. Lancaster, H. J. Lewtas, P. Adamson,M. J. Pitcher, D. R. Parker, and S. J. Clarke, Phys. Rev. B 79, 052508 (2009).
- [129] D. Braithwaite, G. Lapertot, W. Knafo, and I. Sheikin, Journal of the Physical Society of Japan 79, 053703 (2010).
- [130] T. Klein, D. Braithwaite, A. Demuer, W. Knafo, G. Lapertot, C. Marcenat, P. Rodière, I. Sheikin, P. Strobel, A. Sulpice, and P. Toulemonde, Phys. Rev. B 82, 184506 (2010).
- [131] P. K. Biswas, G. Balakrishnan, D. M. Paul, C. V. Tomy, M. R. Lees, and A. D. Hillier, Phys. Rev. B 81, 092510 (2010).
- [132] H. Kim, C. Martin, R. T. Gordon, M. A. Tanatar, J. Hu, B. Qian, Z. Q. Mao, R. Hu, C. Petrovic, N. Salovich, R. Giannetta, and R. Prozorov, Phys. Rev. B 81, 180503 (2010).

- [133] C. Poole, H. Farach, R. Creswick, and R. Prozorov, Superconductivity, 2nd ed., Superconductivity Series (Academic Press, 2010) p. 670.
- [134] Y. Wang, B. Revaz, A. Erb, and A. Junod, Phys. Rev. B 63, 094508 (2001).
- [135] U. Welp, W. K. Kwok, G. W. Crabtree, K. G. Vandervoort, and J. Z. Liu, Phys. Rev. Lett. 62, 1908 (1989).
- [136] L. Shan, K. Xia, Z. Y. Liu, H. H. Wen, Z. A. Ren, G. C. Che, and Z. X. Zhao, Phys. Rev. B 68, 024523 (2003).
- [137] G. MacDougall, R. Cava, S.-J. Kim, P. Russo, A. Savici, C. Wiebe, A. Winkels, Y. Uemura, and G. Luke, Physica B: Condensed Matter 374 - 375, 263 (2006).
- [138] A. Carrington, A. P. Mackenzie, and A. Tyler, Phys. Rev. B 54, R3788 (1996).
- [139] H. Ding, P. Richard, K. Nakayama, K. Sugawara, T. Arakane, Y. Sekiba, A. Takayama, S. Souma, T. Sato, T. Takahashi, Z. Wang, X. Dai, Z. Fang, G. F. Chen, J. L. Luo, and N. L. Wang, EPL 83, 47001 (2008).
- [140] C. Martin, H. Kim, R. T. Gordon, N. Ni, V. G. Kogan, S. L. Bud'ko, P. C. Canfield,
 M. A. Tanatar, and R. Prozorov, Phys. Rev. B 81, 060505 (2010).
- [141] T. Zhou, G. Koutroulakis, J. Lodico, N. Ni, J. D. Thompson, R. J. Cava, and S. E. Brown, Journal of Physics: Condensed Matter 25, 122201 (2013).
- [142] R. Hu, K. Cho, H. Kim, H. Hodovanets, W. E. Straszheim, M. A. Tanatar, R. Prozorov, S. L. Budko, and P. C. Canfield, Superconductor Science and Technology 24, 065006 (2011).
- [143] W. Bao, Y. Qiu, Q. Huang, M. A. Green, P. Zajdel, M. R. Fitzsimmons, M. Zhernenkov, S. Chang, M. Fang, B. Qian, E. K. Vehstedt, J. Yang, H. M. Pham, L. Spinu, and Z. Q. Mao, Phys. Rev. Lett. 102, 247001 (2009).

- [144] A. Subedi, L. Zhang, D. J. Singh, and M. H. Du, Phys. Rev. B 78, 134514 (2008).
- [145] T.-L. Xia, D. Hou, S. C. Zhao, A. M. Zhang, G. F. Chen, J. L. Luo, N. L. Wang, J. H. Wei, Z.-Y. Lu, and Q. M. Zhang, Phys. Rev. B 79, 140510 (2009).
- [146] K.-W. Yeh, T.-W. Huang, Y. lin Huang, T.-K. Chen, F.-C. Hsu, P. M. Wu, Y.-C. Lee, Y.-Y. Chu, C.-L. Chen, J.-Y. Luo, D.-C. Yan, and M.-K. Wu, EPL (Europhysics Letters) 84, 37002 (2008).
- [147] Y. Mizuguchi, F. Tomioka, S. Tsuda, T. Yamaguchi, and Y. Takano, Applied Physics Letters 94, 012503 (2009).
- [148] Y. Qiu, W. Bao, Y. Zhao, C. Broholm, V. Stanev, Z. Tesanovic, Y. C. Gasparovic, S. Chang, J. Hu, B. Qian, M. Fang, and Z. Mao, Phys. Rev. Lett. 103, 067008 (2009).
- [149] S. Margadonna, Y. Takabayashi, Y. Ohishi, Y. Mizuguchi, Y. Takano, T. Kagayama, T. Nakagawa, M. Takata, and K. Prassides, Phys. Rev. B 80, 064506 (2009).
- [150] T. Imai, K. Ahilan, F. L. Ning, T. M. McQueen, and R. J. Cava, Phys. Rev. Lett. 102, 177005 (2009).
- [151] H. Kotegawa, S. Masaki, Y. Awai, H. Tou, Y. Mizuguchi, and Y. Takano, Journal of the Physical Society of Japan 77, 113703 (2008).
- [152] R. Khasanov, K. Conder, E. Pomjakushina, A. Amato, C. Baines, Z. Bukowski, J. Karpinski, S. Katrych, H.-H. Klauss, H. Luetkens, A. Shengelaya, and N. D. Zhigadlo, Phys. Rev. B 78, 220510 (2008).
- [153] J. K. Dong, T. Y. Guan, S. Y. Zhou, X. Qiu, L. Ding, C. Zhang, U. Patel, Z. L. Xiao, and S. Y. Li, Phys. Rev. B 80, 024518 (2009).

- [154] V. G. Kogan, C. Martin, and R. Prozorov, Phys. Rev. B 80, 014507 (2009).
- [155] R. T. Gordon, H. Kim, N. Salovich, R. W. Giannetta, R. M. Fernandes, V. G. Kogan, T. Prozorov, S. L. Bud'ko, P. C. Canfield, M. A. Tanatar, and R. Prozorov, Phys. Rev. B 82, 054507 (2010).
- [156] R. Hu, E. S. Bozin, J. B. Warren, and C. Petrovic, Phys. Rev. B 80, 214514 (2009).
- [157] R. T. Gordon, H. Kim, M. A. Tanatar, R. Prozorov, and V. G. Kogan, Phys. Rev. B 81, 180501 (2010).
- [158] A. Serafin, A. I. Coldea, A. Y. Ganin, M. J. Rosseinsky, K. Prassides, D. Vignolles, and A. Carrington, Phys. Rev. B 82, 104514 (2010).
- [159] M. Bendele, S. Weyeneth, R. Puzniak, A. Maisuradze, E. Pomjakushina, K. Conder, V. Pomjakushin, H. Luetkens, S. Katrych, A. Wisniewski, R. Khasanov, and H. Keller, Phys. Rev. B 81, 224520 (2010).
- [160] T. Kato, Y. Mizuguchi, H. Nakamura, T. Machida, H. Sakata, and Y. Takano, Phys. Rev. B 80, 180507 (2009).
- [161] J. Hu, T. J. Liu, B. Qian, A. Rotaru, L. Spinu, and Z. Q. Mao, Phys. Rev. B 83, 134521 (2011).
- [162] C. C. Homes, A. Akrap, J. S. Wen, Z. J. Xu, Z. W. Lin, Q. Li, and G. D. Gu, Phys. Rev. B 81, 180508 (2010).
- [163] W. K. Park, C. R. Hunt, H. Z. Arham, Z. J. Xu, J. S. Wen, Z. W. Lin, Q. Li, G. D. Gu, and L. H. Greene, arXiv:1005.0190 (2010).
- [164] K. Nakayama, T. Sato, P. Richard, T. Kawahara, Y. Sekiba, T. Qian, G. F. Chen, J. L. Luo, N. L. Wang, H. Ding, and T. Takahashi, Phys. Rev. Lett. 105, 197001 (2010).

- [165] M. Nohara, S. Kakiya, and K. Kudo, Proceedings of the International Workshop on Novel Superconductors and Super Materials, a (2011).
- [166] M. Neupane, C. Liu, S.-Y. Xu, Y.-J. Wang, N. Ni, J. M. Allred, L. A. Wray, N. Alidoust, H. Lin, R. S. Markiewicz, A. Bansil, R. J. Cava, and M. Z. Hasan, Phys. Rev. B 85, 094510 (2012).
- [167] S. Kakiya, K. Kudo, Y. Nishikubo, K. Oku, E. Nishibori, H. Sawa, T. Yamamoto, T. Nozaka, and M. Nohara, Journal of the Physical Society of Japan 80, 093704 (2011).
- [168] C. Löhnert, T. Stürzer, M. Tegel, R. Frankovsky, G. Friederichs, and D. Johrendt, Angewandte Chemie International Edition 50, 9195 (2011).
- [169] M. M. Altarawneh, K. Collar, C. H. Mielke, N. Ni, S. L. Bud'ko, and P. C. Canfield, Phys. Rev. B 78, 220505 (2008).
- [170] A. Gurevich, Reports on Progress in Physics **74**, 124501 (2011).
- [171] M. Putti, I. Pallecchi, E. Bellingeri, M. R. Cimberle, M. Tropeano, C. Ferdeghini, A. Palenzona, C. Tarantini, A. Yamamoto, J. Jiang, J. Jaroszynski, F. Kametani, D. Abraimov, A. Polyanskii, J. D. Weiss, E. E. Hellstrom, A. Gurevich, D. C. Larbalestier, R. Jin, B. C. Sales, A. S. Sefat, M. A. McGuire, D. Mandrus, P. Cheng, Y. Jia, H. H. Wen, S. Lee, and C. B. Eom, Superconductor Science and Technology 23, 034003 (2010).
- [172] R. Prozorov, M. A. Tanatar, N. Ni, A. Kreyssig, S. Nandi, S. L. Bud'ko, A. I. Goldman, and P. C. Canfield, Phys. Rev. B 80, 174517 (2009).
- [173] N. Plakida, High-Temperature Cuprate Superconductors: Experiment, Theory and Applications, Springer series in solid-state sciences (Springer Berlin Heidelberg, 2010).

- [174] T. Nakano, S. Tsutsumi, N. Fujiwara, S. Matsuishi, and H. Hosono, Phys. Rev. B 83, 180508 (2011).
- [175] H. Luetkens, H.-H. Klauss, M. Kraken, F. J. Litterst, T. Dellmann, R. Klingeler, C. Hess, R. Khasanov, A. Amato, C. Baines, M. Kosmala, O. J. Schumann, M. Braden, J. Hamann-Borrero, N. Leps, A. Kondrat, G. Behr, J. Werner, and B. Buchner, Nat Mater 8, 305 (2009).
- [176] H. Kontani and S. Onari, Phys. Rev. Lett. **104**, 157001 (2010).
- [177] S. Onari, H. Kontani, and M. Sato, Phys. Rev. B 81, 060504 (2010).
- [178] T. Saito, S. Onari, and H. Kontani, Phys. Rev. B 82, 144510 (2010).
- [179] A. Chubukov, Annual Review of Condensed Matter Physics 3, 57 (2012).
- [180] P. J. Hirschfeld, M. M. Korshunov, and I. I. Mazin, Reports on Progress in Physics 74, 124508 (2011).
- [181] S. Maiti, M. M. Korshunov, T. A. Maier, P. J. Hirschfeld, and A. V. Chubukov, Phys. Rev. B 84, 224505 (2011).
- [182] F. Wang and D.-H. Lee, Science **332**, 200 (2011).
- [183] F. Hardy, T. Wolf, R. A. Fisher, R. Eder, P. Schweiss, P. Adelmann, H. v. Löhneysen, and C. Meingast, Phys. Rev. B 81, 060501 (2010).
- [184] P. J. Hirschfeld and D. J. Scalapino, Physics 3, 64 (2010).
- [185] S. V. Borisenko, V. B. Zabolotnyy, D. V. Evtushinsky, T. K. Kim, I. V. Morozov, A. N. Yaresko, A. A. Kordyuk, G. Behr, A. Vasiliev, R. Follath, and B. Büchner, Phys. Rev. Lett. 105, 067002 (2010).

- [186] D. S. Inosov, J. S. White, D. V. Evtushinsky, I. V. Morozov, A. Cameron, U. Stockert, V. B. Zabolotnyy, T. K. Kim, A. A. Kordyuk, S. V. Borisenko, E. M. Forgan, R. Klingeler, J. T. Park, S. Wurmehl, A. N. Vasiliev, G. Behr, C. D. Dewhurt, and V. Hinkov, Phys. Rev. Lett. 104, 187001 (2010).
- [187] M. A. Tanatar, J.-P. Reid, S. René de Cotret, N. Doiron-Leyraud, F. Laliberté, E. Hassinger, J. Chang, H. Kim, K. Cho, Y. J. Song, Y. S. Kwon, R. Prozorov, and L. Taillefer, Phys. Rev. B 84, 054507 (2011).
- [188] H. Fukazawa, T. Yamazaki, K. Kondo, Y. Kohori, N. Takeshita, P. M. Shirage, K. Kihou, K. Miyazawa, H. Kito, H. Eisaki, and A. Iyo, J. Phys. Soc. Jpn. 78, 033704 (2009).
- [189] J. K. Dong, S. Y. Zhou, T. Y. Guan, H. Zhang, Y. F. Dai, X. Qiu, X. F. Wang, Y. He, X. H. Chen, and S. Y. Li, Phys. Rev. Lett. 104, 087005 (2010).
- [190] A. V. Chubukov, M. G. Vavilov, and A. B. Vorontsov, Phys. Rev. B 80, 140515 (2009).
- [191] K. Hashimoto, M. Yamashita, S. Kasahara, Y. Senshu, N. Nakata, S. Tonegawa, K. Ikada, A. Serafin, A. Carrington, T. Terashima, H. Ikeda, T. Shibauchi, and Y. Matsuda, Phys. Rev. B 81, 220501 (2010).
- [192] K. Nakayama, T. Sato, P. Richard, Y.-M. Xu, T. Kawahara, K. Umezawa, T. Qian, M. Neupane, G. F. Chen, H. Ding, and T. Takahashi, Phys. Rev. B 83, 020501 (2011).
- [193] Z. Li, D. L. Sun, C. T. Lin, Y. H. Su, J. P. Hu, and G.-q. Zheng, Phys. Rev. B 83, 140506 (2011).

- [194] C. Martin, R. T. Gordon, M. A. Tanatar, H. Kim, N. Ni, S. L. Bud'ko, P. C. Canfield, H. Luo, H. H. Wen, Z. Wang, A. B. Vorontsov, V. G. Kogan, and R. Prozorov, Phys. Rev. B 80, 020501 (2009).
- [195] K. Hashimoto, T. Shibauchi, S. Kasahara, K. Ikada, S. Tonegawa, T. Kato, R. Okazaki, C. J. van der Beek, M. Konczykowski, H. Takeya, K. Hirata, T. Terashima, and Y. Matsuda, Phys. Rev. Lett. 102, 207001 (2009).
- [196] H. Luo, Z. Wang, H. Yang, P. Cheng, X. Zhu, and H.-H. Wen, Supercond. Sci. Technol. 21, 125014 (2008).
- [197] S. Avci, O. Chmaissem, E. A. Goremychkin, S. Rosenkranz, J.-P. Castellan, D. Y. Chung, I. S. Todorov, J. A. Schlueter, H. Claus, M. G. Kanatzidis, A. Daoud-Aladine, D. Khalyavin, and R. Osborn, Phys. Rev. B 83, 172503 (2011).
- [198] G. Li, W. Z. Hu, J. Dong, Z. Li, P. Zheng, G. F. Chen, J. L. Luo, and N. L. Wang, Phys. Rev. Lett. 101, 107004 (2008).
- [199] P. Popovich, A. V. Boris, O. V. Dolgov, A. A. Golubov, D. L. Sun, C. T. Lin, R. K. Kremer, and B. Keimer, Phys. Rev. Lett. 105, 027003 (2010).
- [200] G. Mu, H. Luo, Z. Wang, L. Shan, C. Ren, and H.-H. Wen, Phys. Rev. B 79, 174501 (2009).
- [201] H. Kim, R. T. Gordon, M. A. Tanatar, J. Hua, U. Welp, W. K. Kwok, N. Ni, S. L. Bud'ko, P. C. Canfield, A. B. Vorontsov, and R. Prozorov, Phys. Rev. B 82, 060518 (2010).
- [202] A. Glatz and A. E. Koshelev, Phys. Rev. B 82, 012507 (2010).
- [203] R. M. Fernandes and J. Schmalian, Phys. Rev. B 82, 014521 (2010).

- [204] J.-P. Reid, M. A. Tanatar, A. Juneau-Fecteau, R. T. Gordon, S. R. de Cotret, N. Doiron-Leyraud, T. Saito, H. Fukazawa, Y. Kohori, K. Kihou, C. H. Lee, A. Iyo, H. Eisaki, R. Prozorov, and L. Taillefer, Phys. Rev. Lett. 109, 087001 (2012).
- [205] N. Kurita, F. Ronning, Y. Tokiwa, E. D. Bauer, A. Subedi, D. J. Singh, J. D. Thompson, and R. Movshovich, Phys. Rev. Lett. 102, 147004 (2009).
- [206] N. Kurita, F. Ronning, C. F. Miclea, E. D. Bauer, K. Gofryk, J. D. Thompson, and R. Movshovich, Phys. Rev. B 83, 094527 (2011).
- [207] T. K. Kim, A. N. Yaresko, V. B. Zabolotnyy, A. A. Kordyuk, D. V. Evtushinsky, N. H. Sung, B. K. Cho, T. Samuely, P. Szabó, J. G. Rodrigo, J. T. Park, D. S. Inosov, P. Samuely, B. Büchner, and S. V. Borisenko, Phys. Rev. B 85, 014520 (2012).
- [208] V. K. Anand, H. Kim, M. A. Tanatar, R. Prozorov, and D. C. Johnston, Phys. Rev. B 87, 224510 (2013).
- [209] H. Fujii and A. Sato, Phys. Rev. B **79**, 224522 (2009).
- [210] N. H. Sung, J.-S. Rhyee, and B. K. Cho, Phys. Rev. B 83, 094511 (2011).
- [211] E. Helfand and N. R. Werthamer, Phys. Rev. 147, 288 (1966).
- [212] N. H. Sung, C. J. Roh, B. Y. Kang, and B. K. Cho, Journal of Applied Physics 111, 07E117 (2012).
- [213] T. Samuely, P. Szabó, Z. Pribulovó, N. H. Sung, B. K. Cho, T. Klein, V. Cambel, J. G. Rodrigo, and P. Samuely, Superconductor Science and Technology 26, 015010 (2013).
- [214] J. D. Fletcher, A. Carrington, P. Diener, P. Rodiere, J. P. Brison, R. Prozorov, T. Olheiser, and R. W. Giannetta, Phys. Rev. Lett. 98, 057003 (2007).

- [215] R. T. Gordon, M. D. Vannette, C. Martin, Y. Nakajima, T. Tamegai, and R. Prozorov, Phys. Rev. B 78, 024514 (2008).
- [216] F. Ronning, N. Kurita, E. D. Bauer, B. L. Scott, T. Park, T. Klimczuk, R. Movshovich, and J. D. Thompson, Journal of Physics: Condensed Matter 20, 342203 (2008).
- [217] I. Bonalde, B. D. Yanoff, M. B. Salamon, and E. E. M. Chia, Phys. Rev. B 67, 012506 (2003).
- [218] A. F. Kemper, C. Cao, P. J. Hirschfeld, and H.-P. Cheng, Phys. Rev. B 80, 104511 (2009).
- [219] O. V. Dolgov, A. A. Golubov, and D. Parker, New J. Phys. 11, 075012 (2009).
- [220] Y. J. Song, J. S. Ghim, B. H. Min, Y. S. Kwon, M. H. Jung, and J.-S. Rhyee, App. Phys. Lett. 96, 212508 (2010).
- [221] Y. Liu, M. A. Tanatar, V. G. Kogan, H. Kim, T. A. Lograsso, and R. Prozorov, Phys. Rev. B 87, 134513 (2013).
- [222] N. Ni, M. E. Tillman, J.-Q. Yan, A. Kracher, S. T. Hannahs, S. L. Bud'ko, and P. C. Canfield, Phys. Rev. B 78, 214515 (2008).
- [223] E. Colombier, S. L. Bud'ko, N. Ni, and P. C. Canfield, Phys. Rev. B **79**, 224518 (2009).
- [224] C. W. Chu, F. Chen, M. Gooch, A. M. Guloy, B. Lorenz, B. Lv, K. Sasmal, Z. J. Tang, J. H. Tapp, and Y. Y. Xue, Physica C 469, 326 (2009).
- [225] E. Colombier, M. S. Torikachvili, N. Ni, A. Thaler, S. L. Budko, and P. C. Canfield, Superconductor Science and Technology 23, 054003 (2010).

- [226] S. J. Zhang, X. C. Wang, Q. Q. Liu, Y. X. Lv, X. H. Yu, Z. J. Lin, Y. S. Zhao, L. Wang, Y. Ding, H. K. Mao, and C. Q. Jin, EPL (Europhysics Letters) 88, 47008 (2009).
- [227] Y. J. Song, J. S. Ghim, J. H. Yoon, K. J. Lee, M. H. Jung, H.-S. Ji, J. H. Shim, Y. Bang, and Y. S. Kwon, EPL (Europhysics Letters) 94, 57008 (2011).
- [228] M. A. Tanatar, N. Ni, S. L. Bud'ko, P. C. Canfield, and R. Prozorov, Supercond. Sci. Technol. 23, 054002 (2010).
- [229] C. Martin, H. Kim, R. T. Gordon, N. Ni, A. Thaler, V. G. Kogan, S. L. Budko, P. C. Canfield, M. A. Tanatar, and R. Prozorov, Superconductor Science and Technology 23, 065022 (2010).
- [230] N. Doiron-Leyraud, P. Auban-Senzier, S. R. de Cotret, C. Bourbonnais, D. Jérome,K. Bechgaard, and L. Taillefer, Phys. Rev. B 80 80, 214531 (2009).
- [231] W. N. Hardy, D. A. Bonn, D. C. Morgan, R. Liang, and K. Zhang, Phys. Rev. Lett. 70, 3999 (1993).
- [232] S. L. Bud'ko, N. Ni, S. Nandi, G. M. Schmiedeshoff, and P. C. Canfield, Phys. Rev. B 79, 054525 (2009).
- [233] R. Prozorov, M. A. Tanatar, R. T. Gordon, C. Martin, H. Kim, V. G. Kogan, N. Ni,M. E. Tillman, S. L. Bud'ko, and P. C. Canfield, Physica C 469, 582 (2009).
- [234] I. Nekrasov, Z. Pchelkina, and M. Sadovskii, JETP Letters 88, 543 (2008).
- [235] L. Boeri, M. Calandra, I. I. Mazin, O. V. Dolgov, and F. Mauri, Phys. Rev. B 82, 020506 (2010).
- [236] L. Boeri, O. V. Dolgov, and A. A. Golubov, Phys. Rev. Lett. **101**, 026403 (2008).

- [237] K. Sasmal, B. Lv, Z. Tang, F. Y. Wei, Y. Y. Xue, A. M. Guloy, and C. W. Chu, Phys. Rev. B 81, 144512 (2010).
- [238] M. Rotter, M. Pangerl, M. Tegel, and D. Johrendt, Angewandte Chemie International Edition 47, 7949 (2008).
- [239] G. Mu, J. Tang, Y. Tanabe, J. Xu, S. Heguri, and K. Tanigaki, Phys. Rev. B 84, 054505 (2011).
- [240] K. Cho, M. A. Tanatar, N. Spyrison, H. Kim, Y. Song, P. Dai, C. L. Zhang, and R. Prozorov, Phys. Rev. B 86, 020508 (2012).
- [241] J.-P. Reid, A. Juneau-Fecteau, R. T. Gordon, S. R. de Cotret, N. Doiron-Leyraud, X. G. Luo, H. Shakeripour, J. Chang, M. A. Tanatar, H. Kim, R. Prozorov, T. Saito, H. Fukazawa, Y. Kohori, K. Kihou, C. H. Lee, A. Iyo, H. Eisaki, B. Shen, H.-H. Wen, and L. Taillefer, Superconductor Science and Technology 25, 084013 (2012).
- [242] T. Das, EPJ Web of Conferences **23**, 00014 (2012).
- [243] R. Thomale, C. Platt, W. Hanke, J. Hu, and B. A. Bernevig, Phys. Rev. Lett. 107, 117001 (2011).
- [244] H. Kawano-Furukawa, C. J. Bowell, J. S. White, R. W. Heslop, A. S. Cameron, E. M. Forgan, K. Kihou, C. H. Lee, A. Iyo, H. Eisaki, T. Saito, H. Fukazawa, Y. Kohori, R. Cubitt, C. D. Dewhurst, J. L. Gavilano, and M. Zolliker, Phys. Rev. B 84, 024507 (2011).
- [245] A. F. Wang, S. Y. Zhou, X. G. Luo, X. C. Hong, Y. J. Yan, J. J. Ying, P. Cheng, G. J. Ye, Z. J. Xiang, S. Y. Li, and X. H. Chen, arXiv:1206.2030 (2012).
- [246] M. Abdel-Hafiez, V. Grinenko, S. Aswartham, I. Morozov, M. Roslova, O. Vakaliuk, S. Johnston, D. V. Efremov, J. van den Brink, H. Rosner, M. Kumar, C. Hess,

- S. Wurmehl, A. U. B. Wolter, B. Büchner, E. L. Green, J. Wosnitza, P. Vogt, A. Reifenberger, C. Enss, M. Hempel, R. Klingeler, and S.-L. Drechsler, Phys. Rev. B 87, 180507 (2013).
- [247] F. F. Tafti, A. Juneau-Fecteau, M.-E. Delage, S. Rene de Cotret, J.-P. Reid, A. F. Wang, X.-G. Luo, X. H. Chen, N. Doiron-Leyraud, and L. Taillefer, Nat Phys 9, 349 (2013).
- [248] K. Okazaki, Y. Ota, Y. Kotani, W. Malaeb, Y. Ishida, T. Shimojima, T. Kiss,
 S. Watanabe, C.-T. Chen, K. Kihou, C. H. Lee, A. Iyo, H. Eisaki, T. Saito,
 H. Fukazawa, Y. Kohori, K. Hashimoto, T. Shibauchi, Y. Matsuda, H. Ikeda,
 H. Miyahara, R. Arita, A. Chainani, and S. Shin, Science 337, 1314 (2012).
- [249] N. W. Salovich, H. Kim, A. K. Ghosh, R. W. Giannetta, W. Kwok, U. Welp, B. Shen, S. Zhu, H.-H. Wen, M. A. Tanatar, and R. Prozorov, Phys. Rev. B 87, 180502 (2013).
- [250] M. Abdel-Hafiez, S. Aswartham, S. Wurmehl, V. Grinenko, C. Hess, S.-L. Drechsler, S. Johnston, A. U. B. Wolter, B. Büchner, H. Rosner, and L. Boeri, Phys. Rev. B 85, 134533 (2012).
- [251] S. L. Bud'ko, Y. Liu, T. A. Lograsso, and P. C. Canfield, Phys. Rev. B 86, 224514 (2012).
- [252] C. C. Homes, S. V. Dordevic, M. Strongin, D. A. Bonn, R. Liang, W. N. Hardy, S. Komiya, Y. Ando, G. Yu, N. Kaneko, X. Zhao, M. Greven, D. N. Basov, and T. Timusk, Nature 430, 539 (2004).
- [253] V. G. Kogan, Phys. Rev. B 87, 220507 (2013).
- [254] K. Ishida, Y. Nakai, and H. Hosono, J. Phys. Soc. Jpn. 78, 062001 (2009).

- [255] S. Jin, ed., Processing and Properties of High-T_c Superconductors (World Scientific, 1993).
- [256] G. Blatter, M. V. Feigel'man, V. B. Geshkenbein, A. I. Larkin, and V. M. Vinokur, Rev. Mod. Phys. 66, 1125 (1994).
- [257] Y. Zhu, Z. X. Cai, R. C. Budhani, M. Suenaga, and D. O. Welch, Phys. Rev. B 48, 6436 (1993).
- [258] S. I. Woods, A. S. Katz, M. C. de Andrade, J. Herrmann, M. B. Maple, and R. C. Dynes, Phys. Rev. B 58, 8800 (1998).
- [259] K. Kuroki, S. Onari, R. Arita, H. Usui, Y. Tanaka, H. Kontani, and H. Aoki, Phys. Rev. Lett. 101, 087004 (2008).
- [260] S. Onari and H. Kontani, Phys. Rev. Lett. 103, 177001 (2009).
- [261] D. V. Efremov, M. M. Korshunov, O. V. Dolgov, A. A. Golubov, and P. J. Hirschfeld, Phys. Rev. B 84, 180512 (2011).
- [262] Y. Nakajima, Y. Tsuchiya, T. Taen, T. Tamegai, S. Okayasu, and M. Sasase, Phys. Rev. B 80, 012510 (2009).
- [263] L. Fang, Y. Jia, C. Chaparro, G. Sheet, H. Claus, M. A. Kirk, A. E. Koshelev, U. Welp, G. W. Crabtree, W. K. Kwok, S. Zhu, H. F. Hu, J. M. Zuo, H.-H. Wen, and B. Shen, Applied Physics Letters 101, 012601 (2012).
- [264] P. C. Canfield, S. L. Bud'ko, N. Ni, J. Q. Yan, and A. Kracher, Phys. Rev. B 80, 060501 (2009).
- [265] R. Prozorov, M. A. Tanatar, B. Roy, N. Ni, S. L. Bud'ko, P. C. Canfield, J. Hua, U. Welp, and W. K. Kwok, Phys. Rev. B 81, 094509 (2010).

- [266] V. Mishra, A. Vorontsov, P. J. Hirschfeld, and I. Vekhter, Phys. Rev. B 80, 224525 (2009).
- [267] L. Shan, Y.-L. Wang, J. Gong, B. Shen, Y. Huang, H. Yang, C. Ren, and H.-H. Wen, Phys. Rev. B 83, 060510 (2011).
- [268] A. Charnukha, O. V. Dolgov, A. A. Golubov, Y. Matiks, D. L. Sun, C. T. Lin,
 B. Keimer, and A. V. Boris, Phys. Rev. B 84, 174511 (2011).
- [269] I. I. Mazin, O. K. Andersen, O. Jepsen, O. V. Dolgov, J. Kortus, A. A. Golubov, A. B. Kuz'menko, and D. van der Marel, Phys. Rev. Lett. 89, 107002 (2002).
- [270] I. Mazin and V. Antropov, Physica C: Superconductivity 385, 49 (2003).
- [271] N. Chikumoto, A. Yamamoto, M. Konczykowski, and M. Murakami, Physica C: Superconductivity 378-381, Part 1, 466 (2002).
- [272] R. M. Fernandes, M. G. Vavilov, and A. V. Chubukov, Phys. Rev. B 85, 140512 (2012).
- [273] H. Kim, M. A. Tanatar, B. Shen, H.-H. Wen, and R. Prozorov, arXiv:1105.2265 (2011).
- [274] K. Terashima, Y. Sekiba, J. H. Bowen, K. Nakayama, T. Kawahara, T. Sato, P. Richard, Y. M. Xu, L. J. Li, G. H. Cao, Z. A. Xu, H. Ding, and T. Takahashi, PNAS 106, 7330 (2009).